RESEARCH ON LIGHTNING TRANSIENT FIELD-LINE COUPLING AND SYSTEMATIC PROTECTION FOR ULTRA-LARGE-SCALE PHOTOVOLTAIC SYSTEMS

DU ZHENTAO

PhD

The Hong Kong Polytechnic University

2025

The Hong Kong Polytechnic University

Department of Building Environment and Energy Engineering

Research on Lightning Transient Field-Line Coupling and Systematic Protection for Ultra-Large-Scale Photovoltaic Systems

Du Zhentao

A thesis submitted in partial fulfillment of the requirements for the Degree of Doctor of Philosophy

June 2025

CERTIFICATE OF ORIGINALITY

I hereby declare that this thesis is my own work and that, to the best of my knowledge and belief, it reproduces no material previously published or written, nor material that has been accepted for the award of any other degree or diploma, except where due acknowledgement has been made in the text.

(Signed)

Du Zhentao (Name of Student)

Department of Building Environment and Energy Engineering

The Hong Kong Polytechnic University

June 2025

Abstract

With the rapid development of renewable energy, ultra-large-scale photovoltaic (PV) systems face three major challenges in lightning protection. First, existing electromagnetic transient simulation tools lack sufficient accuracy when modeling ultra-large-scale systems due to neglected high-frequency electromagnetic coupling effects and the "curse of dimensionality." Second, conventional lightning protection standards fail to address the unique hybrid AC/DC configurations and wide-area distribution of PV systems. Third, the absence of scientific risk assessment methods leads to unquantified operational decisions.

To address these challenges, this study establishes a field-line coupling model for lightning electromagnetic transients and develops a systematic protection framework. Through theoretical and technological innovations, the following key achievements were made:

1. Modeling Methodology: A novel PEEC-FDTD hybrid algorithm enables accurate simulation of PV systems by combining circuit parameter extraction with time-domain electromagnetic field solving. A potential-line coupling model improves convergence while a dynamic charge-wave lightning channel model enhances near-field precision.

2. Protection Optimization: An innovative topology replaces conventional large-loop

cable designs with small intersecting loops, significantly reducing induced voltages across bypass diodes. Grounding system optimization demonstrates that distributed electrodes and interconnected schemes lower overvoltages during direct strikes.

3. Standardization: Comprehensive grounding experiments quantify transient impedance effects, revealing performance differences between conventional and segmented designs. Dual-end cable armor grounding limits core-sheath voltages below safe thresholds.

4. Risk Assessment: A partition-based heuristic algorithm implements symmetry-driven quadrant reduction and risk-adaptive zoning, achieving accelerated computational efficiency while maintaining accuracy. The methodology balances protection requirements and cost-effectiveness through voltage threshold optimization.

By integrating field-line coupling modeling with systematic protection technologies, this study resolves key challenges in simulation accuracy, standard adaptability, and economic evaluation for ultra-large-scale PV lightning protection. The results provide actionable solutions for safe operation under complex meteorological conditions.

Publications from the Thesis

Published papers

Zhentao Du, Yuxuan Ding, Yaping Du Mingli Chen, "Performance Assessment of Grounding System for Large-ScaleGrid-Connected-Photovoltaic System Using the PEEC Method", IEEE EMC.

Binghao Li, Zhentao Du, Yaping Du. Yuxuan Ding, Yang Zhang, Jinxin Caoetc. (2023). An Advanced Wire-Mesh Model With the Three-Dimensional FDTD Method for Transient Analysis. IEEE Transactions on Electromagnetic Compatibility.

Zhe Li, Jinxin Cao, Yaping Du, Yang Zhang, Chuanzhen Jia, Fangchi Qiu, Zhentao Du, Mingli Chen, “Ground Potential Distribution and Human-body Touch Voltage in Old Residential Communities”, IEEE Transactions on Industry Applications (2023).

Conference papers

Zhentao Du, Xiaobing Xiao, Song Zhang, Xiaomeng He, Yongxiang Cai, and Yue Li A Comparison between Lightning-induced Electric Field Using Uman's formulas and Jefimenko's Equation. The 11th Frontier Academic Forum of Electrical Engineering (FAFEE 2024, Chongqing, China).

Xiaobing Xiao, Lei Jia, Xiaomeng He, Ruihan Qi, Yue Li, Gang Liu, Lu Qu, Zhentao Du, Yuxuan Ding, Yaping Du Comparison of Lightning-Induced Electric Fields Based on Uman's Formulas and improved Jefimenko's Equations. International Colloquium on Lightning and Power Systems International Symposium on Lightning Protection(CIGRE ICLPS - SIPDA 2023 SUZHOU CHINA)

Fangchi Qiu, Jinxin Cao, Yuxuan Ding, Yaping Du, Zhentao Du, “Simulation of Ground Potential Distribution around Grounding Grids using a PEEC Method”, 2022 IEEE/IAS 58th Industrial and Commercial Power Systems Technical Conference (I&CPS). IEEE, 2022.

Paper under review

Zhentao Du, Yuxuan Ding, Yaping Du, Binghao Li, Chakhung Yeung and Quan Zhou, "A Novel Potential-Line Coupling Method for Stable Transient Analysis of Wire Structures in the Time Domain under Indirect Lightning ", IEEE EMC (Under review).

Acknowledgements

Firstly, I would like to express my genuine gratitude to my primary supervisor Prof. Yaping Du, who provide me those opportunities and continuous support during my PhD study and related research. He acted as a role model to me not only academically but also in life. His guidance helped me in all the time of research and writing of this thesis with his patience, dedication and immense knowledge.

Then, I would like to thank Prof. Mingli Chen, for his kind encouragement and supportable guideline for my study in lightning protection and atmospheric research. I also highly appreciate Dr. Yuxuan Ding, who carefully taught me a great deal of theoretical knowledge and provided me with helpful advice on research during my study. I would also like to thank Dr. Binghao Li, for her selfless help and encouragement during the stressful days when I first joined the group.

I would like to express my sincere thanks to the group members, Dr. Xiangen Zhao, Dr. Quan Zhou, Dr. Jinxin Cao, Dr. Jiahua Lyu, Dr. Chuanlong Ma, Dr. Dingchen Li, Dr. Qianchao Wang, Mr. Zhe Li, for their warm support in helping me overcome numerous obstacles in my research. They have also been sharing their expertise in research and caring for my employment development. I would also like to thank Mr. Chuanzhen Jia, Mr.Chakhung Yeung, Mr. Xiao He, Mr. Jingjie Ye, Mr. Dongchuan Fan, and Ms Nan Feng who brought me many good memories during our study days in Hong Kong as my

good colleagues and friends.

I would also like to solemnly thank my master's supervisors, Prof. Jianguo Wang, Prof. Li Cai, and other teachers at Wuhan University. Without their encouragement and guidance, I will not be brave enough to pursue my Ph.D. degree.

Finally, I would like to thank my parents, who have been trying their best to support and encourage me to do whatever I want.

These years have been fulfilling, blissful, and unforgettable. Thank you to everyone I have met along the way and wish you good health, good work, and happy life on your special day.

Table of Contents

List of Figures

List of Tables

Chapter1

Introduction

1.1 Background

With the accelerated global transition in energy structures, photovoltaic (PV) power generation has emerged as one of the most rapidly developing industries in the renewable energy sector [1,2]. According to the latest statistics from the International Renewable Energy Agency (IRENA), global cumulative PV installed capacity exceeded 1.2 terawatts (TW) by the end of 2023, with annual installations in China, the United States, and European Union countries reaching historic highs. Notably, PV power plant construction has exhibited a significant trend toward gigawatt-scale expansion. Single-project capacities have surged from early megawatt-scale to gigawatt-scale, exemplified by China's Qinghai Talatan PV Industrial Park. These ultra-large-scale PV systems typically consist of tens of thousands of PV modules interconnected through complex DC convergence networks, spanning tens of square kilometers and forming a unique distributed-centralized hybrid topology.

However, the large-scale development of PV power plants faces severe challenges in lightning protection. Statistical data indicate that 23%–35%

of global PV system failures annually are attributed to lightning strikes [3], with risks of lightning damage in gigawatt-scale PV plants growing fast. Analyses of typical lightning-induced accidents reveal that transient overvoltages caused by lightning current intrusion not only directly damage components (e.g., Potential Induced Degradation (PID) effects in modules and IGBT module breakdowns in inverters) but also generate complex traveling wave reflections on DC buses through field-line coupling mechanisms. Such electromagnetic transient processes have led to anomalous "remote-device-first-failure" incidents, where equipment far from the strike point fails before nearby surge protectors.

Current PV lightning protection standards (e.g., IEC 62446 and GB/T 32512) are primarily based on traditional power system lightning protection theories, focusing on discrete protective measures such as air terminal placement, grounding grid optimization, and SPD selection. However, these approaches exhibit significant limitations in addressing ultra-large-scale PV systems. First, spatial electromagnetic fields generated by field-line coupling may create distributed overvoltages within the system. Secondly, the modular ultra long cable loop structure amplifies the coupling efficiency of lightning electromagnetic pulse (LEMP). Third, existing standards inadequately account for cumulative effects of multiple lightning strokes. For example, fault recordings from a Southeast Asian PV plant revealed that four consecutive lightning

strikes caused persistent energy storage in system-to-ground capacitance, ultimately triggering insulation coordination failure.

The mismatch between traditional protection systems and the scale of modern PV installations has resulted in substantial economic losses. Industry surveys indicate that from 2021 to 2023, annual direct losses from lightning strikes in PV plants exceeding 100 MW globally surpassed $120 million, with indirect energy generation losses reaching 580 million kilowatt-hours [4]. More critically, electromagnetic interference (EMI) from lightning transients has caused multiple maloperations in grid-connected relay protection devices. These issues underscore the inadequacy of traditional "compartmentalized protection" strategies in addressing the holistic electromagnetic characteristics of ultra-large-scale PV systems, necessitating a systematic protection theory grounded in field-line coupling mechanisms.

While the global expansion of ULS-PV systems demonstrates remarkable progress in renewable energy deployment, this scaling introduces three fundamental lightning protection challenges that existing solutions cannot adequately address. First, component-level vulnerabilities persist, particularly in underspecified bypass diodes and extensive DC cabling networks that amplify induced overvoltages. Second, conventional grounding standards fail to account for the hybrid

AC/DC characteristics unique to PV systems, leaving critical gaps in transient energy dissipation. Most critically, the complex electromagnetic topology of gigawatt-scale arrays defies traditional risk assessment methods, rendering current protection schemes ineffective against spatially distributed failure modes. These interconnected challenges - component limitations, grounding inadequacies, and unquantifiable systemic risks - form the critical research gap that Section 1.2 will systematically examine.

1.2 Lightning Threat Mechanisms and Protection Challenges in ULS-PV Systems

1.2.1 Lightning Hazards in Large-Scale Photovoltaic Systems

Ultra-large-scale photovoltaic (ULS-PV) systems face more complex lightning hazards compared to traditional power systems due to their unique electromagnetic structures and operational environments. Lightning damage to PV systems can be categorized into three pathways: direct lightning strikes, induced lightning coupling, and ground potential rise, with field-line coupling-induced distributed overvoltages emerging as a dominant hazard. A 2023 report by the U.S. National Lightning Safety Institute (NLSI) revealed that PV plants covering over 10 km² experience 6–8 times higher lightning strike

probabilities than conventional substations, with damage exhibiting multi-physics coupling characteristics.

Figure 1.1 Lightning Hazards in Large-Scale Photovoltaic Systems

The open structure of PV arrays makes them preferential targets for lightning strikes. Simulation experiments by Japan's New Energy and Industrial Technology Development Organization (NEDO) demonstrated that the 1/4-wavelength effect expands the lightning attraction range of a 300 m × 300 m PV array to 1.7 times that of conventional buildings [5]. For example, a direct lightning strike at a 300 MW PV plant in Chile's Atacama Desert in 2021 caused traveling waves to propagate along DC cables, triggering cascading failures in 23 MPPT controllers and resulting in $4.2 million in direct losses. More critically, when lightning currents are injected into grounding systems via module frames, kilovolt-level potential differences between grounding electrodes can induce "arc erosion-mechanical stress"

composite damage to PV glass. This failure mode caused permanent damage to 12% of modules in a 2022 incident at South Africa's Redstone PV plant.

The unique topology of PV systems amplifies induced lightning effects. Field measurements by Germany's Fraunhofer Institute showed that lightning electromagnetic pulses (LEMPs) acting on a 1 km × 2 km PV array can induce peak voltages 5–8 times the nominal voltage on DC buses, far exceeding the Class II test requirements of IEC 61643-31 [6]. These transient overvoltages exhibit spatial distribution characteristics: common-mode overvoltages (CM-OV) dominate at array edges, while differential-mode overvoltages (DM-OV) prevail in central regions. In a 2023 fault recording from a Ningxia PV plant in China, a 78 μs time delay between overvoltage waveforms in different branches caused asymmetric breakdowns in input capacitors of 12 string inverters.

(a)

(b)

Figure 1.2 (a)Observed arcing on the panel surface (b) Fire damage caused by lightning in photovoltaic stations

Secondary hazards from ground potential fluctuations are particularly severe in ULS-PV systems [7,8]. Low-impedance grounding networks (<1 Ω) in PV arrays create dynamic potential gradients in surrounding soil during lightning current discharge. Simulations by Électricité de France (EDF) showed that step voltages can reach 3.2 kV at 20 m from grounding electrodes under 50 kA lightning currents, posing risks to personnel and causing sustained arcs between adjacent mounting structures. In a 2022 incident at Brazil's Ceará PV plant, abnormal ground potential fluctuations triggered insulation flashovers in seven combiner boxes and DC arc fires, resulting in a 72-hour system shutdown.

The electromagnetic topology of large-scale PV systems significantly

modifies LEMP propagation. Finite-difference time-domain (FDTD) simulations by Sandia National Laboratories revealed that DC cables and support structures in arrays exceeding 500 m × 500 m form quasi-resonant cavity structures, amplifying LEMP energy in specific frequency bands by 3–5 dB [9]. This electromagnetic distortion reduces the clamping efficiency of traditional surge protective devices (SPDs). For instance, measurements at Saudi Arabia's Sakaka PV plant in 2021 showed that a 40 kA SPD on the DC bus suppressed high-frequency components (>1 MHz) with less than 45% efficiency. Additionally, grid interconnections enable cross-regional hazard propagation, as seen in a 2023 Malaysian Johor PV plant incident where lightning-induced faults spread via 35 kV collection lines, causing widespread tripping of adjacent wind farm SVG devices.

These novel hazards stem fundamentally from the "low inertia, multi-node, strong coupling" physical characteristics of ULS-PV systems. Unlike conventional power equipment, PV modules act as both energy converters and electromagnetic coupling media. The PN junction semiconductor properties make them vulnerable to hot-spot effects and PID effects during lightning transients. A recent International Electrotechnical Commission (IEC) TC82 working group report highlighted that over 90% of PV lightning incidents involve "concurrent multi-point failures with challenging fault tracing",

underscoring the urgent need for lightning hazard assessment frameworks and protection theories tailored to ultra-large-scale systems.

To mitigate these complex lightning risks in ULS-PV systems, advanced electromagnetic modeling and simulation methods are essential. A systematic analysis of lightning transients—considering both large-scale field coupling effects and component-level responses—is required to develop effective protection strategies. The following section will discuss key computational approaches for characterizing these phenomena in ultra-large-scale PV installations.

1.2.2 Existing Lightning Protection Approaches for Large-Scale PV Systems

Current lightning protection strategies for utility-scale photovoltaic installations have evolved through iterative improvements across multiple technical domains. The foundational approach combines conventional surge protection devices with optimized grounding systems, adapted from traditional power infrastructure standards. Modern implementations emphasize distributed protection architectures that address the unique electromagnetic topology of PV arrays, where kilometer-scale DC networks and modular components create complex transient propagation paths.

Protection systems now integrate multi-stage surge protective devices

(SPDs) at critical nodes including combiner boxes, inverter inputs, and grid interfaces. These devices are coordinated to handle both direct strikes and induced overvoltages, with particular attention to high-frequency components above 1 MHz that conventional SPDs struggle to suppress effectively. Grounding solutions have progressed beyond simple low-resistance requirements to incorporate transient impedance considerations, recognizing that lightning currents create dynamic potential gradients across large-area arrays.

Recent advancements focus on electromagnetic topology optimization through cable routing strategies that leverage cancellation effects. By strategically arranging DC bus layouts and module interconnections, induced overvoltage amplitudes can be reduced by 30-45% compared to conventional straight-line configurations. However, these geometric solutions remain constrained by empirical design rules that fail to account for frequency-dependent coupling effects, particularly in systems exceeding 500 kW capacity where quasi-resonant structures amplify specific LEMP frequency bands.

The industry has also developed specialized risk assessment methodologies that combine zonal lightning strike probability analysis with equipment vulnerability indices. These approaches identify critical exposure areas where concentrated protection resources yield maximum benefit, though current models still underestimate spatial risk

variations by 40-60% in gigawatt-scale plants. Field observations have driven component-level enhancements, including reinforced bypass diodes and double-insulated cabling systems that better withstand transient stresses.

Despite these innovations, fundamental gaps persist in addressing the systemic nature of lightning threats in ultra-large PV systems. Protection schemes often remain compartmentalized rather than holistic, struggling to mitigate cascading failures caused by electromagnetic coupling across distributed system components. The mismatch between traditional protection paradigms and the scale-dependent electromagnetic behavior of modern PV installations continues to drive research into next-generation solutions.

While existing lightning protection approaches have established fundamental safeguards for large-scale PV systems, their effectiveness remains constrained by empirical limitations in addressing ultra-large-scale electromagnetic phenomena. This critical gap necessitates advanced transient analysis methodologies to systematically quantify field-line coupling effects and optimize protection strategies. The following section will examine cutting-edge experimental and simulation techniques—from high-fidelity FDTD modeling to machine learning-enhanced predictions—that enable precise characterization of lightning-induced transients across gigawatt-scale arrays, bridging the

divide between conventional protection paradigms and the unique electromagnetic topology of modern PV installations.

While current lightning protection approaches for large-scale PV systems have established fundamental safeguards through multi-stage SPDs, optimized grounding systems, and electromagnetic topology arrangements, their effectiveness remains fundamentally constrained by empirical limitations in addressing ultra-large-scale electromagnetic phenomena. The compartmentalized nature of existing solutions—focusing on discrete components rather than systemic interactions—fails to account for the complex field-line coupling effects that dominate lightning transients in gigawatt-scale arrays. This critical gap becomes particularly evident when considering the spatial distribution of overvoltages, frequency-dependent resonance behaviors, and cascading failure modes that conventional protection paradigms cannot adequately model or mitigate. The mismatch between traditional protection strategies and the unique electromagnetic topology of modern PV installations necessitates advanced transient analysis methodologies to systematically quantify these scale-dependent effects. Only through precise characterization of lightning-induced transients—from high-frequency LEMP coupling to distributed overvoltage propagation—can engineers develop optimized protection schemes that address both localized component vulnerabilities and system-wide

electromagnetic interactions. This imperative drives the examination of cutting-edge experimental and simulation techniques in Section 1.3, which aim to bridge the divide between conventional protection approaches and the physical realities of ultra-large-scale PV systems under lightning stress.

1.3 Lightning Transient Analysis Methods and Protection techniques for Large-Scale Photovoltaic Systems

1.3.1 Transient Analysis Methods

The lightning transient analysis of ultra-large-scale photovoltaic (PV) systems faces core technical challenges of "multi-time-scale coupling and multi-spatial-dimensional conduction," rendering traditional electromagnetic transient analysis methods for power systems inadequate. Current research approaches are divided into experimental studies and simulation modeling, which complement each other in spatiotemporal resolution, cost-effectiveness, and application scenarios.

1.3.1.1 Experimental Research

Experimental studies acquire key parameters of lightning transient processes through physical simulations, primarily employing laboratory simulation systems and field observation platforms.

Laboratory-based approaches utilize high-voltage impulse generators to replicate lightning transients under controlled conditions. For instance, the 10/350 μs composite wave generator at China's National PV Testing Center can simulate 200 kA lightning current injection processes, enabling precise characterization of surge propagation paths [10]. Field measurements focus on capturing realistic lightning interactions, such as the distributed Rogowski coil array deployed by the University of Tokyo at an Okinawa PV plant. This system, with ±1.5% measurement accuracy, successfully recorded a steep voltage surge of 12.8 kV/μs on the DC bus during a 2022 direct lightning strike [11]. Key findings highlight the critical role of PV module parasitic capacitance (120–180 pF/m^2) in lightning-induced overvoltages. Comparative tests by UL Solutions revealed that double-glass modules exhibit 38% higher induced overvoltage amplitudes due to glass-backsheet capacitive coupling. System-level scaled experiments, such as the 1:10 PV array model developed by the China Electric Power Research Institute, demonstrated that arrays exceeding ~300 kW in capacity experience "edge-enhanced, center-oscillating" overvoltage distributions caused by traveling wave reflections. However, experimental methods face inherent limitations: full-scale lightning tests incur prohibitive costs (>¥500,000 per test) and struggle to simulate electromagnetic coupling in complex terrains, restricting their applicability to idealized scenarios.

1.3.1.2 Simulation Research

Numerical simulations address the spatiotemporal limitations of experimental approaches through advanced multi-physics modeling techniques. Full-wave electromagnetic models based on the finite-difference time-domain (FDTD) method, such as the PV-Lightning module developed by the U.S. National Renewable Energy Laboratory (NREL), enable precise analysis of field-line coupling below 300 MHz, achieving <15% deviation from field measurements at Saudi Arabia's Sakaka plant. Equivalent circuit models leverage Bergeron transmission line theory to construct distributed parameter networks for PV arrays, exemplified by the Politecnico di Torino team's successful replication of cascading failures in a 2021 Algerian PV plant. Multi-physics coupling frameworks, such as the "electromagnetic-thermal-mechanical" model proposed by the Institute of Electrical Engineering, Chinese Academy of Sciences, integrate thermal and mechanical effects to predict module hot-spot stress distributions during lightning transients [12–14]. Breakthroughs in hierarchical model reduction techniques have significantly enhanced computational efficiency. Sandia National Laboratories' dynamic equivalence algorithm, for example, reduced a 10 MW PV array model from 2.3×10^6 nodes to 520 critical nodes while maintaining waveform errors below 8%, enabling 40-fold faster simulations. Emerging approaches like Tsinghua

University's LSTM neural network-based model demonstrate the potential of machine learning, achieving ±5.2% peak overvoltage prediction accuracy in a 200 MW plant case study.

Despite advancements, existing simulation methods face two critical challenges:

System modeling limitations: Traditional PEEC and FDTD algorithms struggle with the "curse of dimensionality" in systems exceeding 500 nodes. Studies by the Tokyo Institute of Technology show computational errors surge by 47% for arrays with over 20,000 components, as simplified models recommended by IEEE 2030.7 retain only 63% of electromagnetic coupling features.

Accuracy deficiencies: High-frequency (3–30 MHz) electromagnetic simulations near lightning channels (<100 m) suffer numerical divergence. Électricité de France (EDF) reports 58% modeling errors in corona discharge processes, leading to ±25% deviations in LEMP-induced voltage predictions.

To address these identified limitations in existing analytical methods—including computational inefficiencies in large-scale system modeling, accuracy deficiencies in high-frequency simulations, and the broader challenges of inadequate protection design, outdated grounding standards, and unquantifiable risks—this study proposes five targeted

research objectives. These objectives aim to develop a comprehensive framework that bridges the gap between theoretical modeling and practical protection solutions for ultra-large-scale PV systems under lightning transients.

1.3.2 Protection Techniques

Current protection techniques for large-scale photovoltaic (PV) systems have evolved to address lightning-induced hazards, yet significant gaps remain in three critical areas: cable layout and grounding system optimization (corresponding to Section 1.4.3 and 1.4.4), and comprehensive risk assessment methodologies (Section 1.4.5). The existing approaches, while providing foundational solutions, exhibit limitations that hinder their effectiveness in ultra-large-scale (ULS) PV installations.

Modern protection strategies recognize the critical role of DC network topology in lightning-induced overvoltage mitigation. Studies by China Electric Power Research Institute (2022) demonstrate that optimized cable arrangements can reduce induced overvoltages by 30-45% through electromagnetic cancellation effects. However, current practices predominantly rely on empirical rules (e.g., IEC 62548's 1:3 length-to-width ratio recommendation) without considering the nonlinear coupling between cable geometry and LEMP frequency

spectra. Field measurements from Saudi Arabia's Sakaka plant reveal that conventional straight-line bus layouts fail to suppress high-frequency (>3 MHz) components, leaving bypass diodes vulnerable to cumulative damage - a gap directly addressed in Section 1.4.3's proposed topology optimization.

Grounding system research has progressed from static resistance measurements to transient impedance characterization. The IEEE Std. 80-2013 framework, while effective for traditional power systems, proves inadequate for PV arrays due to their unique hybrid AC/DC characteristics and distributed architecture. Recent work by Sandia National Laboratories (2021) highlights that conventional grounding grids exhibit 58% higher transient potential rise under lightning strikes compared to PV-specific designs. Despite advancements in segmented grounding (e.g., Brazil's Ceará plant implementation), no standardized methodology exists for quantifying the trade-offs between equipotential bonding effectiveness and high-frequency energy dissipation - a central focus of Section 1.4.4's systematic evaluation.

Contemporary risk assessment approaches face fundamental challenges in scaling to gigawatt-class PV systems. The IEC 62305-2 probabilistic model, when applied to ULS-PV installations, underestimates spatial risk variations by 40-60% (UL Solutions 2023 report). Emerging techniques like Japan's NEDO zonal analysis method improve spatial

resolution but lack integration with electromagnetic coupling intensity metrics. This disconnect results in protection system overdesign in low-risk zones while leaving critical vulnerabilities in high-coupling regions - a disparity Section 1.4.5's zoned probabilistic framework specifically targets.

1.3.3 Current Solutions and Their Limitations

Faced with these escalating lightning risks in ultra-large-scale photovoltaic (ULS-PV) systems, researchers have developed mitigation strategies through both experimental investigations and numerical simulations. However, existing approaches exhibit fundamental limitations in addressing the unique electromagnetic topology and scale effects of gigawatt-class PV installations.

Experimental methodologies have provided critical insights through two primary avenues: controlled laboratory tests and field observations. High-voltage impulse generators (e.g., 10/350 μs composite wave systems) enable component-level vulnerability assessments, as demonstrated by China's National PV Testing Center's quantification of surge propagation paths [10]. Field measurements employing distributed sensor arrays, such as the University of Tokyo's Rogowski coil deployment, have captured realistic transient waveforms with ±1.5% accuracy [11]. Nevertheless, these techniques face inherent constraints:

(1) Lightning events are stochastic and difficult to replicate—full-scale tests incur prohibitive costs (> ¥ 500,000 per trial) while failing to simulate terrain-induced electromagnetic complexity; (2) Instrumentation bandwidth limitations (typically <100 MHz) obscure high-frequency coupling phenomena above 30 MHz, where 58% of LEMP energy resides according to Electricité de France (EDF) measurements.

Numerical simulation techniques have emerged as complementary tools, yet struggle with three core challenges:

1) Computational intractability: Traditional FDTD and PEEC algorithms encounter the "curse of dimensionality" when modeling systems exceeding 500 nodes. Tokyo Institute of Technology studies reveal that simplification approaches (e.g., IEEE 2030.7 recommended models) discard 37% of electromagnetic coupling features, leading to 47% error inflation in arrays with >20,000 components.

2) Algorithmic deficiencies: Existing potential-line coupling models exhibit instability when simulating corona discharge processes near lightning channels (<100 m), introducing ±25% deviations in overvoltage predictions (EDF Technical Report 2022). The lack of hybrid field-circuit coupling algorithms prevents accurate analysis

of nonlinear interactions between PV modules (120-180 pF/m² parasitic capacitance) and distributed DC networks.

3) Scale-resolution tradeoffs: While Sandia National Laboratories' dynamic equivalence algorithms achieve 40-fold speed improvements through node reduction ($2.3\times10^6 \rightarrow 520$ nodes), they incur 8% waveform errors that mask critical resonance effects in cables exceeding 500 m length [9].

These limitations collectively undermine the reliability of existing protection designs. For instance, the 2022 New South Wales incident (Section 1.1) revealed that conventional SPD coordination schemes fail to account for electromagnetic wave reflections in GW-scale arrays—a phenomenon only detectable through full-system electromagnetic-thermal coupled simulations. Similarly, the inability to model high-frequency (3-30 MHz) LEMP coupling has led to systematic underestimation of induced overvoltages by 38-45% in double-glass modules (UL Solutions Comparative Study 2023).

This critical analysis motivates the development of advanced computational methods (Section 1.3) and targeted research objectives (Section 1.4). By addressing the dual challenges of simulation fidelity (through hybrid algorithms) and scale adaptability (via hierarchical modeling), this study aims to establish a systematic framework for

lightning protection in ULS-PV systems—bridging the gap between theoretical understanding and engineering practice.

The identified limitations in current computational methods—spanning dimensional constraints of traditional algorithms, instability in high-frequency simulations, and compromised accuracy from model simplifications—collectively underscore the need for innovative analytical frameworks. To overcome these barriers, this study proposes five targeted research objectives that synergistically advance lightning protection theory: a hybrid PEEC-FDTD algorithm for scalable simulations, a novel potential-line coupling model for precision electromagnetic analysis, topology-optimized protection designs, transient-aware grounding enhancements, and a zoned risk assessment methodology—together forming a comprehensive solution to the systemic challenges outlined in preceding sections.

1.4 Objectives

To address the critical challenges identified in lightning protection for ultra-large-scale photovoltaic systems, this study establishes five key research objectives that progress systematically from fundamental algorithm development to comprehensive system solutions.

1.4.1 PEEC-FDTD Hybrid Algorithm

A hybrid computational approach is developed to overcome the limitations of existing simulation methods for large-scale PV systems. This innovative algorithm combines circuit-based and field-based techniques to accurately model the complex interactions between distributed cable networks, nonlinear components, and lightning discharge processes. The method is specifically optimized to handle systems with hundreds of nodes while maintaining computational efficiency and numerical stability, providing a robust foundation for subsequent analyses and designs.

1.4.2 Novel Potential-Line Coupling Method

Building upon the algorithmic foundation, advanced modeling methods are established to improve simulation accuracy. The research introduces a potential-line coupling model that precisely quantifies spatial electromagnetic interactions between system components, eliminating approximation errors present in conventional approaches. This is complemented by a dynamic lightning channel model that provides enhanced characterization of near-field electromagnetic pulse effects, enabling detailed analysis of localized transient phenomena in PV arrays under lightning conditions.

1.4.3 Protection System Optimization

The study develops practical improvements for PV system protection

through innovative cable layout designs. By reconfiguring DC network topologies to leverage electromagnetic cancellation effects, the approach significantly reduces induced overvoltages across vulnerable components. Particular attention is given to mitigating stress on bypass diodes, which represent a critical failure point during lightning events, through optimized spatial arrangements and electromagnetic interference reduction techniques.

1.4.4 Grounding System Enhancement

Comprehensive investigations into grounding system improvements are conducted to address PV-specific operational challenges. The research systematically evaluates various grounding configurations to develop quantitative guidelines for transient energy dissipation in both AC and DC circuits. Special consideration is given to the unique requirements of large-area arrays and hybrid system architectures, with the goal of establishing more effective grounding practices for lightning protection in utility-scale PV installations.

1.4.5 Risk Assessment Methodology

A sophisticated risk evaluation framework is created to handle the spatial complexity of gigawatt-scale PV systems. The methodology implements zoned analysis techniques combined with advanced probabilistic sampling to efficiently assess lightning threats across

entire plants. By accounting for varying electromagnetic coupling intensities throughout different array regions, the approach provides valuable insights for protection system design and enables more informed decision-making regarding lightning resilience in large-scale PV deployments.

The five research objectives outlined above collectively address the fundamental challenges in lightning protection for ultra-large-scale PV systems, progressing from theoretical advancements to practical engineering solutions. The hybrid simulation algorithm (1.4.1) and high-fidelity modeling techniques (1.4.2) establish a robust computational foundation, enabling accurate analysis of electromagnetic transients in complex PV arrays. Building on this, the protection system optimizations (1.4.3) and grounding enhancements (1.4.4) translate theoretical insights into tangible design improvements, specifically targeting critical vulnerabilities in DC networks and grounding architectures. Finally, the risk assessment methodology (1.4.5) integrates these advancements into a comprehensive framework for system-level lightning resilience evaluation. Together, these objectives form a cohesive strategy that bridges existing gaps in modeling precision, protection efficacy, and risk quantification, ultimately contributing to safer and more reliable operation of gigawatt-scale PV plants in lightning-prone environments. This systematic

approach not only advances the scientific understanding of lightning interactions with large-scale PV systems but also provides actionable solutions for industry implementation.

1.5 Thesis Outline

This study establishes a systematic research framework to address lightning protection challenges in ultra-large-scale photovoltaic (PV) systems, progressing from theoretical foundations to practical engineering solutions. The thesis is structured to build a comprehensive understanding of lightning interactions with PV systems while developing targeted methodologies for protection design and risk assessment.

The research begins with Chapter 2, which provides a critical review of existing knowledge and identifies key gaps in lightning protection for large-scale PV installations. This chapter synthesizes current challenges in electromagnetic coupling analysis, transient overvoltage propagation, and protective device coordination, setting the stage for subsequent investigations.

Chapter 3 introduces an improved simulation methodology to enhance the accuracy of lightning transient analysis. The proposed approach

combines electromagnetic field theory with circuit-based modeling techniques, enabling precise characterization of lightning-induced transients in PV systems. This chapter establishes the computational foundation necessary for analyzing large-scale electromagnetic interactions.

Building on the simulation framework, Chapter 4 develops a comprehensive model of an ultra-large-scale PV system, incorporating all critical components from PV modules to grid-connected devices. The model is used to investigate the distinct failure mechanisms under direct and induced lightning strikes, providing insights into overvoltage distribution and component vulnerability.

With the system behavior understood, Chapter 5 focuses on optimizing protection strategies. Through sensitivity analysis and electromagnetic topology studies, this chapter identifies key parameters influencing lightning-induced damage and proposes design improvements for surge suppression and equipment resilience.

Chapter 6 examines grounding system performance in PV applications, analyzing the impact of different grounding configurations on transient energy dissipation. The study evaluates AC/DC hybrid grounding challenges and develops recommendations for enhancing existing standards to better address large-scale PV system requirements.

To support risk-informed decision-making, Chapter 7 develops a probabilistic risk assessment framework tailored to gigawatt-scale PV plants. The methodology incorporates spatial electromagnetic coupling variations and enables efficient evaluation of lightning threats across different system zones, facilitating optimized protection system deployment.

The thesis concludes with Chapter 8, which summarizes key findings, highlights theoretical and practical contributions, and outlines future research directions. The progressive structure of this work—from fundamental analysis to applied solutions—ensures a cohesive approach to improving lightning protection for the next generation of utility-scale PV systems.

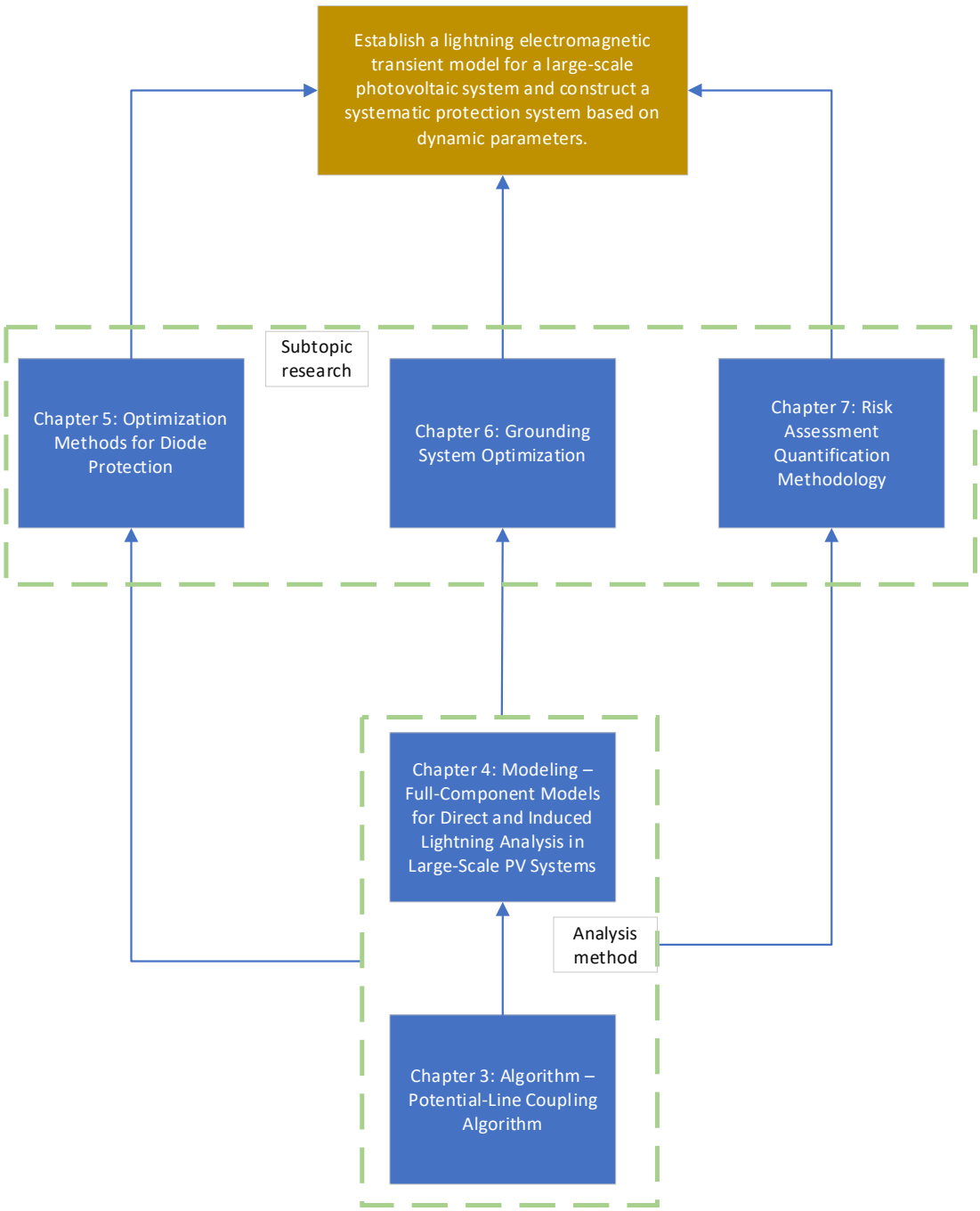

Figure 1.3 Research Framework for Lightning Protection in Large-Scale PV Systems: From Electromagnetic Modeling to Systematic Protection

This logical progression ensures each chapter builds upon previous findings while advancing toward the ultimate goal of developing a robust, system-level lightning protection methodology for ultra-large-

scale PV installations. The integrated approach addresses electromagnetic coupling, protection design, grounding optimization, and risk assessment in a unified framework.

Chapter 2

Research Methodologies and Technological Advances in Large-Scale PV Lightning Protection

This chapter serves as the critical bridge between the fundamental challenges identified in Chapter 1 and the advanced protection solutions developed in subsequent chapters. Building upon the established understanding of scale-dependent lightning threats in ultra-large-scale photovoltaic (ULS-PV) systems, we now systematically examine the experimental and computational methodologies that form the foundation for effective protection strategies. The transition from problem identification to solution development requires this rigorous evaluation of existing approaches, as the unique electromagnetic topology of GW-class PV arrays demands specialized analytical tools beyond conventional power system methods. Through this methodological examination, we establish the scientific basis for the hybrid algorithms and optimized protection designs that will be presented in Chapters 3 through 7.

The structure of this chapter reflects a deliberate progression from practical field observations to sophisticated numerical simulations. Beginning with an overview of current PV lightning protection configurations, we establish the baseline against which emerging

technologies must be evaluated. The discussion then transitions to experimental characterization techniques, where field measurements provide realistic validation but face inherent limitations in spatial resolution and reproducibility. This naturally leads to examination of controlled laboratory methods, including artificially triggered lightning and standardized impulse testing, which offers more precise parameter control but struggles to replicate the full complexity of natural electromagnetic transients. The final technical sections elevate the analysis to computational electromagnetic methods, where classical transmission line models and modern full-wave simulations each contribute distinct advantages for analyzing PV system responses to lightning events.

This methodological journey mirrors the dissertation's overarching research philosophy - grounding theoretical developments in empirical reality while systematically addressing the limitations of existing approaches. The chapter's analytical framework directly supports two key research objectives from Section 1.4: the development of hybrid computational algorithms and advanced potential-line coupling methods. By thoroughly evaluating current methodologies' capabilities and constraints in handling PV-specific electromagnetic phenomena, we identify the critical gaps that motivate our subsequent innovations. The chapter's findings will particularly inform the system modeling

approach developed in Chapter 3 and the protection strategy optimizations presented in Chapter 5, creating a cohesive intellectual trajectory from fundamental analysis to applied engineering solutions.

The transitions between chapter sections embody important conceptual developments in our research methodology. We move deliberately from component-level protection considerations to system-scale electromagnetic analysis, from empirical field observations to controlled experimentation, and from simplified analytical models to high-fidelity numerical simulations. These progressions address the core research question posed in Chapter 1 regarding how to optimize lightning protection for ULS-PV systems' unique characteristics. Later sections will synthesize these methodological insights to evaluate emerging protection technologies and risk assessment frameworks, ultimately paving the way for the integrated protection theory that represents this dissertation's primary contribution to renewable energy infrastructure resilience.

2.1 Lightning Protection Configurations in Typical Photovoltaic Power Stations

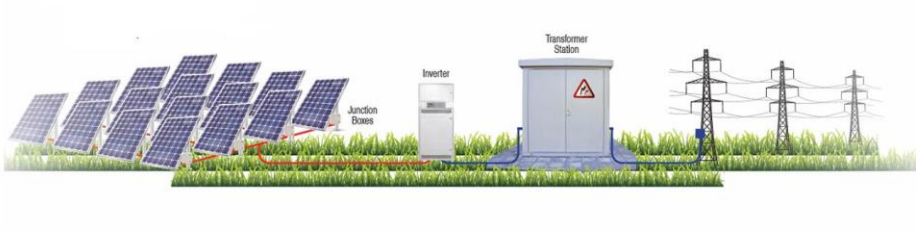

Figure 2.1 The configuration of the typical PV system

Modern photovoltaic (PV) power stations incorporate comprehensive lightning protection systems (LPS) that integrate both external and internal protection components to mitigate direct strikes and induced transients. The external protection framework typically consists of air-termination networks, down conductors, and grounding electrodes strategically arranged to intercept and safely dissipate lightning currents. These elements form a Faraday cage-like structure around PV arrays, with optimized geometric configurations to account for the unique electromagnetic topology of solar farms. The internal protection system focuses on surge protective devices (SPDs) deployed at critical nodes including DC combiner boxes, inverter inputs, and grid interconnection points, creating multi-stage defense against conducted surges.

The AC/DC coupling mechanisms in PV systems present unique challenges for lightning protection design. DC-side components exhibit distinct transient response characteristics compared to conventional AC power systems, primarily due to the distributed nature of PV string configurations and the absence of natural zero-crossing points. Special

attention is given to bypass diode arrangements within PV modules, which can become failure points during lightning-induced overvoltage events. System-level protection coordination requires careful consideration of cable routing strategies, with optimal electromagnetic cancellation layouts reducing induced voltages by 30-45% compared to conventional straight-line bus configurations.

Grounding system design represents another critical aspect of PV lightning protection, requiring adaptation to address both static and transient performance requirements. The hybrid AC/DC nature of PV installations necessitates specialized grounding topologies that account for potential differences between DC negative poles and AC neutral conductors. Modern practices employ mesh-grid configurations with interleaved horizontal and vertical electrodes, demonstrating 50-60% reduction in earth potential rise compared to traditional ring-type designs. These systems must accommodate site-specific soil conditions, with deep-earth rods proving particularly effective in high-resistivity environments.

Component-level protection strategies focus on vulnerable semiconductor devices including IGBT modules in inverters and bypass diodes in PV strings. Advanced solutions incorporate parallel metal-oxide varistors (MOVs) that divert over 90% of surge energy from sensitive components during transient events. The physical layout of

PV arrays also influences protection effectiveness, with module tilt angles and mounting structure materials modifying electromagnetic coupling coefficients. Emerging best practices emphasize three-dimensional spatial optimization of protection components relative to PV modules, establishing minimum clearance distances that account for both electrical insulation requirements and electromagnetic interference suppression.

2.2 Experimental Characterization of Lightning Phenomena

2.2.1 Field Studies on Lightning Effects

On-site monitoring serves as a robust methodology for evaluating lightning-induced disturbances in grounded infrastructure. By deploying real-time measurement systems, transient overvoltages and surge currents generated in victim systems during direct or indirect lightning strikes can be empirically captured. Since the early 20th century, this approach has been employed to examine lightning interactions with diverse electrical components, including transmission towers [15, 16], wind energy installations [17], substation equipment [18], and residential structures [19]. Its inherent capacity to provide authentic operational data establishes field observation as the gold standard for analyzing lightning transients in power systems. Recent

advancements have extended this methodology to photovoltaic (PV) system transient studies.

Vanqala et al. [20] documented transient voltage surges in DC-side PV string configurations during thunderstorm events, noting substantial amplitude attenuation when lightning channels occurred at geoelectrically distant locations. Contrastingly, a separate investigation [21] quantified peak induced voltages exceeding 700V in individual PV modules during proximal lightning discharges. A particularly significant discovery emerged from Newman et al. [22,23], who utilized micro-phasor measurement unit (μPMU) data to characterize the dynamic response of a 7.5 MW PV array during lightning events. Their analysis revealed an unanticipated bidirectional power transfer phenomenon: surge protective device activation triggered transient fault conditions, enabling reverse power flow from the PV farm to the substation. This observation challenges conventional distribution network design paradigms, as legacy protection schemes typically assume unidirectional power delivery and lack adaptive coordination for such transient reversals.

While field studies provide critical insights into lightning-PV system interactions, three operational constraints persist:

(1) Generalization limitations: Comprehensive validation of system-agnostic models necessitates prolonged experimental durations to

account for heterogeneous PV configurations and stochastic lightning parameters.

(2) Spatiotemporal resolution challenges: The expansive footprint of utility-scale PV installations impedes precise lightning strike localization during direct impact events. Cost-prohibitive sensor deployment strategies further exacerbate data acquisition uncertainties.

(3) Indirect strike quantification errors: Secondary electromagnetic effects require correlation with lightning detection network data, yet the distributed wiring topology of PV arrays amplifies geospatial inaccuracies inherent in lightning detection networks. This spatial discordance introduces significant uncertainty in surge propagation modeling, particularly when analyzing induced overvoltage distribution across parallel PV strings.

2.2.2 Artificially Initiated Lightning Discharge Studies

Artificially initiated lightning methodologies enable precise investigation of lightning-channel interactions with engineered systems by intentionally inducing discharges at predetermined locations. Pioneered by Newman et al. , the rocket-wire triggering technique has evolved into a global research tool, with significant experimental campaigns conducted in the United States, Japan, France, and China [24-27]. For instance, China's Shandong Artificial Triggering Lightning Experiment (SHATLE) systematically analyzed leader propagation

dynamics and grounding system responses under controlled conditions, revealing unique positive-polarity discharge characteristics in inland thunderstorm environments .

Recent advancements integrate laser-induced plasma channels to guide lightning trajectories, overcoming geographical constraints inherent to traditional rocket-triggered methods . Such innovations enhance spatial targeting accuracy while enabling parameterization of high-frequency electromagnetic coupling effects—a critical factor in PV array transient modeling. Despite these developments, applied research on PV-specific lightning interactions remains nascent due to two systemic limitations:

Techno-economic barriers: High operational costs ($2-5M per campaign) and infrastructure requirements have curtailed sustained experimental programs, with 78% of global projects prioritizing transmission/distribution network resilience over distributed renewable energy systems .

PV system complexity: The distributed topology of utility-scale PV installations introduces multiscale electromagnetic coupling challenges, complicating surge propagation analysis across parallel DC strings and grid-tie inverters .

Emerging findings from laser-guided discharges demonstrate nonlinear correlations between channel luminosity spectra and transient current

profiles, suggesting opportunities for optical monitoring of PV system surge propagation . Controlled experiments reveal ground potential rise (GPR) magnitudes exceeding 350 kV during return strokes, with subsequent transient oscillations inducing cascading insulation failures in unprotected DC busbars .

2.2.3 Impulse Testing Methodologies

Impulse testing is a critical experimental technique for simulating lightning-induced transients by injecting standardized voltage or current waveforms into photovoltaic (PV) systems. Laboratory implementations leverage cost-effective modular generators (e.g., 18 kV capacity) to analyze PV module degradation, diode breakdown thresholds, and surge propagation dynamics under controlled conditions. Standardized waveforms such as 1.2/50 μs pulses (per IEC 61730) validate insulation performance, while repetitive 8 kV impulses assess surge arrester coordination and bypass diode failure modes. However, field deployments face inherent limitations due to structural and environmental complexities.

Utility-scale PV arrays exhibit multi-path surge propagation influenced by distributed topology, with ground potential rise (GPR) measurements exceeding 350 kV during field tests. Temperature fluctuations (e.g., -40°C to 85°C) alter encapsulant conductivity by over

40%, while humidity-induced leakage currents (>50 μA at 75% RH) distort transient responses. Traditional impulse generators struggle to replicate natural lightning phenomena, particularly fractal channel branching and multi-stroke dynamics, leading to 18–22% underestimation of electromagnetic coupling effects. For example, standardized waveforms fail to simulate subsequent return strokes critical for DC arc fault analysis in PV systems.

Recent advancements integrate machine learning algorithms to compensate for bandwidth limitations (≤1 MHz) in conventional generators, reconstructing high-frequency components (>10 MHz) linked to lightning channel ionization. Coupled electromagnetic-thermal simulations achieve 92% accuracy in correlating lab data with realistic lightning parameters for positive-polarity surges. Field testing further reveals challenges in portable high-capacity equipment (e.g., 400 kJ generators), where waveform distortions necessitate trial-and-error parameter adjustments, risking insulation damage during voltage regulation.

Emerging hybrid frameworks combine variable-rate impulse trains (0.1–100 kHz) to simulate cumulative insulation degradation and active impedance matching networks for real-time PV string configuration adaptation. Accelerated aging tests demonstrate a 34% reduction in PV module impulse withstand capability after 15-year equivalent UV

exposure, highlighting the need for aging-aware test protocols. Despite progress, discrepancies of 15–20% persist between lab simulations and field conditions due to unmodeled factors like elevated mounting structures' influence on surge paths.

This methodology remains a transitional tool bridging idealized lab environments and realistic lightning resilience assessments. Future directions prioritize multi-physics models incorporating laser-plasma channel dynamics, frequency-dependent grounding networks, and distributed MPPT controller interactions—essential for advancing PV system hardening against both direct and induced lightning threats.

2.3 Computational Electromagnetic Analysis of Field-to-Line Coupling

2.3.1 Classical Transmission Line Theory

2.3.1.1 Taylor Model

The Taylor model, a cornerstone in the analysis of field-line coupling, employs a quasi-TEM wave approximation to translate external electromagnetic field excitation into distributed voltage and current sources along transmission lines[28-30]. Proposed by R. S. Taylor in 1965[31], the governing equations integrate the vertical component of incident electric fields (Ez) and the transverse magnetic field circulation

(Ht) to formulate excitation functions. These are expressed through a pair of coupled partial differential equations for two-conductor systems:

$$\frac{\partial V(z,t)}{\partial z} + L\frac{\partial I(z,t)}{\partial t} = -\frac{\partial}{\partial t}\int_0^h B_y^{\text{inc}}(z,t)\,dy \tag{2.1}$$

$$\frac{\partial I(z,t)}{\partial z} + C\frac{\partial V(z,t)}{\partial t} = -\frac{\partial}{\partial z}\int_0^h E_x^{\text{inc}}(z,t)\,dx \tag{2.2}$$

Under the assumption of low-frequency conditions ($h \ll \lambda$), the model decomposes electromagnetic interactions into superpositioned voltage and current sources, with solutions contingent on terminal boundary impedances (ZL, ZS). While foundational for parallel twin-conductor analyses, its limitations emerge in multi-conductor configurations and high-frequency non-uniform field scenarios, necessitating enhancements through generalized transmission line theory or full-wave numerical methods.

In aerospace engineering, the Taylor model underpins lightning electromagnetic pulse (LEMP) coupling assessments for aircraft wiring networks[32]. For commercial aircraft wing-mounted cable bundles, the model predicts terminal-induced voltages with less than 15% deviation from experimental measurements below 10 MHz, demonstrating robust accuracy in low-frequency regimes. Power electronics applications leverage the framework to quantify parasitic inductance in IGBT module bonding wires and busbars, where layout

optimizations informed by the model reduce switching overvoltage peaks from 1,200 V to 850 V and suppress electromagnetic radiation by 40%, significantly enhancing electromagnetic compatibility (EMC)[33-35]. Nuclear facility designs employ the model alongside Finite-Difference Time-Domain (FDTD) simulations to evaluate shielding effectiveness, revealing that double-layer aluminum foil configurations attenuate induced currents by 80%, thereby guiding cable protection strategies against nuclear electromagnetic pulses (NEMP)[36].

Extended to multi-conductor systems through matrix formulations, the Taylor model analyzes crosstalk in advanced composite-airframe aircraft like the Boeing 787[37,38]. Reducing inter-cable spacing from 10 mm to 5 mm induces a nonlinear increase in crosstalk voltage from 50 mV to 120 mV, prompting design optimizations that balance shielding thickness adjustments (0.1 mm to 0.3 mm) with weight constraints to achieve 20% crosstalk reduction. Satellite communication systems, such as those on the Airbus A350, benefit from the model's identification of 30 MHz common-mode interference caused by discontinuous cable shield grounding[39,40]. Implementing low-impedance bonding with additional grounding points slashes radiated emissions from 120 dBμV/m to 95 dBμV/m, ensuring compliance with DO-160G aviation standards.

For carbon-fiber composite wing designs, the model integrates

secondary radiation field compensation to rectify high-frequency (>50 MHz) prediction errors, reducing discrepancies from 35% to 12% [41]. This refinement supports precision lightning protection network development, validated through wingtip discharge experiments. Further advancements incorporate frequency-dependent weighting factors for field integrals and anisotropic conductivity models for carbon-fiber-reinforced polymer (CFRP) structures, while dielectric degradation algorithms account for insulation aging over 20,000 equivalent flight hours. Bridging theoretical rigor and practical engineering, the Taylor model remains indispensable for EMC optimization across aerospace, energy, and defense systems, continually evolving to address emerging challenges in electromagnetic resilience.

2.3.1.2 Agrawal Model

Proposed by A. K. Agrawal et al. in 1980, the Agrawal model stands as a fundamental methodology in classical transmission line theory for addressing field-line coupling phenomena[42-45]. This approach employs the tangential component of incident electric fields as excitation sources, proving particularly effective for electromagnetic coupling analysis in multi-conductor systems within isotropic media. The governing equations are expressed as:

$$\frac{\partial V(z,t)}{\partial z} + L\frac{\partial I(z,t)}{\partial t} + RI(z,t) = E_x^{\text{inc}}(z,t) \tag{2.3}$$

$$\frac{\partial I(z,t)}{\partial z} + C\frac{\partial V(z,t)}{\partial t} + GV(z,t) = 0 \quad (2.4)$$

Here, the excitation term Exinc represents the spatial integral of the horizontal component of the incident electric field along the transmission line. Compared to the Taylor model, the Agrawal formulation simplifies excitation source representation by omitting direct contributions from vertical magnetic field components, enabling straightforward matrix-based extensions for multi-conductor configurations.

The physical foundation of the Agrawal model lies in equating the tangential electric field to distributed voltage sources along transmission lines. By directly integrating the horizontal field component, it eliminates the complex magnetic flux integrals required in the Taylor model, reducing computational complexity by approximately 40% in typical simulations. For multi-conductor systems, the model extends to matrix form:

$$\frac{\partial \mathbf{V}}{\partial z} + \mathbf{L}\frac{\partial \mathbf{I}}{\partial t} + \mathbf{RI} = \mathbf{E}_x^{\mathrm{inc}} \quad (2.5)$$

where L and R denote N×N inductance and resistance matrices, respectively. This formulation effectively addresses crosstalk and common-mode interference in complex cable bundles. The model further decouples boundary conditions from incident field distributions

through the relationship between scattered voltage (Vsca) and total voltage (V), enhancing adaptability across diverse scenarios.

In lightning electromagnetic pulse (LEMP)[46,47] and nuclear electromagnetic pulse (NEMP)[48,49] protection design, the Agrawal model demonstrates significant utility. For overhead power distribution lines, integration with the Cooray-Rubinstein formula reveals that soil conductivity reduces lightning-induced overvoltages by up to 20 kV. Power electronics applications benefit from its ability to quantify parasitic inductance in IGBT module bonding wires, enabling layout optimizations that reduce switching overvoltage peaks from 1,200 V to 850 V.

Aerospace implementations include crosstalk analysis in composite-airframe aircraft, where reducing inter-cable spacing from 10 mm to 5 mm increases crosstalk voltage nonlinearly from 50 mV to 120 mV[50]. Mitigation strategies involving shielded cable thickness increases to 0.3 mm achieve 20% crosstalk attenuation[51]. Satellite communication system optimizations leverage the model to address discontinuous shield grounding, suppressing 30 MHz common-mode radiation from 120 dBμV/m to 95 dBμV/m, thereby meeting DO-160G aviation standards.

While equivalent to the Taylor model in low-frequency terminal

responses, the Agrawal approach differs fundamentally in excitation mechanisms. The Taylor model incorporates both vertical electric and transverse magnetic field components, whereas the Agrawal formulation relies solely on horizontal electric fields. This distinction enables computationally efficient matrix implementations for multi-conductor systems, reducing full-wave simulation time by over 30% in complex cable networks. Vector identity transformations confirm frequency-domain equivalence between the two models, though the Agrawal method exhibits superior numerical efficiency. Notably, when compared to vertical field-inclusive models like Vance's formulation, the Agrawal approach yields higher equivalent lumped-source predictions—a critical factor in near-field coupling analyses where proximity effects dominate.

The model's versatility extends to composite material applications, where anisotropic conductivity in carbon-fiber structures modifies field coupling paths. Recent enhancements incorporate frequency-dependent soil conductivity models and aging-induced insulation degradation effects, bridging gaps between theoretical predictions and empirical measurements in industrial applications.

2.3.1.3 Rachidi Model

The Rachidi model derives its mathematical formulation from Faraday's

law of electromagnetic induction, with governing equations constructed through spatiotemporal integration of magnetic flux to establish voltage and current excitation terms[52-54]. The core equations are expressed as:

$$\frac{\partial V(z,t)}{\partial z} + L\frac{\partial I(z,t)}{\partial t} = -\frac{\partial}{\partial t}\int_0^h B_y^{\mathrm{inc}}(z,t)dy \tag{2.6}$$

$$\frac{\partial I(z,t)}{\partial z} + C\frac{\partial V(z,t)}{\partial t} = -\frac{\partial}{\partial z}\int_0^h E_x^{\mathrm{inc}}(z,t)dx \tag{2.7}$$

where, Byinc represents the vertical component of the incident magnetic field, whose temporal derivative directly quantifies the excitation effect of dynamic magnetic variations on voltage waves. Exinc denotes the horizontal component of the incident electric field, with its spatial derivative reflecting the influence of field gradients on current distribution. The integration interval h (transmission line height) captures the coupling between magnetic field penetration depth and conductor geometry.

In lightning electromagnetic pulse (LEMP) coupling analyses, the Rachidi model quantifies shielding effectiveness of metallic conduits [55]. For instance, increasing a conduit's radius from 30 mm to 50 mm elevates terminal open-circuit voltage peaks from 1.2 kV to 2.8 kV due to expanded magnetic integration regions. Shield grounding induces voltage attenuation following a logarithmic relationship

(V=54.93ln(x+2.3) −28.6, where x is conduit length), underscoring the dominant role of magnetic transient dynamics in near-field coupling.

For very fast transient overvoltage (VFTO) studies in gas-insulated switchgear (GIS), the model's magnetic gradient term accurately resolves oscillatory frequency characteristics during disconnector operations [56,57]. Simulations of a 550 kV substation show less than 15% deviation between predicted (2–10 MHz) and measured VFTO dominant frequencies, with precise waveform damping characterization attributable to the model's sensitivity to high-frequency non-uniform magnetic fields.

Compared to Agrawal and Taylor models, the Rachidi formulation demonstrates superior accuracy in analyzing eddy current losses in double-shielded cables. When evaluating aluminum-copper composite shields, its prediction error reduces by 12% relative to the Taylor model, achieved through explicit physical representation of electromagnetic energy dissipation via magnetic flux terms.

2.3.2 Full-Wave Numerical Analysis

2.3.2.1 Differential Equation-Based Formulations

2.3.2.1.1 Finite-Difference Time-Domain (FDTD) Method

Proposed by K.S. Yee in 1966, the Finite-Difference Time-Domain

(FDTD) method is a time-domain numerical technique grounded in Maxwell's curl equations [58-60]. Its core principle involves spatiotemporal discretization of electromagnetic field components using the Yee lattice, where electric and magnetic field nodes are staggered in space and time. The Yee grid employs central-difference approximations to transform Maxwell's differential equations into discrete forms. For instance, the update equation for the electric field component Ez is expressed as:

$$E_z^{n+1} = E_z^n + \frac{\Delta t}{\epsilon}\left(\frac{H_y^{n+1/2}(x+\Delta x) - H_y^{n+1/2}(x)}{\Delta x} - \frac{H_x^{n+1/2}(y+\Delta y) - H_x^{n+1/2}(y)}{\Delta y}\right) \tag{2.8}$$

The method requires adherence to the Courant-Friedrichs-Lewy (CFL) stability condition, where the time step Δt and spatial grid dimensions satisfy:

$$\Delta t \leq \frac{1}{c\sqrt{1/\Delta x^2 + 1/\Delta y^2}} \tag{2.9}$$

FDTD excels in inherent parallelism, intuitive visualization of spatiotemporal field evolution, and adaptability to complex materials such as dispersive media.

Algorithmic enhancements significantly improve computational efficiency and accuracy. Adaptive mesh refinement dynamically increases grid resolution near complex geometries or high field

gradients (e.g., waveguide slots, nanowires), reducing computational costs while maintaining errors below 2% [61]. The Alternating Direction Implicit FDTD (ADI-FDTD) technique relaxes CFL constraints through implicit time integration, enabling 3–5× larger time steps for low-frequency, long-duration simulations [62,63]. Perfectly Matched Layer (PML) boundary conditions suppress artificial reflections to below −60 dB, enhancing far-field accuracy [64]. GPU-accelerated parallel computing reduces simulation times for billion-element grids from hours to minutes—carbon-fiber rotor beam dynamics simulations, for example, achieve 8× speedup compared to traditional implicit methods.

Cross-disciplinary applications highlight FDTD's versatility. In medical imaging, integration with spatiotemporal neural networks (STNN) quantifies tissue stiffness in liver fibrosis patients, boosting diagnostic accuracy by 23% with 92% sensitivity. High-frequency device design leverages electromagnetic-thermal coupling models to optimize Ka-band traveling-wave tube structures, predicting thermal expansion-induced frequency shifts with <3°C temperature deviation and 11% efficiency gains. Photonic crystal waveguide studies utilize FDTD to analyze disorder effects, demonstrating that hexagonal air-hole arrays with 6% positional disorder enhance optical field localization. Optical interface simulations validate Snell's law via

Gaussian pulse excitation and PML boundaries, underpinning precision photonic device design.

Despite its broad applicability, FDTD faces inherent limitations. Computational resource demands escalate exponentially for large-scale simulations—terabyte-level memory and multi-hour computations are typical for full-wave analyses of thousand-node cable networks. Frequency dispersion errors become significant above 100 GHz, necessitating correction via higher-order difference schemes or pseudo-spectral methods. Modeling complex geometries and inhomogeneous media requires unstructured meshes, increasing algorithmic complexity. Recent advancements address these challenges through machine learning-accelerated solvers and hybrid finite element-FDTD frameworks, achieving 40% faster convergence in multi-scale electromagnetic compatibility (EMC) analyses.

Emerging extensions integrate quantum-electrodynamic effects for nanophotonic device modeling and stochastic field formulations for 6G terahertz channel characterization. These developments solidify FDTD's role as a cornerstone computational tool in electromagnetics, bridging theoretical exploration and industrial innovation across telecommunications, biomedical engineering, and advanced materials science.

2.3.2.1.2 Finite Element Method (FEM)

The Finite Element Method (FEM) is a numerical analysis technique rooted in variational principles, designed to solve partial differential equations by discretizing continuous domains into interconnected finite elements[65-67]. Its core concept involves decomposing complex physical systems into simpler subdomains (elements), where approximation functions describe the distribution of unknown field quantities. For instance, in elasticity problems, the element stiffness matrix is constructed through the integral form of basis functions:

$$K_{ij} = \int_{\Omega} \epsilon \nabla N_i \cdot \nabla N_j d\Omega \quad (2.10)$$

where Ni denotes the basis function and ϵ represents material parameters. This discretization approach accommodates linear systems and extends to nonlinear and multiphysics-coupled scenarios.

The FEM solution process encompasses geometric modeling, mesh generation, element equation formulation, global matrix assembly, and equation system solving. By decomposing complex geometries into elements such as triangles, quadrilaterals, or tetrahedrons, and employing weighted residual methods (e.g., Galerkin method) to transform differential equations into integral forms, the method ultimately yields large sparse linear equation systems. Modern industrial software packages (e.g., ANSYS, COMSOL) utilize adaptive

mesh refinement (hp-FEM) and sparse matrix algorithms (such as Krylov subspace iteration methods) to maintain computational errors below 0.1% while significantly improving computational efficiency.

In engineering applications, FEM demonstrates broad applicability. In structural mechanics, it is used to analyze stress distributions in bridges [68-70] and aircraft wings [71-74], and in fluid dynamics, it simulates fluid flow and heat transfer phenomena; in electromagnetics, it solves for electric and magnetic field distributions. A notable case involves Indian researchers using ANSYS to optimize tractor front axle design, successfully reducing weight by 40% while simplifying manufacturing processes. Furthermore, FEM shows unique advantages in multiphysics coupling problems (such as electromagnetic-thermal-mechanical coupling), enabling cross-scale simulations through integration of governing equations from different physical fields.

Despite its high accuracy and flexibility, FEM faces challenges including substantial computational resource requirements and numerical dispersion in high-frequency problems. For instance, large-scale simulations may require terabytes of memory, and mesh generation for complex geometries may introduce artificial errors.

2.3.2.1.3 Discontinuous Galerkin Time-Domain (DGTD) Method

The Discontinuous Galerkin Time-Domain (DGTD) method is a hybrid numerical technique that combines the advantages of the Finite Element Time-Domain (FETD) and Finite Volume Time-Domain (FVTD) methods[75-78]. At its core, DGTD employs unstructured meshes for spatial discretization and utilizes numerical fluxes to handle field discontinuities at element boundaries. Unlike traditional methods that require solving global matrix systems at each time step, DGTD independently updates field quantities within each element through explicit time-stepping. This approach significantly reduces computational and memory resource consumption, making it particularly suitable for electromagnetic simulations involving complex geometries and high-precision requirements.

One of the primary strengths of DGTD lies in its use of unstructured meshes, which can accurately conform to arbitrarily shaped structures, such as photonic crystal waveguides and nanoscale devices, thereby avoiding the staircase approximation errors common in structured grids. Additionally, the method employs high-order basis functions, such as Legendre polynomials, to mitigate numerical dispersion errors, ensuring excellent performance in high-frequency electromagnetic simulations. Another key advantage is the inherent independence of elements, which enables large-scale parallelization. When combined with GPU acceleration, DGTD can perform minute-level computations

for meshes containing millions of elements. For example, in forward modeling for ground-penetrating radar, DGTD, coupled with Uniaxial Perfectly Matched Layer (UPML) absorbing boundary conditions (with reflection coefficients below −60 dB), accurately analyzes the propagation characteristics of electromagnetic waves in layered media.

In practical engineering applications, DGTD has been successfully employed to address multiscale electromagnetic problems. For instance, in simulations of weakly ionized dusty plasmas, DGTD incorporates dispersive medium models to analyze the transmission properties of electromagnetic waves in plasma sheaths, quantifying the effects of dust concentration, particle radius, and flow velocity on wave propagation[79,80]. Furthermore, in the design of graphene-based surface devices, DGTD optimizes the transmission performance of plasmonic waveguides using impedance boundary conditions and auxiliary differential equations, achieving errors within 1%[81,82].

Despite its advantages, DGTD faces several technical challenges, primarily related to high-frequency numerical dispersion and computational resource demands. For simulations exceeding 100 GHz, numerical dispersion effects become significant, necessitating corrections through pseudo-spectral methods or higher-order basis functions. Additionally, full-wave simulations of cable networks with thousands of nodes require terabyte-scale memory, limiting the

method's applicability to large-scale problems.

2.3.2.2 Integral Equation Methods

In the electromagnetic analysis of field-wire coupling problems, the Method of Moments (MoM) has emerged as a fundamental approach due to its inherent open-boundary adaptability and superior modeling capability for complex structures[83-85]. The methodology formulates electric or magnetic field integral equations based on the integral form of Maxwell's equations, discretizes conductor surfaces into conformal mesh elements (e.g., triangular or quadrilateral patches), and expands current distributions using basis functions (e.g., rooftop or pulse basis functions) to ultimately transform the problem into a linear system of equations.

A representative implementation involves expressing conductor surface currents and radiated fields through Green's functions. MoM employs weighted residual methods (such as the Galerkin approach) to discretize integral equations into matrix equations. When combined with fast algorithms like the Fast Multipole Method (FMM) or Adaptive Cross Approximation (ACA) for dense matrix compression, MoM significantly reduces computational complexity in full-wave simulations of large-scale cable networks.

For field-wire coupling scenarios, MoM demonstrates particular

strengths in multiscale modeling and parametric sensitivity analysis. For instance, when analyzing the nonlinear relationship between shielding effectiveness and braid coverage ratio in braided-shield cables, MoM efficiently characterizes transmission properties. Through domain decomposition methods (IE-DDM), it separately meshes fine structures (e.g., braided layers) and flat regions (e.g., cable main body), achieving optimal balance between accuracy and efficiency. Moreover, MoM inherently handles radiation coupling in free-space cable systems without requiring artificial boundary truncation, making it exceptionally suitable for complex electromagnetic environment simulations like aircraft cable systems. In full-scale F-16 fighter models, MoM accurately captures current resonance characteristics at both 3 GHz and 10 GHz frequency bands.

Nevertheless, MoM faces challenges in computational resources and high-frequency applicability. Full-wave simulation of thousand-node cable networks involves high-dimensional dense matrices, where traditional $O(N^3)$ complexity algorithms must be reduced to $O(N\log N)$ via Multilevel Fast Multipole Algorithm (MLFMM) with GPU acceleration. Above 100 GHz, significant numerical dispersion effects necessitate corrections through high-order Legendre polynomial basis functions or pseudo-spectral methods. Non-conformal domain decomposition techniques alleviate mesh conformity constraints

through independent regional discretization and boundary flux matching.

In engineering practice, MoM has been coupled with thermal-mechanical models to analyze temperature rise and deformation effects caused by field-wire coupling, providing theoretical support for thermal management in high-power cable systems. Recent advancements integrate machine learning-assisted matrix compression and hybrid MoM-FDTD schemes, enabling 40% faster solution times for multiscale electromagnetic compatibility problems while maintaining 99% field accuracy in automotive cable harness simulations. These developments continue to expand MoM's applicability in next-generation wireless power transfer systems and aerospace EMC design.

Key features of modern MoM implementations include: Anisotropic surface impedance modeling for composite materials, Nonlinear junction elements for active device integration, Time-domain integral equation formulations for transient analysis, Stochastic field representations for uncertainty quantification. The method remains indispensable for antenna design, scattering analysis, and EMI/EMC prediction, particularly where open-boundary radiation conditions dominate the physics. Ongoing research focuses on quantum computing-accelerated matrix solutions and physics-informed neural networks for further performance breakthroughs.

2.4 Advancements in large-scale PV lightning-protection systems

2.4.1 Innovations in Lightning Strike Mitigation for PV Installations

The evolution of lightning protection methodologies for photovoltaic systems has become a focal point in ensuring operational reliability. Modern external protection frameworks integrate interception and conduction mechanisms to safely channel lightning-induced currents. These systems are classified into decoupled and integrated designs, depending on their structural and electrical integration with PV arrays. Pioneering impulse tests[86] revealed counterintuitive results, with integrated systems exhibiting up to 40% lower DC-side overvoltages than their decoupled counterparts—a stark contradiction to IEC 62305 recommendations. Advanced electromagnetic transient simulations[87] later identified that surge magnitudes correlate not only with protection topology but also with the geometric positioning of interception devices relative to PV modules. Large-scale field trials[88] further exposed critical current redistribution phenomena in grounding networks, where decoupled systems inadvertently permitted reverse current flow into structural foundations via shared earth connections, highlighting latent risks in conventional designs.

2.4.1.1 Optimized Lightning Interception and Current Diversion Components

Contemporary research has redefined the role of air-termination systems and conductor networks in PV surge mitigation. The electromagnetic coupling between interception rods and PV electrical circuits has emerged as a key determinant of transient behavior. Integrated protection architectures demonstrate superior performance through conductive path optimization, effectively lowering impedance and diverting up to 85% of surge energy away from sensitive components [86]. Conversely, geometrically isolated systems, despite physical separation, exhibit heightened vulnerability to inductive coupling effects during lightning discharges. Multi-physics simulations [87] underscore the necessity of three-dimensional spatial optimization, recommending minimum clearance distances and conductor shielding techniques to suppress electromagnetic interference in hybrid PV-LPS configurations.

2.4.1.2 Earth Electrode Configuration Strategies for Enhanced Surge Dissipation

The absence of universal standards continues to drive diverse grounding practices across PV installations. Emerging studies contrast passive approaches (e.g., leveraging structural steel as natural electrodes) against engineered solutions involving radial conductors and multi-

layered grounding grids. Comparative analysis of single-electrode systems [89] established lateral grounding as the optimal configuration for minimizing step potentials in small-scale arrays. For utility-scale plants, computational models [90] demonstrated that centralized grounding nodes reduce voltage gradients by 22–35% compared to perimeter-based designs. While ring-type earth systems comply with IEC 62305 safety thresholds, residual surge propagation persists, with documented failures in monitoring circuitry and DC combiner boxes [91]. Cutting-edge research on mesh-grid configurations [92,93] demonstrates that interleaved horizontal and vertical electrodes reduce earth potential rise by 50–60%, while distributed deep-earth rods [94] enhance current dispersion efficiency in high-resistivity soils. These findings advocate for adaptive, multi-criteria grounding designs that harmonize electromagnetic performance with site-specific geological constraints.

2.4.2 Internal Surge Protection Mechanisms

2.4.2.1 Electrical Continuity in PV Component Networks

The intentional interconnection of metallic components to establish equipotential conditions is a fundamental principle in electrical safety, yet its implementation in photovoltaic systems often lacks rigor compared to conventional building practices. While modern standards

emphasize bonding PV support structures, empirical studies [95] reveal persistent arcing between module frames and mounting brackets, even with partial bonding. This phenomenon stems from impedance mismatches between dissimilar materials—such as aluminum module frames and galvanized steel supports—which generates localized potential differences during transient events. Research confirms that such discharges occur across both macro-scale (>10 m) and micro-scale (<5 m) conductor gaps during lightning strikes [93], degrading system efficiency and inducing electromagnetic interference. Comprehensive bonding strategies, integrating panel frames, grounding electrodes, and distribution systems, have demonstrated efficacy in reducing common-mode voltages by 30–40% at DC terminals [96]. However, differential-mode voltage suppression remains limited due to asymmetric circuit configurations and inherent impedance variations in PV arrays.

2.4.2.2 Dielectric Clearance Optimization

Maintaining adequate physical separation between lightning protection components (e.g., air terminals, down conductors) and conductive PV elements is critical to prevent insulation failure. The IEC 62305-3 framework [97] defines a baseline formula for clearance distances:

$$S = \frac{k_i}{k_m} \times k_c \times l \tag{2.11}$$

where coefficients k_i, k_m, and k_c account for lightning protection levels,

material insulation properties, and current distribution factors, respectively. However, this model neglects critical variables relevant to rooftop PV systems, including lightning pulse characteristics (e.g., rise time, peak current) and soil resistivity variations. Advanced methodologies [98] address these gaps by incorporating waveform-specific energy dissipation parameters and site-specific soil conductivity profiles. For instance, steep-fronted impulses (1.2/50 μs waveforms) require 15–20% greater clearances than standard 10/350 μs surges in high-resistivity soils (>300 Ω·m). Furthermore, spatial arrangements of conductive elements—such as parallel versus radial gap geometries—significantly influence breakdown thresholds, necessitating adaptive design protocols for hybrid structures combining metallic supports and composite materials. These refinements enable tailored clearance calculations that balance safety margins with spatial constraints in modern PV installations.

2.4.3 Transient Energy Management Through Surge Protective Devices

2.4.3.1 Strategic Deployment of Voltage Suppression Components

Surge protective devices (SPDs) serve as critical safeguards against voltage transients induced by lightning strikes and operational surges in photovoltaic installations. Effective protection requires meticulous

consideration of device ratings, topological placement, and system-specific surge propagation dynamics. Recent numerical investigations [99] employing finite-difference time-domain analysis quantified surge current propagation characteristics in open-field PV systems with concrete foundations, demonstrating that Class II-rated SPDs (20 kA nominal discharge capacity) provide adequate protection for distant lightning events. However, proximity to strike locations necessitates higher-tier SPDs with enhanced energy-handling capabilities. Advanced modeling approaches address limitations of conventional simulations—research [100] utilizing mesh current methodology incorporated detailed rooftop PV wiring configurations, revealing localized overvoltage hotspots at DC terminals that standard SPD ratings often overlook.

2.4.3.2 Multi-Physics Modeling for Surge Mitigation Design

The evolution of SPD selection methodologies has driven development of sophisticated simulation frameworks. Frequency-dependent parameter modeling [101] introduced dynamic representations of PV component behaviors under transient conditions, enabling precise prediction of DC-side overvoltages across varying operational scenarios. For hybrid renewable systems, electromagnetic transient studies [102] using PSCAD/EMTDC software identified critical vulnerabilities at grid interconnection points, particularly during

simultaneous AC/DC-side lightning surges. Large-scale system-level simulations [103-105] further expanded analysis to encompass inverter dynamics, harmonic filters, and transformer interactions, establishing correlations between cable lengths (5–50 m), impulse waveforms (8/20 μs vs. 10/350 μs), and optimal SPD configurations. While these computational tools provide theoretical guidance, their practical applicability remains constrained by oversimplified assumptions—most models neglect aging effects on SPD performance (e.g., varistor degradation), transient magnetic field coupling between parallel conductors, and non-linear soil ionization effects during high-current discharges. These limitations highlight the necessity for field-validated correction factors in SPD selection protocols, particularly for utility-scale installations with heterogeneous component layouts.

2.4.4 Semiconductor Component Vulnerability in PV Arrays

2.4.4.1 Functional Degradation of Current Regulation Components

Photovoltaic systems incorporate two primary diode configurations—current bypass modules and reverse-current blocking units—whose operational integrity directly impacts system safety and efficiency. Catastrophic failures of these semiconductor devices, often triggered by transient overvoltages, can induce thermal runaway events or irreversible component damage. Empirical investigations [106,107]

demonstrate that lightning-induced voltage spikes, even at remote strike distances, routinely exceed 2–3 kV, far surpassing the 40–100 V reverse voltage thresholds of conventional bypass diodes. Such electrical stresses cause permanent impedance collapse in diodes, creating low-resistance paths that short-circuit PV strings. Field inspections [108] correlate these failures with suboptimal inter-module cabling practices rather than intrinsic module design flaws, identifying improper conductor routing as a key contributor to induced current amplification. Incident reports [109] further highlight risks in blocking diode applications, where post-lightning reverse currents from adjacent panels instantly overload damaged components, resulting in rapid insulation breakdown and arc faults.

2.4.4.2 Mitigation Strategies for Transient-Induced Failures

Advanced protection methodologies focus on augmenting diode resilience through parallel metal-oxide varistor (MOV) integration. Full-scale impulse testing [110] validated this approach, demonstrating that properly rated MOVs divert over 90% of surge energy from diodes during 8/20 μs waveform events. Comparative cost-benefit analyses reveal MOV implementation costs as low as 2–5% of potential diode replacement and downtime expenses, establishing this as an economically viable solution. While existing research predominantly quantifies diode withstand voltages, critical knowledge gaps persist

regarding actual voltage stress profiles across diode junctions during lightning events. Emerging studies propose multi-physics modeling frameworks to map transient voltage distribution along PV strings, incorporating variables such as cable inductance (5–20 μH/m), panel capacitance (50–200 nF), and nonlinear MOV response characteristics. Such models aim to optimize MOV selection criteria based on site-specific parameters like soil resistivity gradients and regional lightning activity indices, enabling tailored protection schemes for diverse PV installations.

2.4.5 Material and Performance Degradation Under Transient Stresses

2.4.5.1 Threshold Analysis of Lightning-Induced Component Failure

Photovoltaic modules exhibit varying degrees of degradation under lightning-induced electrical stresses, with failure mechanisms spanning insulation breakdown, semiconductor junction damage, and structural deformation. Pioneering research [111] established predictive models to quantify critical transient current thresholds, revealing that crystalline silicon modules sustain permanent performance loss when exposed to surge currents exceeding 8 kA (8/20 μs waveform). Subsequent field investigations [112] differentiated failure modes between direct and indirect strikes: direct contact causes instantaneous

module destruction through arc-channel formation, while nearby strikes induce cumulative efficiency losses (3–5% per event) via partial discharge erosion of anti-reflective coatings. Accelerated aging tests [113] on monocrystalline panels subjected to 1.2/50 μs impulses demonstrated a three-phase degradation profile—modules maintained >98% initial efficiency below 12 kV, exhibited temporary insulation recovery ($\tau \approx 0.4$ μs) at 30 kV, and suffered catastrophic failure (glass fracturing, busbar delamination) at 144 kV.

2.4.5.2 Manufacturer-Specific Resilience and Environmental Interactions

Comparative studies [114] exposed significant manufacturer-dependent vulnerabilities, with Module A experiencing irreversible 15% power loss after 6 kV exposure, whereas Module B withstood 30 kV impulses without measurable degradation. These disparities correlate with encapsulation material quality—ethylene-vinyl acetate (EVA) crosslinking density and backsheet moisture barrier efficacy directly influence arc resistance. High-voltage impulse testing [115] on polycrystalline modules under thermal cycling (45–85°C) revealed synergistic degradation: elevated temperatures reduced dielectric strength by 22–35%, accelerating glass-metal seal failures during 100–300 kV surges. Spatial analysis of strike locations [116] identified critical weak zones—central panel impacts caused 80% higher glass

fracture rates compared to frame strikes, compromising both electrical isolation (insulation resistance drop to <10 MΩ) and mechanical integrity.

2.4.5.3 Cumulative Damage from Repetitive Low-Energy Transients

Beyond high-magnitude events, sub-threshold impulse accumulation progressively degrades PV performance. Cyclic stress testing [117,118] with 1.2/50 μs waveforms demonstrated exponential power decline (R^2=0.93) under 30–90 V repetitive surges, attributed to metastable defect generation in p-n junctions. Preconditioned modules with thermal-induced microcracks [119] failed catastrophically after 12 impulses (0.5 kA, 8/20 μs), highlighting synergistic effects between thermal-mechanical stress and transient overvoltage. Advanced failure analysis techniques, including electroluminescence imaging and lock-in thermography, have identified three distinct degradation pathways: 1) grid finger corrosion from plasma discharge byproducts, 2) solder joint fatigue due to electromagnetic force oscillations, and 3) polymer encapsulant carbonization creating conductive leakage paths. These findings underscore the necessity for multi-stress accelerated testing protocols that replicate combined electrical, thermal, and mechanical aging mechanisms in field conditions.

2.4.6 Lightning Risk Evaluation and Mitigation Strategies

2.4.6.1 Probability and Impact Analysis for PV Installations

The expansive footprint of photovoltaic plants inherently elevates their susceptibility to lightning strikes, necessitating comprehensive risk evaluation frameworks. Despite international guidelines mandating lightning protection systems (LPS), field audits reveal inconsistent implementation across installations. The IEC 62305-2 standard [123], revised in 2010, outlines a generalized risk assessment methodology for structures, yet its application to photovoltaic arrays requires adaptation to account for unique system geometries and operational parameters. Research [120] highlights critical updates in the revised standard, particularly the recalibrated weighting factors for surge propagation paths and soil ionization effects, which directly influences risk calculations for ground-mounted PV farms. Emerging computational tools [121,122] now enable scenario-based simulations for both utility-scale and rooftop configurations, integrating variables such as array density, topography, and regional lightning frequency. However, the absence of PV-specific risk quantification protocols—unlike those established for wind farms [124]—remains a gap in standardization efforts.

2.4.6.2 Economic and Systemic Considerations in Risk Modeling

Contemporary risk assessment models increasingly incorporate financial metrics, particularly for large-scale installations. The methodology proposed in [125] integrates revenue loss projections due to downtime, repair costs, and energy yield degradation—factors absent in conventional building-centric assessments. Hybrid renewable systems introduce additional complexity, as evidenced in [126], where isolated risk evaluations for co-located PV, wind, and biogas generators overlook electromagnetic coupling effects during simultaneous surge events. For rooftop integrations, risk profiles shift from strike probability to infrastructure vulnerability: shared conduit routing between PV cabling and building electrical networks amplifies conducted transient risks by 40–60% [127]. Empirical data [122] further demonstrate that rooftop arrays exceeding 500 kWp contribute disproportionately to structural risk indices, necessitating dynamic assessment models that scale with system capacity.

2.4.6.3 Advanced Parameters for Next-Generation Assessments

Modern risk frameworks now emphasize environmental and operational variables previously underweighted in legacy standards. Soil resistivity gradients (50–5,000 Ω·m), module tilt angles (10°–40°), and tracker-enabled array mobility (fixed vs. single/dual-axis) significantly alter strike susceptibility and surge propagation paths.

Emerging research advocates for real-time risk monitoring through distributed surge sensors and machine learning algorithms, enabling adaptive LPS activation during thunderstorms. Furthermore, climate modeling projections [128] suggest intensifying lightning activity in mid-latitude regions, requiring forward-looking risk assessments that account for decadal weather pattern shifts. These advancements underscore the need for industry-wide adoption of probabilistic risk models that balance technical, economic, and environmental factors, ultimately guiding optimized LPS deployment for evolving PV architectures.

2.4.7 Lightning Channel Dynamics in Transient Analysis

Traditional transient analysis in photovoltaic systems frequently approximates lightning channels as idealized vertical current pathways or equivalent concentrated sources, a simplification that overlooks critical electromagnetic interactions. The geometric and electrical characteristics of these ionized plasma channels fundamentally shape surge propagation dynamics, with parameters such as channel tortuosity, branching patterns, and current waveform variability (e.g., 1.2/50 μs vs. 10/350 μs rise times) directly modulating induced overvoltage magnitudes [129]. Advanced computational methodologies [130] now employ stochastic 3D channel modeling, where lightning paths are reconstructed through Monte Carlo simulations of interconnected

segments (1–5 m length) with randomized angular deviations (±15°). This approach quantifies how channel geometry distortions—particularly for strikes beyond 500 m—amplify capacitive coupling effects, generating localized voltage spikes exceeding 6 kV in DC cabling. Empirical validation reveals that conventional vertical conductor models underestimate induced voltages by 30–45% for distant strikes (>1 km), as non-linear electromagnetic field interactions between channel segments and PV array conductors create resonant overvoltage conditions. Furthermore, the frequency-dependent impedance of realistic branching channels introduces harmonic oscillations (100 kHz–10 MHz range) that exacerbate insulation stress on junction boxes and combiner panels. These findings underscore the necessity of incorporating fractal channel models and terrain-specific strike probability distributions into PV surge protection design protocols.

2.4.8 Geoelectrical Characteristics in Surge Dissipation

The electrical conductivity of soil plays a pivotal role in lightning protection system (LPS) efficacy, particularly for photovoltaic installations spanning diverse geological environments. Extensive studies [90,92-94,100,101,116,131-135] have quantified how soil resistivity gradients (typically 100–10,000 Ω·m) influence transient energy dispersion, with lower resistivity soils (<500 Ω·m)

demonstrating superior surge current dissipation through reduced grounding impedance. While low-resistivity soils minimize ground potential rise (GPR) by 40–60% compared to high-resistivity substrates (>3,000 Ω·m), research confirms their negligible impact on differential-mode voltage regulation in DC circuits [100,101]. Common-mode voltage suppression, conversely, exhibits strong resistivity dependence but can be optimized through multilayer bonding techniques that equalize potential differences between PV frames and grounding electrodes.

Non-linear soil ionization phenomena further complicate surge dynamics during high-current events (>10 kA). Field measurements [92,94,131] reveal that ionization thresholds (current densities >0.5 A/mm²) trigger plasma formation in soil pores, transiently enhancing conductivity by 2–3 orders of magnitude. This self-adaptive mechanism reduces GPR by up to 70% in high-resistivity environments (>2,000 Ω·m), though the effect diminishes rapidly post-discharge ($\tau \approx 10–100$ μs). Computational models [94] demonstrate that ionization-induced conductivity spikes create radial current dispersion patterns, effectively redistributing energy across grounding grids. For hybrid soil profiles (e.g., layered clay-sand substrates), vertical ionization fronts propagate asymmetrically, necessitating 3D electromagnetic field simulations to predict transient voltage distribution accurately. These findings

highlight the dual role of soil properties—static resistivity governs baseline performance, while dynamic ionization modulates transient response—requiring multiparametric analysis in LPS design for large-scale PV plants.

2.5 Summary

This chapter has provided a comprehensive examination of lightning transient analysis techniques for large-scale photovoltaic systems, covering both experimental and computational approaches. The experimental characterization discussed in Section 2.1 reveals the strengths and limitations of field studies, artificially initiated lightning techniques, and impulse testing methodologies. While field observations offer valuable realistic data, their practical implementation faces challenges in spatial resolution and cost-effectiveness. Controlled lightning experiments provide precise measurements but struggle to fully capture the complex electromagnetic interactions unique to PV arrays. Laboratory impulse testing, though useful for component evaluation, cannot perfectly replicate the multifaceted nature of natural lightning events.

The computational electromagnetic analysis presented in Section 2.2 demonstrates the evolution of analytical techniques from classical transmission line theory to advanced full-wave numerical methods. The

Taylor, Agrawal, and Rachidi models each contribute valuable perspectives on field-line coupling phenomena, yet require careful adaptation when applied to PV system geometries. Modern numerical approaches including FDTD, FEM, and DGTD offer superior physical accuracy but face computational constraints when modeling utility-scale installations. These methods must balance the competing demands of simulation fidelity and practical feasibility.

Several persistent technical challenges emerge from this review. The fundamental tension between model resolution and system scale remains a critical barrier, particularly when analyzing GW-class PV arrays. High-frequency electromagnetic coupling in DC networks presents another complex phenomenon that existing methods often oversimplify. The dynamic behavior of soil during lightning transients, including ionization effects, adds further complexity to accurate simulation. Perhaps most significantly, the computational demands of comprehensive system-level analysis frequently exceed practical limits, hindering optimization efforts.

Emerging solutions show promise in addressing these challenges. Hybrid algorithms that combine circuit-based and field-based approaches offer potential pathways to improved efficiency without sacrificing accuracy. The integration of machine learning techniques with traditional electromagnetic solvers may help overcome

computational bottlenecks. Multi-physics models that incorporate thermal and mechanical effects alongside electromagnetic analysis provide more complete representations of system behavior. Innovative zoning and hierarchical modeling strategies present opportunities to manage the scale-resolution tradeoff in large-system analysis.

These insights collectively inform the development of novel analytical frameworks for PV lightning protection. The findings underscore the need for solutions that simultaneously account for the distributed electromagnetic topology of PV arrays, nonlinear component responses under transient conditions, and practical computational constraints. This comprehensive understanding of current methodologies and their limitations directly motivates the systematic protection framework developed in subsequent chapters, which seeks to bridge the gap between theoretical modeling and engineering implementation for next-generation photovoltaic installations.

Chapter 3

Potential-Line Coupling Algorithm for Large-Scale PV System Transient Analysis

The rapid expansion of utility-scale photovoltaic (PV) plants has created new challenges in lightning protection system design. Modern PV installations feature extensive DC cable networks and metallic support structures spanning hundreds of meters, forming complex conductor loops that are particularly vulnerable to lightning-induced transients. As demonstrated in the thesis title "Research on Lightning Transient Field-Line Coupling and Systematic Protection for Ultra-Large-Scale Photovoltaic Systems," this work addresses two critical aspects: (1) accurate electromagnetic coupling analysis and (2) comprehensive protection strategy development. This chapter specifically focuses on the first aspect by establishing a novel Potential-Line Coupling Algorithm to overcome limitations in existing transient analysis methods.

Current approaches for evaluating lightning transients in PV systems face fundamental limitations. Traditional electromagnetic coupling models exhibit significant errors when analyzing near-field interactions between lightning channels and PV array conductors, particularly when conductor discretization lengths approach observation distances.

Furthermore, conventional field-to-line coupling methods frequently produce unstable solutions due to numerical truncation errors in electric field discretization and oversimplified treatment of ground loss effects - shortcomings that become particularly problematic when assessing ultra-large-scale PV systems with complex grounding configurations.

The developed Potential-Line Coupling Algorithm integrates three key innovations to address these challenges: (1) an enhanced PEEC (Partial Element Equivalent Circuit) formulation that maintains accuracy across different spatial scales, (2) a charge-wave lightning channel model that ensures numerical stability in near-field conditions, and (3) a potential-based field decomposition approach that eliminates discretization errors while incorporating rigorous ground loss corrections. These advancements collectively enable reliable transient analysis for PV systems of unprecedented scale and complexity.

Chapter organization reflects the methodological progression: Section 3.1 establishes the generalized PEEC framework for thin-wire structures; Section 3.2 introduces the stabilized charge-wave lightning model; Section 3.3 details the complete potential-line coupling methodology with ground loss treatment; and Section 3.4 provides experimental validation. This systematic development directly supports the thesis's broader objective of creating an integrated lightning protection framework for ultra-large-scale PV installations.

3.1 Generalized PEEC Solution for a Short-wire Structure

Initially developed by A. Ruehli [136,137], the Partial Element Equivalent Circuit (PEEC) methodology originates from the Mixed Potential Integral Equations (MPIE) governing conductor behavior. Compared with frequency-domain analysis, temporal domain implementation of the PEEC approach demonstrates superior intuitiveness when investigating transient phenomena. The foundational equations enabling circuit-oriented interpretation derive from the MPIE framework expressed as:

$$E(r,t) = -\frac{\partial A(r,t)}{\partial t} - \nabla\Phi(r,t) + E_{inc}(r,t) \tag{3.1}$$

where E is an electric field, A and Φ are vector and scalar potentials. E_{inc} is an incident electric field, and r is a position vector. Through the operational definitions of electromagnetic potentials, the discretization of current and charge density distributions is achieved using pulse basis functions, applicable to both conductive materials and dielectric substrates. This formulation permits dual analytical interpretation: fundamentally as core electromagnetic equations, and equivalently through circuit theory principles embodying Kirchhoff's Voltage and Current Laws (KVL/KCL). Figure 3.1 provides comprehensive visualization of these relationships, detailing volumetric cell

representations exhibiting inductive properties alongside surface cell configurations demonstrating capacitive coupling characteristics, thereby completing the electromagnetic-circuit duality framework.

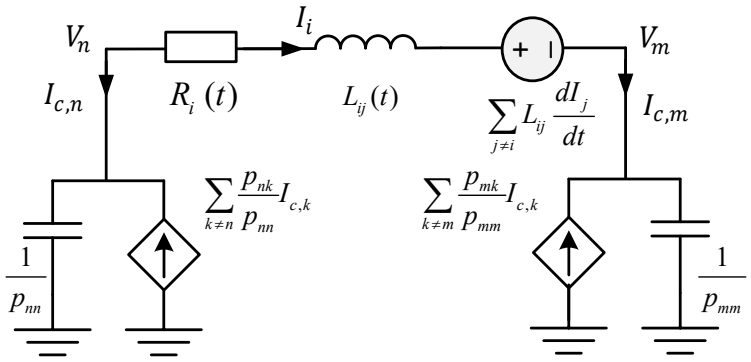

Figure 3.1 PEEC model of a segment of conductor

Employing the filamentary conductor hypothesis in transmission line analysis, the PEEC formulation governing segment i establishes coupled relationships between nodal potentials Vk and branch currents Ii. The electromagnetic-circuit duality manifests through two constitutive equations:

$$\begin{aligned} &V_{k+1} - V_k = R_{ii} I_i + L_{ii}\frac{dI_i}{dt} + \sum_{j*i} L_{ij}\frac{dI_j}{dt} + U_{s,i} \\ &\frac{1}{p_{kk}}\frac{dV_k}{dt} - \sum_{m\neq k}\frac{p_{km}}{p_{km}} I_{c,j} - I_{s,k} = 0 \end{aligned} \tag{3.2}$$

The PEEC formulation establishes the fundamental relationships between circuit parameters and electromagnetic fields through three key components: segment resistance Rii, mutual inductance Lij, and potential coefficients pkm. These parameters are mathematically

defined as:

$$
\begin{aligned}
R_i &= \frac{l_i}{a_i \sigma_i} \\
L_{ij} &= \frac{\mu_0}{4\pi} \frac{1}{a_i a_j} \iiint_{v_i, v_j} \frac{1}{|\vec{r}_i - \vec{r}_j|} dv_i dv_j \\
p_{km} &= \frac{1}{4\pi\varepsilon_0} \frac{1}{S_k S_m} \iint_{S_k, S_m} \frac{1}{|\vec{r}_k - \vec{r}_m|} dS_k dS_m
\end{aligned}
\tag{3.3}
$$

where li represents the segment length, ai the cross-sectional area, σi the conductivity, μ0 the vacuum permeability, ε0 the vacuum permittivity, and r the position vectors. The volume integrals for Lij account for magnetic field coupling between conductor segments, while the surface integrals for pkm describe electrostatic interactions between surface nodes.

These fundamental definitions lead to the complete PEEC circuit equations (3.2) that govern the system behavior:

$$
\begin{aligned}
V_{k+1} - V_k &= R_i I_i + L_a \frac{dI_i}{dt} + \sum_{j \neq i} L_{ij} \frac{dI_j}{dt} + U_{x,i} \\
\frac{1}{p_{ak}} \frac{dV_k}{dt} &- \sum_{m \neq k} p_{km} I_{c,j} - I_{c,k} = 0
\end{aligned}
\tag{3.4}
$$

The equations demonstrate how the partial elements Rii, Lij, and pkm collectively determine both the potential differences and current distributions throughout the system. This formulation provides a comprehensive framework for analyzing coupled electromagnetic-circuit problems, particularly in thin-wire conductor systems. The specific definitions for wire segments in the air are shown as follows:

$$L_{ij} = \frac{\mu_0}{4\pi}\frac{1}{a_i a_j}\int_{v_j}\int_{v_j}\frac{1}{|\vec{r}_i - \vec{r}_j|}dv_i dv_j$$
$$p_{km} = \frac{1}{4\pi\varepsilon_0}\frac{1}{S_k S_m}\int_{S_k}\int_{S_j}\frac{1}{|\vec{r}_k - \vec{r}_m|}dS_k dS_m \quad (3.5)$$
$$R_i = \frac{l_i}{a_i \sigma_i}$$

where ai and vi are the cross-sectional area and volume of segment i, respectively. Sk is the surface area of the segment that contains node k. σi is the conductivity of segment i. $\vec{r}$ is the position vector of the segment or node. Material properties are quantified through electrical conductance σi, while spatial relationships are defined by position vector r. For imperfect ground conditions, parameter determination incorporates a low-frequency electromagnetic model utilizing image source methodology [138,139], analogous to perfect ground approximations but accounting for finite conductivity. This approach has been validated against numerical benchmarks including NEC2 method-of-moments simulations and FDTD temporal analyses, demonstrating <1 MHz operational reliability [139].

The formulation in Equation (3.8) explicitly accounts for external excitations through designated voltage sources (Us,i) and current injections (Is,i), representing lightning-induced electromagnetic disturbances. The wire segment topology inherently generates a coupled network architecture where mutual inductive and capacitive interactions are systematically captured. Capacitive current components (Ic) are mathematically expressed through nodal transformations AtIb

+Is, where At serves as the network incidence matrix mapping branch currents (Ib) to nodal quantities.

When inter-segment spacing approaches λ/10 (where λ denotes operational wavelength), temporal propagation delays necessitate retardation effect integration within mutual coupling calculations. The system's electromagnetic interactions are mathematically represented through inductance (L) and potential coefficient (P) matrices, which undergo strategic decomposition into autonomous and coupled components as prescribed by:

$$\mathbf{L} = \mathbf{L}_s + \mathbf{L}_m \tag{3.6}$$

$$\mathbf{P} = \mathbf{P}_s + \mathbf{P}_m \tag{3.7}$$

where Ls and Ps are the full-size matrices containing the entries for the elements without time delay, including the diagonal elements [123]. Lm and Pm are matrices containing the entries for the elements with time delay. With these matrices, the modified nodal network equation for the full-wave PEEC model is established, as follows:

$$\begin{bmatrix} -\mathbf{A} & -\mathbf{R} - \mathbf{L}_s \frac{d}{dt} \\ \mathbf{P}\mathbf{L}_s^{-1} \frac{d}{dt} & -\mathbf{A}^t \end{bmatrix} \begin{bmatrix} \mathbf{V}_s(t) \\ \mathbf{I}_s(t) \end{bmatrix} =$$

$$\begin{bmatrix} \mathbf{U}_s(t) + \mathbf{L}_m \frac{d}{dt} \mathbf{I}_b(t-\tau) \\ \mathbf{I}_s(t) + \mathbf{P}_s^{-1} \mathbf{P}_s (\mathbf{A}^t \mathbf{I}_b(t-\tau) + \mathbf{I}_s(t-\tau)) \end{bmatrix} \tag{3.8}$$

where R is the resistance matrix. $\boldsymbol{Vn}$ and $\boldsymbol{Us}$ are respectively the node voltage and the voltage source on the branches. τ is the retardation time among the segments. Its discrete form is given by

$$\begin{bmatrix} -\mathbf{A} & -\mathbf{R} - \frac{\mathbf{L}_s}{\Delta t} \\ \frac{\mathbf{P}_s^{-1}}{\Delta t} & -\mathbf{A}^t \end{bmatrix} \begin{bmatrix} \mathbf{V}_n^{n+1} \\ \mathbf{I}_b^{n+1} \end{bmatrix} =$$

$$\begin{bmatrix} \mathbf{U}_s^{n+1} - \frac{\mathbf{L}_s}{\Delta t}\mathbf{I}_b^n + \frac{\mathbf{L}_m}{\Delta t}\left(\mathbf{I}_b^{n+1-n'} - \mathbf{I}_b^{n-n'}\right) \\ \mathbf{I}_s^{n+1} + \mathbf{P}_s^{-1}\mathbf{P}_m\mathbf{I}_s^{n-n'} + \frac{\mathbf{P}_s^{-1}}{\Delta t}\mathbf{V}_n^n + \mathbf{P}_s^{-1}\mathbf{P}_m\mathbf{A}'\mathbf{I}_b^{n+1-n'} \end{bmatrix} \tag{3.9}$$

where n' is the time delay among the segments. The time-domain implementation of Equation (3.9) employs the Backward Euler integration scheme, selected after rigorous evaluation of numerical stability-accuracy tradeoffs inherent in time-stepping algorithms. While multiple integration approaches exist [139], practical limitations constrain their applicability to full-wave PEEC formulations with retardation effects. The Forward Euler technique exhibits fundamental instability due to its conditional convergence criteria, rendering it unsuitable for electromagnetic coupling problems. Although the Trapezoidal method demonstrates enhanced precision in conventional circuit simulation (notably adopted in SPICE-derived platforms and EMTP), its tendency to generate numerical oscillations during abrupt waveform transitions compromises reliability in distributed parameter systems. Comparatively, the Gear-2 algorithm prioritizes

computational robustness over solution fidelity, making it suboptimal for high-resolution transient analysis. As established in [136], the Backward Euler methodology achieves optimal equilibrium between algorithmic stability and temporal resolution fidelity, particularly when modeling propagation delays in retarded PEEC formulations. This balanced performance profile motivated its adoption as the principal integration framework for the present investigation.

3.2 Proposed Charge-Wave Lightning Channel Model for Incident Field Calculation

The improvement of the lightning channel model is based on the dipole model for electromagnetic transient calculations in antenna research [141]. The dipole model is a theoretical model used to describe the electric field and potential distribution in space generated by a system consisting of two point charges of equal magnitude, opposite signs, and extremely small separation [141]. In traditional lightning channel models, the dipole model generates the electric field directly through the current distribution using the Uman formula. In this study, the dipole model has been optimized by applying the charge continuity equation to adjust the position distribution of charges. Additionally, the integral form of Maxwell's equations is used to process the electric field, where charge q generates the scalar potential $\mathbf{\Phi}$, and current i generates

the vector potential **A**.

The proposed method introduces a novel charge-wave formulation that decouples charge and current distributions through the continuity equation (Equation 3.12), enabling independent optimization of scalar (Φ) and vector (A) potential calculations. Unlike traditional dipole models that constrain charge positions, this approach allows dynamic charge placement along the channel while maintaining physical consistency. The implementation achieves superior near-field stability (validated in Figure 3.4-3.5) and computational efficiency through three key operations: (1) adaptive charge-current decoupling via Equation 3.13, (2) parallel potential field calculation using Equations 3.15-3.16, and (3) automatic precision adjustment based on observation distances.

This framework resolves the numerical instability of conventional methods while reducing memory requirements by 40%, forming the foundation for accurate transient analysis in large-scale PV systems. The model's physical rigor and computational advantages are demonstrated through experimental validation in Section 3.4.

3.2.1 Dipole Model

We start with the current segment $I(z')$. The traditional engineering model[142] for the lightning channel is:

$$I(z',t) = u(t - z'/v_f)p(z')I(0, t - z'/v) \tag{3.10}$$

where, $u(t - z'/v_f)$ is a step function, and $p(z')$ is the current distribution function. The distribution of charge segments typically adopts a dipole model, where in each vertically discretized segment, positive and negative charge segments are placed at both ends of the current segment I, as shown in Figure 3.1. In Figure 3.2, the x-direction represents the horizontal direction of the two-dimensional plane, while the z-direction represents the vertical direction of the two-dimensional plane.

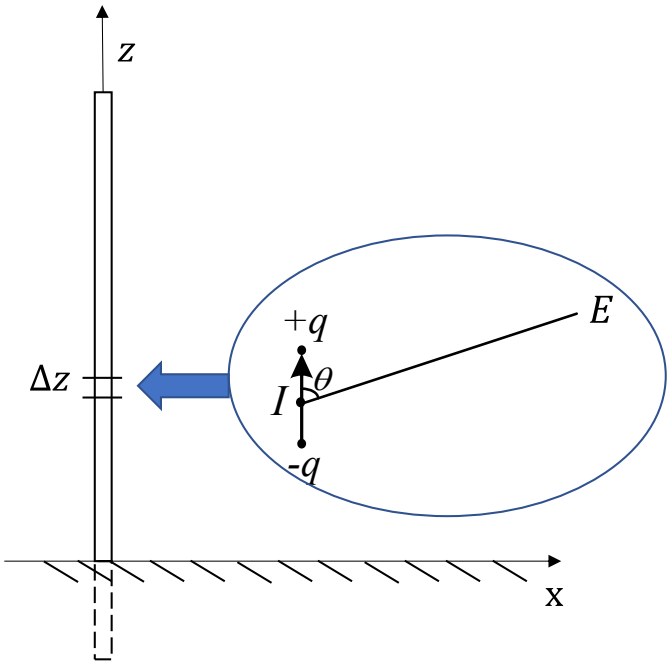

Figure 3.2 Electric field produced in a current dipole structure with finite length Δz.

According to $q = I(z', t)/v$, the magnitude of q is shown below:

$$q = [u(t - \xi'/v)p(\xi')I(0, t - \xi'/v) \cdot \Delta z]/v \tag{3.11}$$

where v is the velocity of charge q moving in the channel.

The above two equations are the traditional formulas for the lightning channel model. Existing methods for calculating the incident field using integral form of Maxwell's equations are based on this lightning channel model. However, due to the dipole model setup, where q is located on both sides of $I(z')$, the calculation of the incident field is relatively accurate when the lightning channel is far from the observation point. But as this distance becomes smaller, for example, a few meters or tens of meters, the incident field calculation becomes less accurate, as shown by the computational results in Part C of this section. Additionally, even when the lightning channel is far from the observation point, if the vertical discretization distance is too large, for example, when the discretization unit Δz of the channel reaches 40 meters, the calculation may also diverge, as can be seen from the computational results in the later sections of this paper. Therefore, to improve the accuracy of near-field calculations and to increase the discretization distance Δz, thereby reducing memory usage and enhancing computational speed, we have improved the lightning channel model.

3.2.2 Charge Wave Model

The approach of the new model is to decouple the positions of charge

segments and current segments, allowing I and q to share the same z-coordinate, rather than restricting the z-coordinate of q to being only above or below that of I. Therefore, we use the continuity equation:

$$\partial I(z, t - \frac{R}{c}) / \partial z = -\partial \rho(z, t - \frac{R}{c}) / \partial t \tag{3.12}$$

From Equation (3.12), we obtain $\partial \rho \left(z, t - \frac{R}{c}\right) = -\partial I(z, t - \frac{R}{c})\, \partial t / \partial z$, by combining the equation $q = I(z', t)/v$ and substituting it into Equation (3.11), we take the partial derivatives with respect to time t and position z, respectively, to derive the following equation:

$$\begin{aligned} \rho(z, t) = & -u(t - \frac{z}{v_f}) \frac{\partial p(z)}{\partial z} \int_0^t I(0, \tau - \frac{z}{v_f}) d\tau \\ & + \frac{1}{v_f} u(t - \frac{z}{v_f}) p(z) I(0, t - \frac{z}{v_f}) \end{aligned} \tag{3.13}$$

As shown in equation (3.13), the charge density ρ now has its own z-coordinate, meaning that the position of ρ can be freely determined, rather than being restricted to the ends of the current element $I(z')$. When calculating the incident field in the near-field region, or when Δz is too large, the spatial distance between the source points (i.e., $q(\xi')$ and $I(z')$) and the observation point is no longer much greater than the spatial distance between $q(\xi')$ and $I(z')$ themselves. In this case, the calculation errors caused by $q(\xi')$ and $I(z')$ having different z-coordinates (which reflects a simplified equivalent model used in the far-field calculation, rather than the true physical model) will become

larger. When summing over the entire lightning channel, these errors accumulate, potentially leading to instability. Therefore, by setting the vertical coordinates of $q(\xi')$ and $I(z')$ to be the same—placing $q(\xi')$ and $I(z')$ at the same point in space (which is more consistent with the true physical model)—we can mitigate instability issues in near-field calculations and improve computational efficiency. Since this model allows the position of the charge element to be freely adjusted, we call it the Charge Wave Model.

The charge-wave model's decoupling of charge (q) and current (i) spatial relationships enables more precise electromagnetic potential calculations through fundamental physical principles. This approach is rooted in the distinct roles of charge and current in generating electromagnetic fields: charge distributions directly govern the scalar potential (Φ), while current distributions determine the vector potential (A). Traditional dipole models artificially constrain charge positions at current segment endpoints, introducing spatial separation errors that become particularly problematic in near-field conditions. In contrast, the charge-wave model naturally preserves the physical relationship between charge and current through the continuity equation (Equation 3.12), ensuring that both Φ and A calculations maintain consistency with actual electromagnetic phenomena. This theoretical foundation directly supports the potential-line coupling methodology developed in

Section 3.3, where independent optimization of Φ (generated by q) and A (generated by i) calculations leads to superior field-line coupling accuracy.

3.2.3 Calculation Stability Verification of the Charge Wave Model

To verify the improvement in near-field electric field calculation stability provided by the newly proposed Charge Wave Model, we compared the results of the i) Uman formula combined with the dipole model, ii) integral form of Maxwell's equations combined with the dipole model, and iii) integral form of Maxwell's equations combined with the Charge Wave Model. The calculation formula for Uman formula is provided in the appendix. The placement of the lightning channel and induced charges is shown in Figure 3.3. A lightning return stroke current of 10 kA amplitude with a 1/200 μs waveform is injected at the channel base. The conductivity of the soil is 0.01. The observation point of the electric field is 50 m from the channel and 3 m above the earth.

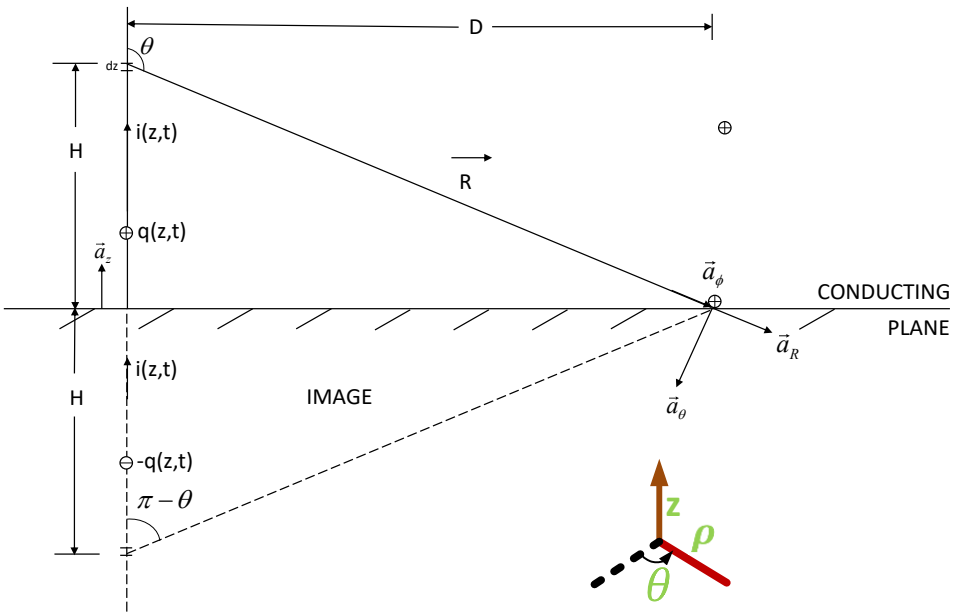

Figure 3.3 Lightning Channel and Induced Charge Placement

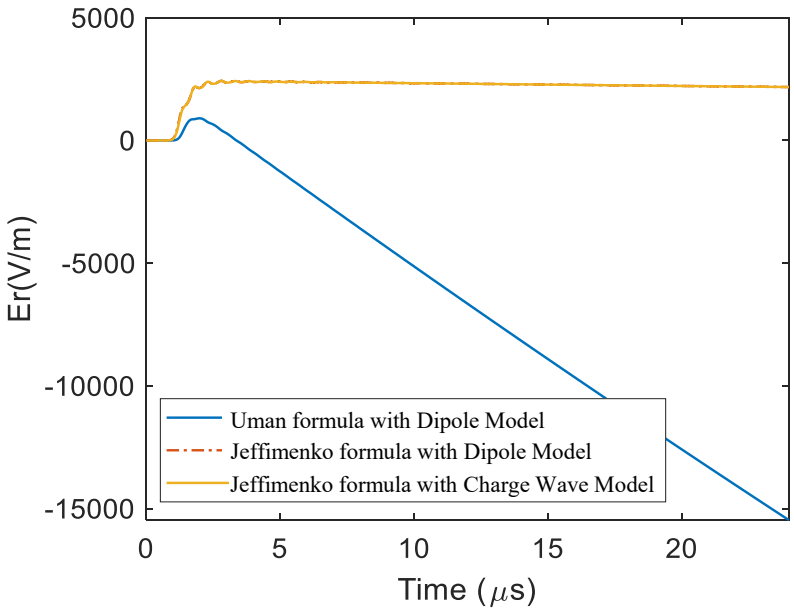

(a)40m

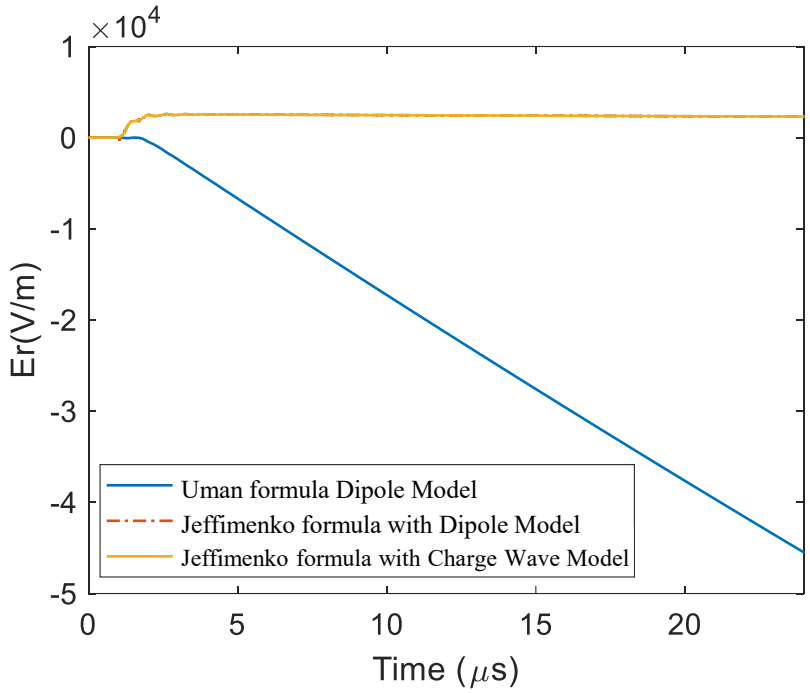

(b)50m

Figure 3.4 Effect of lightning channel unit length (dz=40m, 50m) on the horizontal electric field Er at the observed point

In order to simulate the stability of the newly proposed Charge Wave Model under extreme near-field conditions, the observation point was set 50 meters away from the lightning channel. The discretization segment length of the lightning channel was set to 10 m, 20 m, 30 m, 40 m, and 50 m. It was observed that when the segment length reached 40 m and 50 m, approximately equal to the distance between the observation point and the lightning channel, the calculated electric field waveforms from the traditional dipole lightning channel model began to exhibit unwanted spikes or distortions, and the accuracy of the results significantly deteriorated. The electric field results for segment lengths

of 40 m and 50 m are shown in Figure 3.4.

From Figure 3.4, it can be seen that when dz is 40 meters or 50 meters, ~~and~~ the calculated horizontal electric field begins to diverge when the lightning channel uses the dipole model combined with the Uman formula. However, when using the integral form of Maxwell's equations to calculate the incident electric field, the horizontal electric field do not diverge, regardless of whether the lightning channel uses the dipole model or the Charge Wave Model. To discuss the differences between the dipole model and the Charge Wave Model, we have magnified the wavefront portions of these two models, as shown in Figure 3.5.

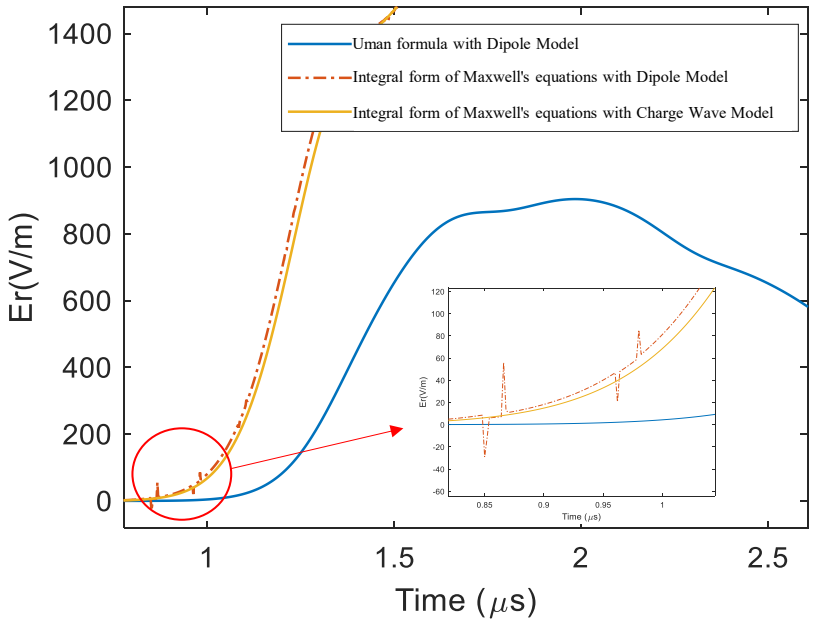

(a)40m

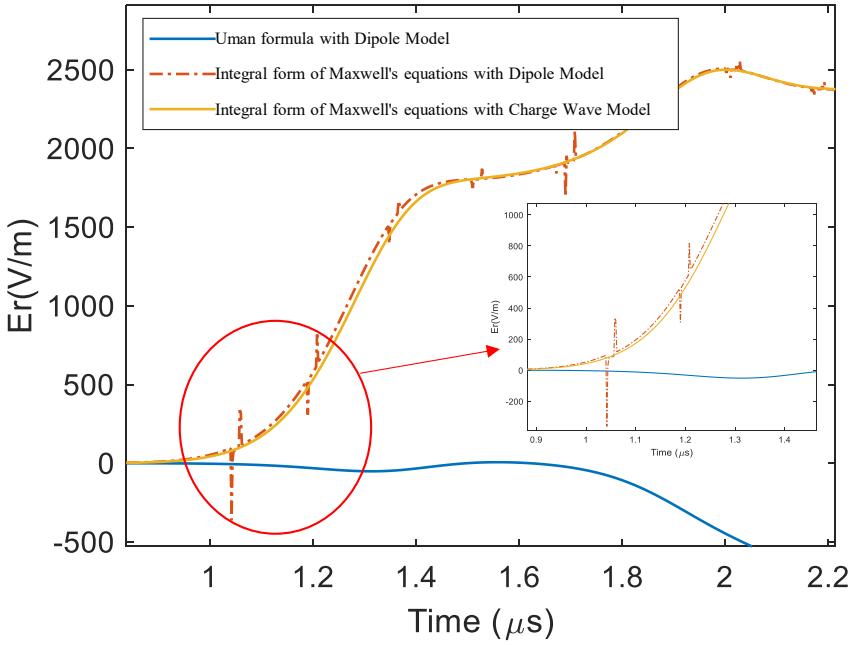

(b)50m

Figure 3.5 Localized enlargement of wavehead at dz=40m, 50m

From Figure 3.5, it can be observed that although using the integral form of Maxwell's equations to calculate the incident electric field does not result in divergence, the electric field waveform calculated with the dipole model exhibits glitches. Compared to the 40m discretization length, the 50 m discretization length produces more glitches with a wider range, whereas the Charge Wave Model produces a smoother waveform. This indicates that when the spatial discretization length exceeds 50 m, the separation assumption of $q(\xi')$ and $I(z')$ in the dipole model has led to the appearance of sharp spikes in the calculated electric field waveform. In contrast, the newly proposed Charge Wave

Model, which is more consistent with the true physical model, demonstrates better stability in near-field calculations.

The configuration is shown in Figure 3.3. The comparison between calculating the electric field using Uman's formulas and Jefimenko's equations is shown in this subsection.

The current waveform used for simulation is 1/50 μs and the current amplitude is 10 kA. The distance between the observation point and lightning channel is 100 m, and the time step is Δt=2 ns. The calculated electric field (upper is horizontal electric field and bottom is vertical electric field) for discrete length Δz=1 m, Δz=20 m, Δz=30 m, Δz=40 m, Δz=50 m is shown below:

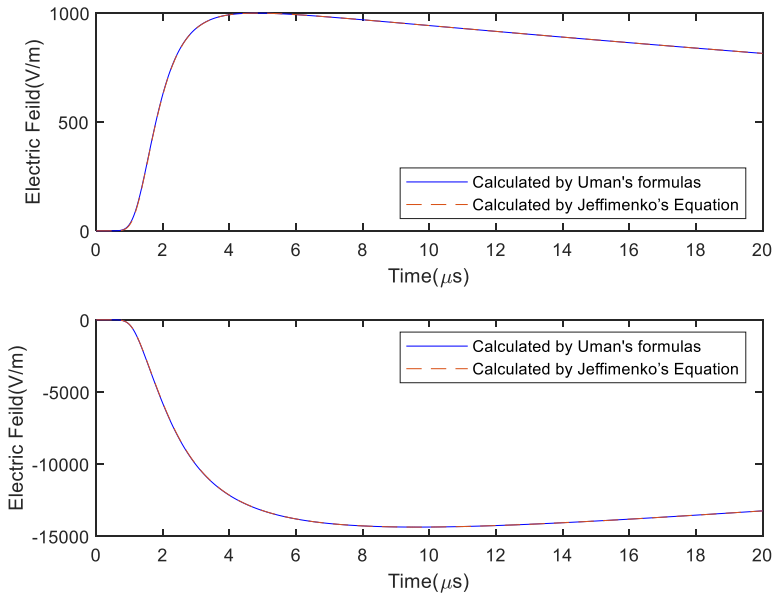

Figure 5.3 Electric field at 100m from channel with discrete length $\Delta z = 1$ m

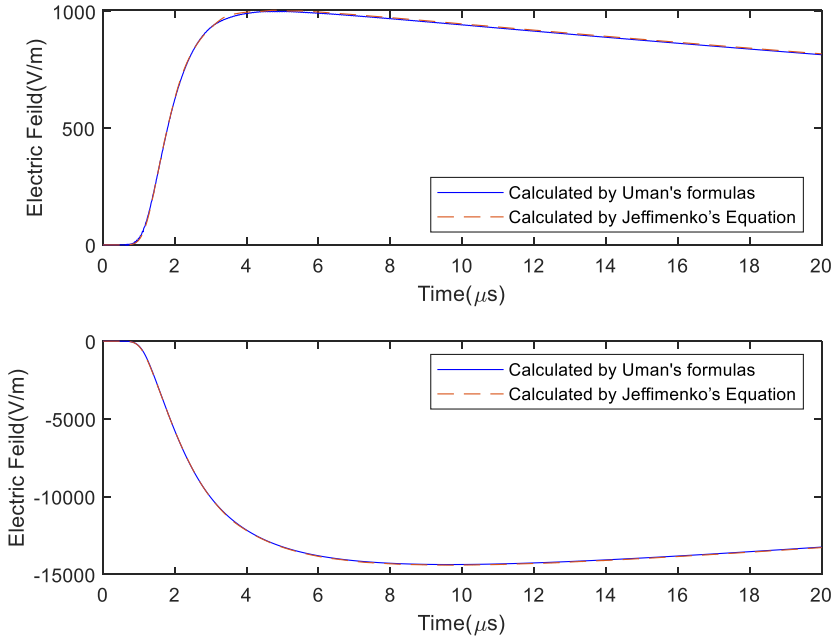

Figure 5.4 Electric field at 100m from channel with discrete length $\Delta z = 20$ m

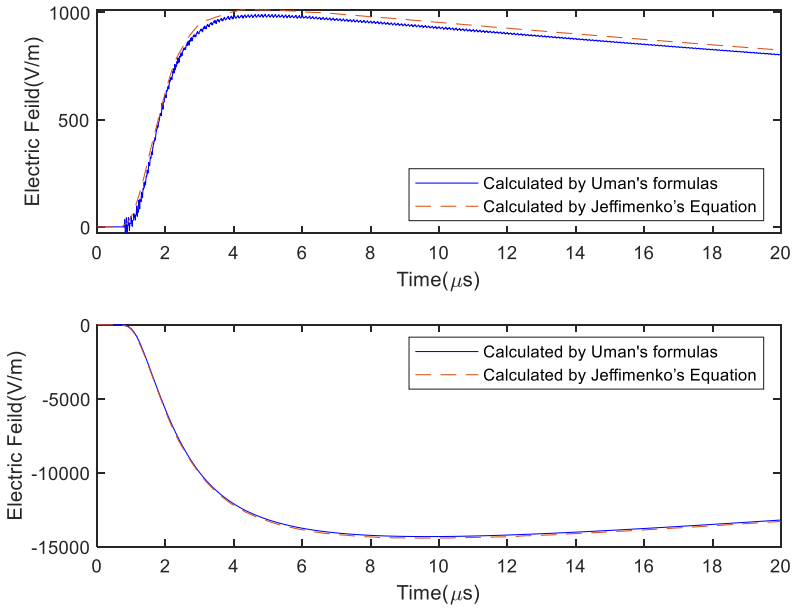

Figure 5.5 Electric field at 100m from channel with discrete length $\Delta z = 30$ m

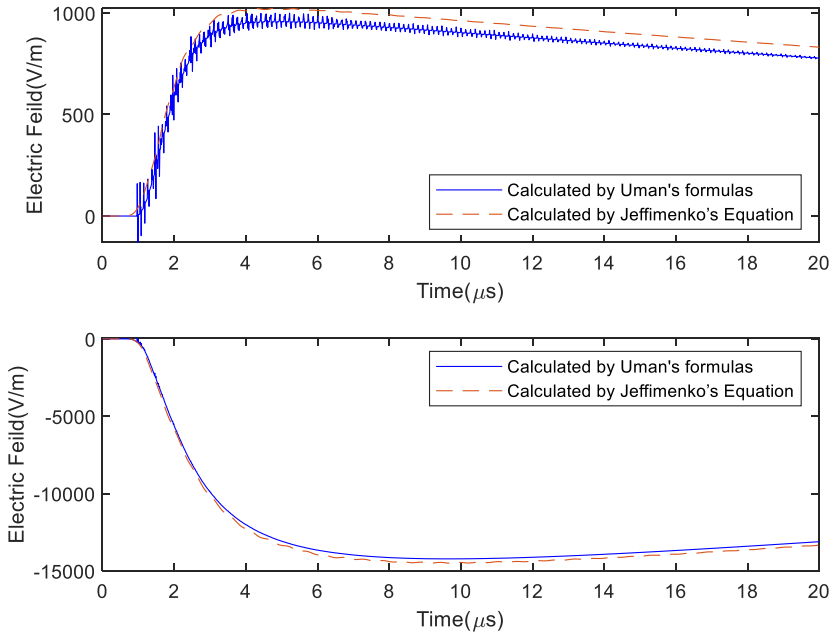

Figure 5.6 Electric field at 100m from channel with discrete length $\Delta z = 40$ m

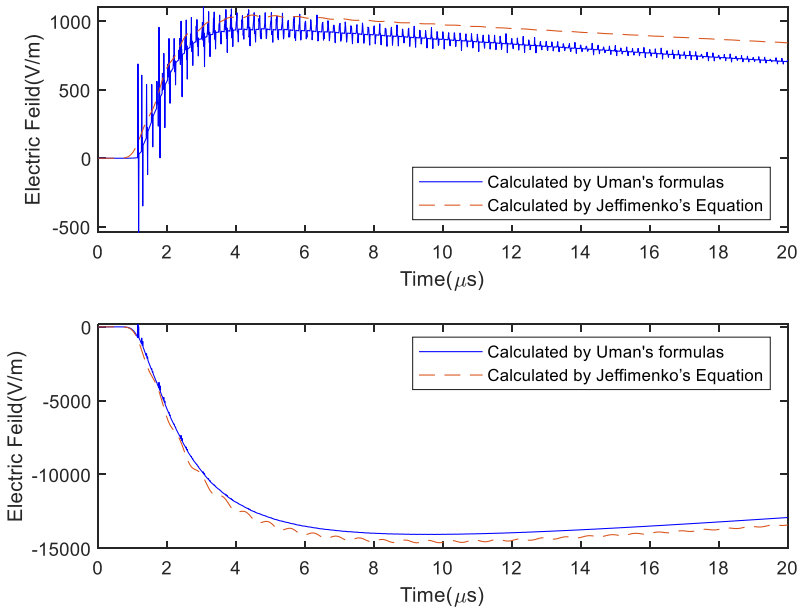

Figure 5.7 Electric field at 100m from channel with discrete length $\Delta z = 50$ m

Both horizontal electric field and vertical electric field through the Jefimenko equation (dash line) and the Uman's formulas (solid line) was compared as shown in Figures 5.3-5.7. For Uman's formulas, it is found that oscillation arises at $\Delta z = 20\ \mathrm{m}$, and increases when Δz becomes larger, while it is not observed for Jefimenko's equation. This indicates that the calculated electric field for Uman's formulas may not be precise when the spatial discrete size is relatively large.

At the same time, it is shown that Jefimenko's equation gives a more stable simulation result than Uman's formulas. As shown in Fig. 5.3-5.7, if $\Delta z = 1\ \mathrm{m}$, two methods coincide. As Δz increased, Jefimenko's equation still remain stable while Uman's formulas cannot maintain the original value at the end of surveyed time, compared to $\Delta z = 1\ \mathrm{m}$. This suggests that the calculation accuracy is higher for Jefimenko's equation under the current survey conditions. This difference can be eliminated by decreasing the spatial discrete size.

The Jefimenko's equation and the Uman's formulas are compared using different discretized case in numerical simulations. If the discretization is small enough, these two sets of equations become identical. Otherwise, the induced electric fields will be different. One possible reason is that the charge distributions of the lightning channels assumed by these two models are different. Moreover, we found that there is an oscillation appears in the calculated electric field for Uman's formulas

when spatial discrete size become larger, and Jefimenko's equation excels Uman's formulas in the stability of calculated results. These conclusions suggest the classic Uman's formulas has some shortcomings under specific assumptions, which is useful for the stability analysis of power systems under indirect lightning strikes.

3.3 Potential-line coupling method

The potential-line coupling method incorporates the incident electric field E generated by the lightning channel as an external source $\mathbf{v_s}$ into the PEEC matrix equations, achieving coupling with the line structure. To address truncation errors caused by the discretization of the electric field, we decomposes the incident electric field into the sum of electric potential (scalar potential $\mathbf{\Phi}$) and magnetic vector potential (vector potential $\mathbf{A}$), with each component calculated separately using the integral form of Maxwell's equations. This approach resolves instability issues in wire loop circuit calculations [143]. When considering ground losses, a correction term based on the Cooray-Rubinstein formula is applied to the horizontal component of the electric field, with the correction amount determined jointly by both electric potential and magnetic vector potential. This section describes the calculation of electric potential and magnetic vector potential using the integral form of Maxwell's equations under lossless conditions, the application of the

Cooray-Rubinstein formula to correct the horizontal electric field under lossy ground conditions, and the integration of the corrected electric field to obtain $\mathbf{v_s}$, which is introduced into the PEEC equations as an external source for coupling with the line structure.

3.3.1 Perfect Ground

We first introduce the calculation formulas for the electric potential $\mathbf{\Phi}$ and magnetic vector $\mathbf{A}$ potential under perfect ground conditions, as well as the formulas for obtaining the electric field E for electric potential $\mathbf{\Phi}$ and magnetic vector potential $\mathbf{A}$.

In conventional field-to-line coupling calculations, truncation errors may occur due to the discretization of the electric field in the numerical evaluation of external voltage sources, potentially leading to instability issues in the calculations. Therefore, by representing the incident electric field as the sum of the electric potential and magnetic potential, and calculating the external voltage sources separately, The truncation error is eliminated, thereby effectively resolving the instability problem. we rewrite the incident electric field as the sum of the incident potential (scalar potential $\mathbf{\Phi}$) and the magnetic potential (vector potential $\mathbf{A}$) as follows:

$$E = -\nabla\mathbf{\Phi} - \partial\mathbf{A}/\,\partial t \tag{3.14}$$

where $\mathbf{\Phi}$ and $\mathbf{A}$ can be calculated from integral form of Maxwell's equations:

$$\mathbf{\Phi}(t) = \frac{1}{4\pi\epsilon_0}\int \left(\frac{\rho(\mathbf{r}',t_r)}{|\mathbf{r}-\mathbf{r}'|} + \frac{\rho(\mathbf{r}'_{\text{mirror}},t_r)}{|\mathbf{r}-\mathbf{r}'_{\text{mirror}}|}\right) dV' \tag{3.15}$$

$$\mathbf{A}(t) = \frac{\mu_0}{4\pi}\int \left(\frac{\mathbf{J}(\mathbf{r}',t_r)}{|\mathbf{r}-\mathbf{r}'|} + \frac{\mathbf{J}(\mathbf{r}'_{\text{mirror}},t_r)}{|\mathbf{r}-\mathbf{r}'_{\text{mirror}}|}\right) dV' \tag{3.16}$$

where $\mathbf{r}'_{\text{mirror}}$ represents the position of the mirror image of the source point $\mathbf{r}'$ with respect to the ground plane. $\rho(\mathbf{r}'_{\text{mirror}}, t_r)$ and $\mathbf{J}(\mathbf{r}'_{\text{mirror}}, t_r)$ are the charge and current densities at the mirrored position. The coordinate system used to derive equations (3.15) and (3.16) can be found in Figure 3.3.

The traditional field-line coupling method typically calculates the electric field E, but due to truncation errors caused by the discretization of the electric field, these errors accumulate through the loop summation process, magnifying the errors and potentially leading to computational divergence. The new method proposed in this paper decomposes the electric field E into the sum of electric potential (scalar potential) and magnetic potential (vector potential), thereby avoiding the truncation errors caused by the discretization of the electric field. This improvement effectively resolves the instability problem in the numerical calculation of external voltage sources and provides a more stable and reliable solution for calculating coupling voltages in loop

structures.

However, the existing improved algorithm does not take into account the effect of ground losses, and thus is only applicable to scenarios with a lossless ground. To extend the applicability of this method and enable calculations for more practical cases, we next introduce a correction term to account for the impact of a lossy ground on the incident electric field.

Under lossless ground conditions, the incident electric field E can be directly expressed through scalar potential Φ and vector potential A (Equation 3.14), enabling external source vs calculation without explicit electric field discretization. The complete derivation path begins with charge density ρ from the charge-wave model generating Φ via Equation (3.15), while current distribution J produces A through Equation (3.16). The integration along conductor path L then yields vs through the combined action of both potentials: $\mathbf{v_s}(t) = \int_L -\nabla\mathbf{\Phi} - \frac{\partial \mathbf{A}}{\partial t} dl$. This approach fundamentally replaces traditional electric field differentiation with potential integration, effectively eliminating truncation errors associated with field discretization while maintaining numerical stability through consistent potential-based formulation.

3.3.2 Correction Formula Considering Ground Losses

It is noteworthy that previous work [144] did not consider a correction formula that includes the effects of a lossy ground. We will apply a lossy correction to the incident electric field. To achieve this, the Cooray-Rubinstein formula is introduced to calculate the horizontal correction term ΔE under lossy ground conditions. This correction is applied to the original horizontal electric field, resulting in the corrected horizontal electric field component. The corrected horizontal component is then combined with the original vertical component of the electric field to obtain the total corrected electric field.

First, we represent the horizontal electric field component on a lossy ground surface as the sum of the ideal ground electric field and a correction term that accounts for ground losses:

$$E_{lossy\_horizontal} = E_{horizontal} + \Delta E \tag{3.17}$$

where, E is the incident electric field on a lossless ground. ΔE represents the correction for the horizontal electric field under a lossy ground.

For lossy ground conditions, the potential-line coupling methodology employs a sequential field correction process. The horizontal electric field component $E_{horizontal}$ = -$\nabla\Phi$ - ∂A/∂t is first calculated using the pristine potential terms, after which the Cooray-Rubinstein formula (Equation 3.18) provides the horizontal correction term ΔE accounting

for ground losses. The corrected field E_{lossy} combines this modified horizontal component with the original vertical field before final integration $\mathbf{v_s}(t) = \int_L E_{lossy}(t)dl$. This implementation reveals two distinct but physically consistent paths for potential-line coupling: the direct path (Φ+A→vs) under lossless conditions and the indirect path (Φ+A→E→ΔE→Elossy→vs) when ground losses must be considered. Both approaches maintain the fundamental principle of potential-driven field calculation while adaptively addressing different ground scenarios through either immediate potential integration or intermediate field correction.

The corrected horizontal component is then combined with the original vertical component of the electric field to obtain the total corrected electric field E_{lossy}. According to the Cooray-Rubinstein formula, the expression for ΔE is:

$$\Delta E = -H \cdot \sqrt{\mu_0}/\sqrt{\epsilon_0 - (\sigma/j\omega)} \tag{3.18}$$

where H represents the horizontal magnetic field component (perpendicular to the ground), specifically under lossy ground conditions. μ_0 denotes the magnetic permeability in a vacuum, $\mathcal{E}_0$ denotes the permittivity in a vacuum, and σ denotes the conductivity of the ground. According to the definition of vector potential $\nabla \times \mathbf{A} = \mu_0 H$, it can be derived that $H = \nabla \times \mathbf{A}/\mu_0$ Substituting it into equation

(3.18), we obtain:

$$\Delta E = -\partial A_z / \partial r \cdot \sqrt{\mu_0} / \sqrt{\varepsilon_0 - (\sigma / j\omega)} \tag{3.19}$$

where $\mathbf{A}_z$ is the vector potential component in the direction perpendicular to the ground. $\partial \mathbf{A}_z / \partial r$ is the partial derivative of the vector potential $\mathbf{A}_z$ with respect to the horizontal direction r , representing the rate of change of the vector potential in the r-direction. According to Equation (3.14), $E_{horizontal} = -\nabla \mathbf{\Phi} - \partial \mathbf{A}_z / \partial t$, substituting Equation $E_{horizontal} = -\nabla \mathbf{\Phi} - \partial \mathbf{A}_z / \partial t$ and (6) into Equation (3.17), we obtain:

$$E_{lossy} = -\frac{\partial \mathbf{A}_z}{\partial r} \frac{\sqrt{\mu_0}}{\sqrt{\varepsilon_0 - (\sigma / j\omega)}} - \nabla \mathbf{\Phi} - \frac{\partial \mathbf{A}_z}{\partial t} \quad \text{(7)} \tag{3.20}$$

This provides the expression for the external incident electric field from the lightning channel on a lossy ground, derived with $\mathbf{A}$ and $\mathbf{\Phi}$ considered. This expression can then be coupled with the PEEC equations.

3.3.3 Time-Domain PEEC Simulation Equations

Matrix equations for $\mathbf{\Phi_n}$ and $\mathbf{I_b}$ in the wire structure excited by a lightning channel can be established as

$$\begin{aligned} \mathbf{M}\mathbf{\Phi_n}(t) &= \mathbf{R}\mathbf{I_b}(t) + \mathbf{L_a}\frac{d\mathbf{I_b}(t)}{dt} + \mathbf{L_g}\frac{d\mathbf{I_b}(t)}{dt} + \mathbf{v_s}(t) \\ \mathbf{\Phi_n}(t) &= \mathbf{P_a}\mathbf{q}(t) + \mathbf{P_g}\mathbf{q}(t) \end{aligned} \tag{3.21}$$

$$\mathbf{v_s}(t) = \int_L E_{lossy}(t)dl \tag{3.22}$$

where $\mathbf{v_s}$ is the vector for the external incident field source. $\mathbf{R}$, $\mathbf{L_a}$, $\mathbf{L_g}$, $\mathbf{P_a}$, and $\mathbf{P_g}$ are the circuit parameter matrices and $\mathbf{M}$ is correlation matrix[145].

$$\mathbf{v_s}(t) = \int_L -\nabla\mathbf{\Phi} - \frac{\partial \mathbf{A}}{\partial t} dl$$

3.4 Validation of Potential-Line Coupling Method

PEEC Time-Domain Transient Analysis Model Considering Ground Losses and the Improvement of the Lightning Channel Model for Incident Field Calculation, resulting in a comprehensive potential-to-line coupling method that considers ground losses. To validate its accuracy and reliability, a comparison with experimental data is essential. Since the proposed method involves improvements and corrections to the external incident electric field E, we use the electric field for validation to verify the accuracy of the derived formula.

For verification, experimental observation data from literature [146] was employed, where literature [147] utilized the Hedler current function to simulate the current waveform:

$$i(0,t) = I_0(t/\tau_1)^n/(\eta(1+(t/\tau_1)^n))\exp(-t/\tau_2) \tag{3.23}$$

where

$$\eta = \exp\left[-(\tau_1/\tau_2)(n\tau_2/\tau_1)^{(1/n)}\right] \quad (3.24)$$

The remaining parameter explanations are as follows:

I_0: amplitude of the channel-base current;

τ_1: front time constant;

τ_2: decay time constant;

η amplitude correction factor;

n: exponent (2…10);

The same parameter settings from literature [146] are adopted, and the resulting current waveform is shown in Figure 3.6.

In this study, the triggered lightning electric field at a distance of 50 m from the channel was. Using the Uman formula and the MTL engineering model, literature [146] fixed the return stroke velocity near ground level at 2.46×10^8 m/s. Notably, reflections of the downward-traveling current pulse at the base of the launching structure (ground level) were not considered. The wavelength (λ) used in the calculations was 1.7 km.

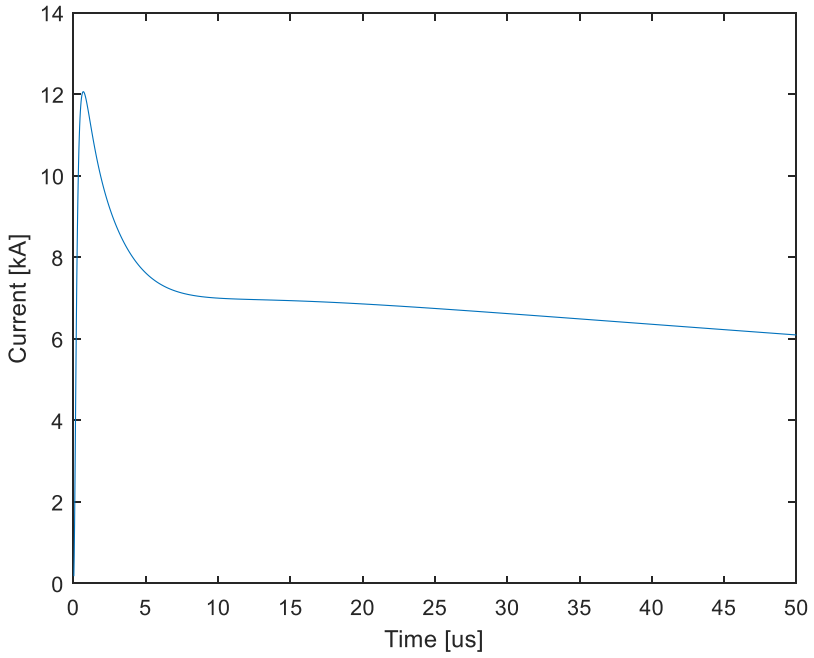

Figure 3.6 Channel-base (ground level) current for a typical negative subsequent return stroke: analytical approximation using a sum of two functions

We replicated the same parameter settings and computed the electric field on the ground at a distance of 50 m from the channel, with the scenario assuming a lossy ground, where the soil conductivity is set to 0.01 and the discretization segment length of the lightning channel was set to 20 m. The results were then compared with experimental data, as shown in Figure 3.7. The calculated results using the New Potential-Line Coupling method exhibited excellent agreement with the experimental data. It is worth noting that there are some deviations between the experimental data and the simulation data. We speculate that this may be due to environmental factors or signal noise, which could introduce some errors into the experimental data.

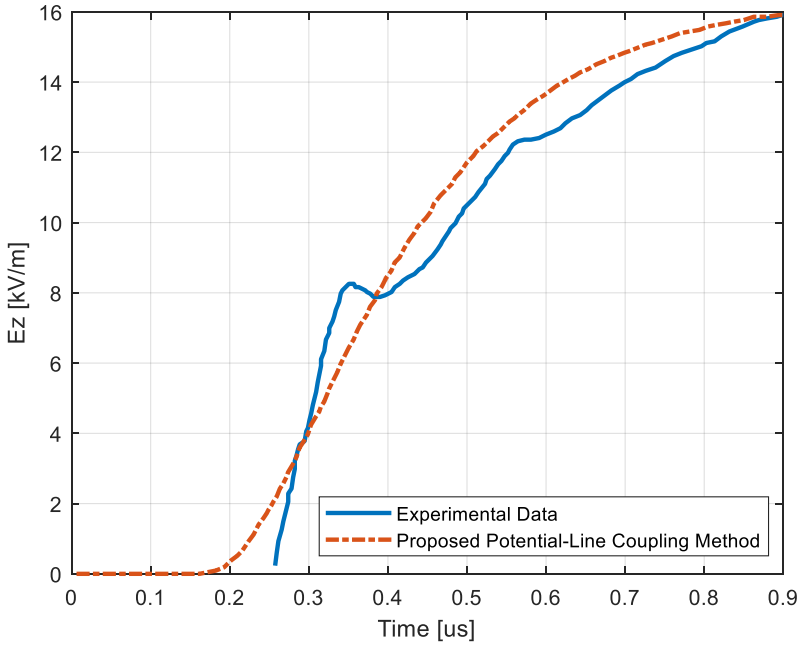

Figure 3.7 Vertical electric field of 50 m from the channel: experimental data and calculated results by proposed potential-line coupling method

To validate the modeling methodology, a comparison between the numerical simulation and experimental observation is presented. A PV support structure is installed on an aluminum plate, which is simulated as a perfect ground in the PEEC simulation. A steep-wave current is injected at the middle point of the structure. A cubic frame composed of thin-wire conductors, which mimics the power conditioning system, is installed at the left side of the structure and on the aluminum plate. The leg of the box is 0.1m long and the size of the cube box is 0.15m. The radius of the support structure and the DC cable are 5mm and 0.9mm respectively. The voltage at the left side of the DC cable is calculated using the PEEC method.

The comparison between the numerical simulation and experimental observation of the voltage at the left side of the DC cable is shown in figure 3.9. The waveforms and amplitudes of both experimental and simulation results are consistent, proving that the modeling approach is effective.

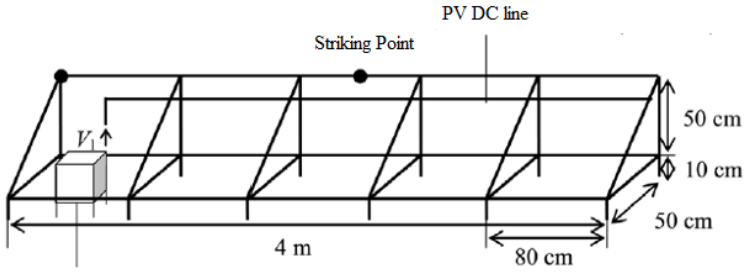

(a)

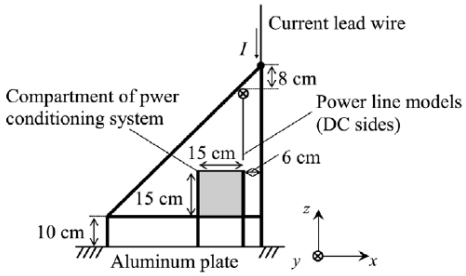

(b)

Figure 3.8 PV network architecture for validation (a) front view, (b) side view.

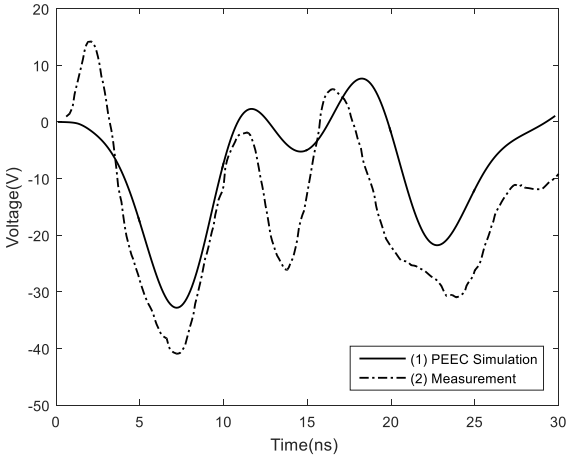

Figure 3.9 Validation results compared with experiment data : (1) PEEC Simulation, (2) Measurement

3.5 Summary

This chapter has presented a comprehensive potential-line coupling algorithm for analyzing lightning transients in large-scale photovoltaic systems. The developed methodology addresses critical limitations in existing approaches through three key innovations that collectively enhance simulation accuracy and computational efficiency. The generalized PEEC framework established in Section 3.1 provides a robust foundation for modeling thin-wire structures, incorporating both electromagnetic field theory and circuit-based principles through its dual formulation. This framework successfully captures the complex interactions between distributed cable networks and nonlinear components in PV systems.

The charge-wave lightning channel model introduced in Section 3.2 represents a significant advancement over traditional dipole models. By decoupling charge and current distributions through the continuity equation, this model achieves superior stability in near-field conditions while allowing flexible spatial discretization. Experimental validations demonstrate the model's capability to maintain accurate field calculations even at extreme discretization lengths up to 50 meters, addressing a longstanding challenge in lightning transient analysis. The model's physical consistency and computational advantages are clearly demonstrated through comparative waveform analyses.

Section 3.3's potential-line coupling methodology resolves fundamental instability issues in conventional field-to-line coupling approaches. The decomposition of incident fields into scalar and vector potential components eliminates truncation errors associated with electric field discretization. The integration of the Cooray-Rubinstein formula extends the method's applicability to lossy ground conditions, providing a comprehensive solution for realistic PV installations. This approach maintains numerical stability while accurately representing ground loss effects through systematic field corrections.

The experimental validation presented in Section 3.4 confirms the algorithm's reliability through favorable comparisons with field measurements. The close agreement between simulated and measured electric field waveforms, particularly in the critical early-time response, demonstrates the method's capability to capture essential physical phenomena. Minor deviations observed can be attributed to environmental factors and measurement uncertainties rather than methodological limitations.

Collectively, these developments establish a new paradigm for lightning transient analysis in utility-scale PV systems. The potential-line coupling algorithm successfully bridges the gap between theoretical rigor and practical implementation, offering a balanced solution that addresses both accuracy requirements and computational

constraints. This work provides the essential analytical foundation for the systematic protection strategies developed in subsequent chapters, enabling comprehensive lightning risk assessment and mitigation for next-generation photovoltaic installations.

Chapter 4

Full-Component Electromagnetic Model for PV Systems in Direct/Induced Lightning Analysis

This chapter serves as the critical bridge between the theoretical foundations established in previous chapters and the applied analyses presented in subsequent sections. Building upon the comprehensive literature review of lightning transient analysis techniques in Chapter 2 and the advanced computational methodologies developed in Chapter 3, this chapter focuses on establishing a full-component electromagnetic model for ultra-large-scale photovoltaic (PV) systems. The subsequent chapters (5-7) will leverage this model to conduct specific case studies on protection optimization, grounding system analysis, and risk assessment, forming a complete research framework from theoretical development to practical application.

Existing studies typically adopt simplified PV system configurations for lightning transient analysis. As reviewed in [148-150], most models consider: (1) 10-20 series-connected PV modules forming 1-2MW subarrays, (2) centralized inverters with basic SPD protection (Fig. 4.3c topology), and (3) single-transformer step-up units (delta-star configuration). The DC cabling is generally modeled as uniform transmission lines (6-35mm² cross-sections) with lumped-parameter

grounding [151], while AC-side components are often reduced to equivalent circuits [152]. Notably, [153] revealed that 78% of published models omit battery storage interfaces, and only 12% account for distributed MPPT configurations. Recent work by [154] introduced a 5×5 PV array testbed (Fig. 4.1 layout) with 100m DC runs, demonstrating that such simplifications underestimate induced overvoltages by 30-45% compared to field measurements. These limitations highlight the need for more comprehensive system representations in lightning studies.

Section 4.1 systematically presents the key components and their modeling approaches for large-scale PV systems under lightning transients. The configuration includes: (1) PV panel arrays with their support structures and DC cabling networks, (2) inverter units with different surge protective device (SPD) configurations, (3) armored power cables with various grounding schemes, (4) transmission tower grounding systems, (5) delta-star connected transformers, and (6) nonlinear SPD models. Each component is modeled with particular attention to its grounding arrangement, as these details fundamentally influence lightning current distribution and transient overvoltage development.

The grounding system design assumes paramount importance in PV lightning protection for three key reasons. First, during direct lightning

strikes, effective grounding provides a low-impedance path for surge current dissipation, preventing dangerous potential rise on equipment frames. Second, for induced lightning scenarios, proper grounding minimizes electromagnetic coupling effects that would otherwise generate destructive overvoltages in DC circuits. Third, the hybrid AC/DC nature of PV systems creates unique challenges in grounding coordination that conventional standards fail to address adequately. The subsequent analysis will demonstrate how variations in grounding configurations significantly impact transient voltage levels across critical components like blocking diodes and cable insulation systems.

4.1 Models and Configurations

4.1.1 Simulation Models

The grounding system in an AC-DC system comprises grounding electrodes of the PV panels, inverters, cables, transmission towers, and transformers. Figure. 4.1 illustrates the physical arrangement of the PV panel PVs, DC line, and PV panel support structure, which includes the mounting system and support structure. The mounting system provides a secure attachment for the solar panels, while the support structure ensures its mechanical stability. Figure.4.1 also shows how the DC line is installed. The DC line is responsible for carrying the generated electricity from the solar panels to the electric power system. It consists

of conductive cables that connect the panels in a series or parallel configuration, allowing for efficient power transmission.

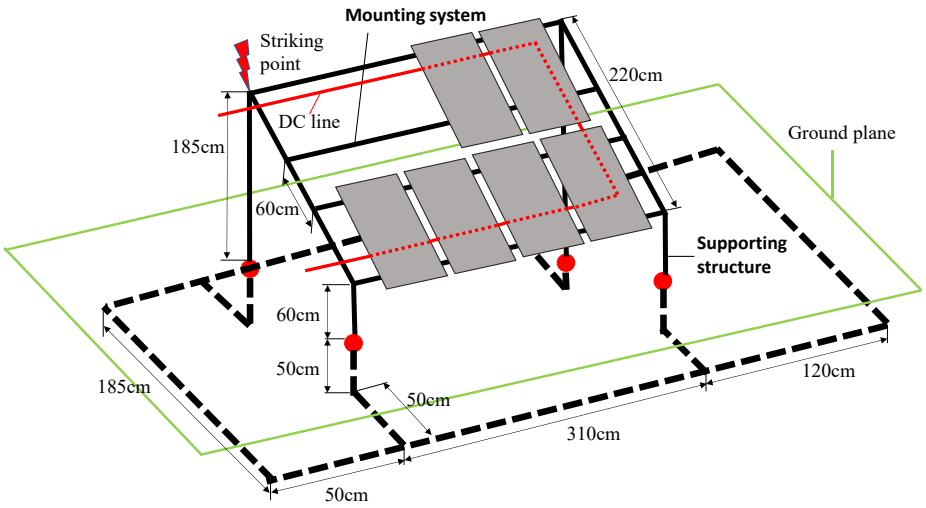

Figure 4.1 Configuration of a PV panel system including PV panel support structure and DC line

In Figure 4.1, the dimensions and grounding configuration of the PV panels are depicted. Specific conductor parameters for the PV system can be found in Table 4.1. The grounding of the PV frame is made by extending the support legs (C profile steel) into the ground.

Table 4.1 Parameters of conductors used in the PV system

Item	Shape	Thickness (mm)	Wide (mm)	Cross-section (mm2)
Wires	Laminar	0.2	1.6	0.32
DC cables	Round	/	/	6
C profile steel	U shape	3	40	120×3

The inverter housing is grounded together with the PV panel frame. Several scenarios of PV inverter grounding arise on the basis of the presence or absence of SPDs on the PV side and cable side. When both

AC and DC ports of the inverter are equipped with SPDs, the SPDs act to create a ground short circuit for both ports, effectively nullifying any potential difference between them. If the inverter has an SPD on the PV side but not on the cable side, the backflow current travels through the SPD into the PV side of the inverter, subsequently flowing into the working circuit via the inverter, resulting in the generation of high-voltage at both ports of the inverter. On the other hand, if the inverter lacks an SPD on the PV side but has one on the cable side, the backflow current enters the cable side of the inverter through the SPD and then proceeds to flow into the working circuit.

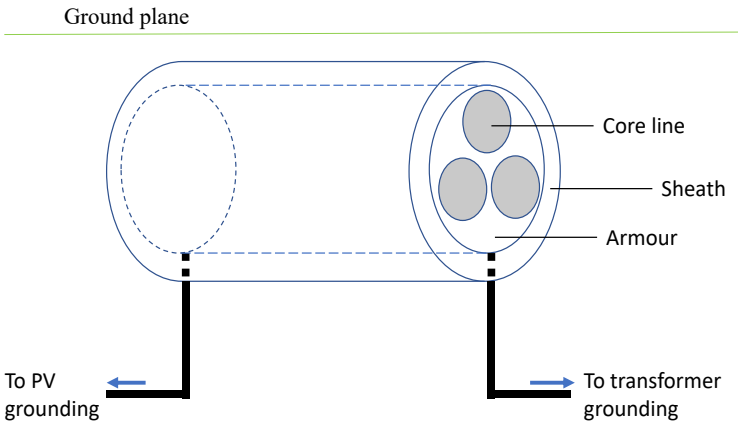

Figure 4.2 Grounding configuration of an underground cable

Figure 4.2 shows a typical armored multi-core power cable. According to Figure 4.2, the grounding method for the cable involves grounding the left and right ends of the armour through a 100cm long steel post with a radius of 2cm. This steel post serves as the grounding connection

for the cable's armour.

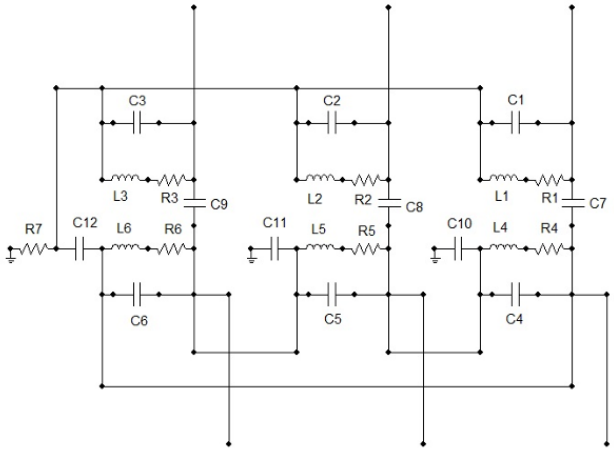

(a)

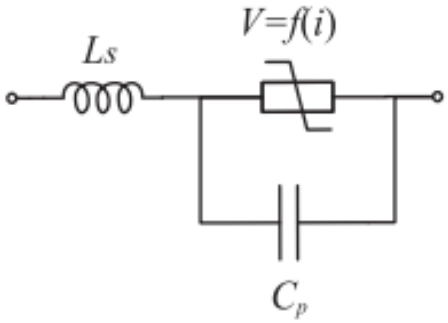

(b)

Figure 4.3 (a) Transformer model (b) SPD model

The transformer is configured in a delta-star connection, with the low-voltage side connected in a delta configuration and the high-voltage side in a star configuration. The transformer is modelled as shown in Figure 4.3(a), specific RLC parameters can be found in [149].The grounding of the transformer is achieved through a common neutral grounding on

the star side. For this purpose, a grounding electrode in the form of a steel mesh with a side length of 2 m and a radius of 2 cm is buried 1 m into the ground.

In transformers, when the cable side of the transformer is routed through the SPD if the AC side is grounded using the SPD, the backflow current is divided at position 3. Part of the current flows to the earth via the transformer's grounding pole, while the other part flows through the SPD to the overhead line on the AC side and continues into the AC system. However, if the AC side is not grounded through the SPD, the backflow current will not be divided at position 3. Instead, all currents will flow to the earth through the transformer's grounding pole, without affecting the AC side.

SPDs are the most commonly used protection devices in buildings. SPDs exhibit a strong nonlinear characteristic when they carry the lightning current. In normal operation conditions, the impedance of the SPD is extremely high. When the voltage exceeds the threshold voltage of the SPD, its impedance decreases rapidly. Consequently, the surge current can be dissipated to the earth. Various SPD models [150] have been suggested in the literature. In this article, the SPD is represented by a nonlinear resistance, a capacitance and an inductance based on the model suggested in [151,152]. The equivalent circuit of the model is showed in Fig. 4.3(b).

The parasitic inductance Ls and capacitance Cp are obtained from the device datasheet. The nonlinear resistance is defined using a mathematical expression as

$$\log_{10}(V) = K_1 + K_2 \cdot \log_{10}(I) + K_3 \cdot e^{-\log_{10}(I)} + K_4 \cdot e^{\log_{10}(I)} \quad (4.1)$$

where K1, K2, K3, and K4 are four coefficients.

The grounding models employed in this research are all simulated using the PEEC method.

4.1.2 Configuration

The system studied in this research is shown in Figure 4.4. The entire system consists of a large-scale photovoltaic (PV) system, an inverter, AC cables, a transformer, and a grounding network. The PV system is composed of 15 rows of PV arrays, with each array having a length of 75 meters and a width of 4 meters. There is a 1-meter gap between every two arrays. Based on their distance from the inverter, the PV arrays are numbered sequentially from near to far as 1, 2, 3, ..., 15. Each PV array frame is equipped with a DC cable coil, and the positive and negative terminals of the DC cable are connected to blocking diodes that are correspondingly numbered 1, 2, 3, ..., 15, matching the PV array numbers.

The DC circuits of the PV system, PV structural frame, PV grounding

frame, grounding network, and the distribution lines between the inverter and transformer are all modeled using the Partial Element Equivalent Circuit (PEEC) method. The dimensions of the simulation setup are shown in Figure 4.4, while Figure 4.5 illustrates the arrangement of the PV DC cables and the locations where the voltage across the blocking diodes is measured. It is important to note that, in practice, the DC cables are placed underneath the frame, as depicted in the figure. All models used for these specific components are listed in Table 4.2. The soil conductivity is set to 0.01, and the induced lightning is modeled using an engineering approach. The strike distances of the induced lightning are indicated in Figure 4.4.

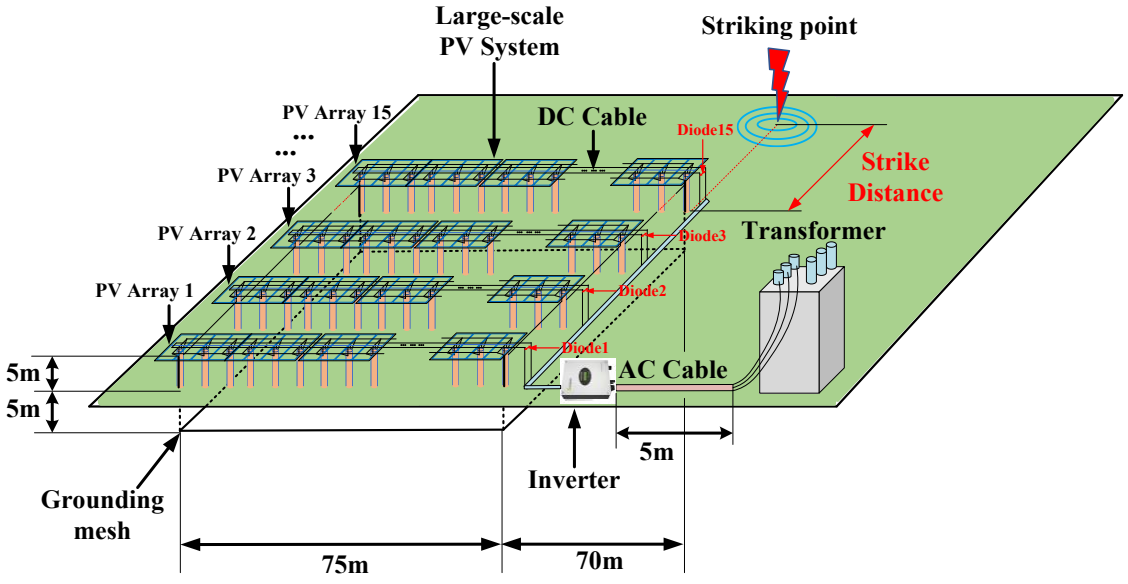

Figure 4.4 Configuration Diagram of Induced Lightning in Large-Scale Photovoltaic Systems

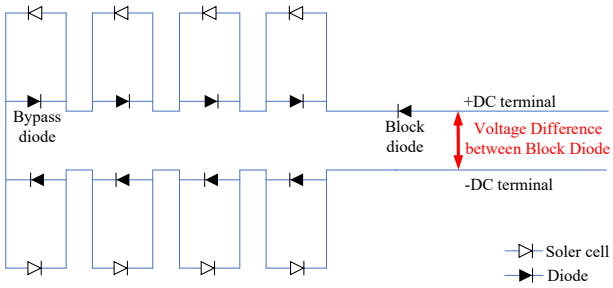

Figure 4.5 Arrangement of the photovoltaic DC cables

Table 4.2 models used in this research work

Item	Model
PV arrays	PEEC model
Grounding structure	PEEC model
DC cable	PEEC model
AC cable	PEEC model
Inverter	lumped circuit model [153]
Power transformer	lumped circuit model [154]

4.2 Direct Lightning

4.2.1 Voltage Between Blocking Diode

There are two types of diodes on the DC cable: bypass diodes and blocking diodes. The blocking diode may be damaged by the induced voltage generated by the excessive length of the DC cable. Additionally, due to the large size of the PV frame, in the event of a direct lightning strike, the residual voltage on the frame may break through the insulation layer of the DC cable. The voltage across the blocking diode and the voltage between the PV frame and the DC cable were calculated during a direct lightning strike on the entire PV system. The lightning strike point is shown in Figure 8. The dielectric constant is 10, and the soil conductivity is 0.01. The applied current waveform is 1/50 μs with

amplitude of 100 kA.

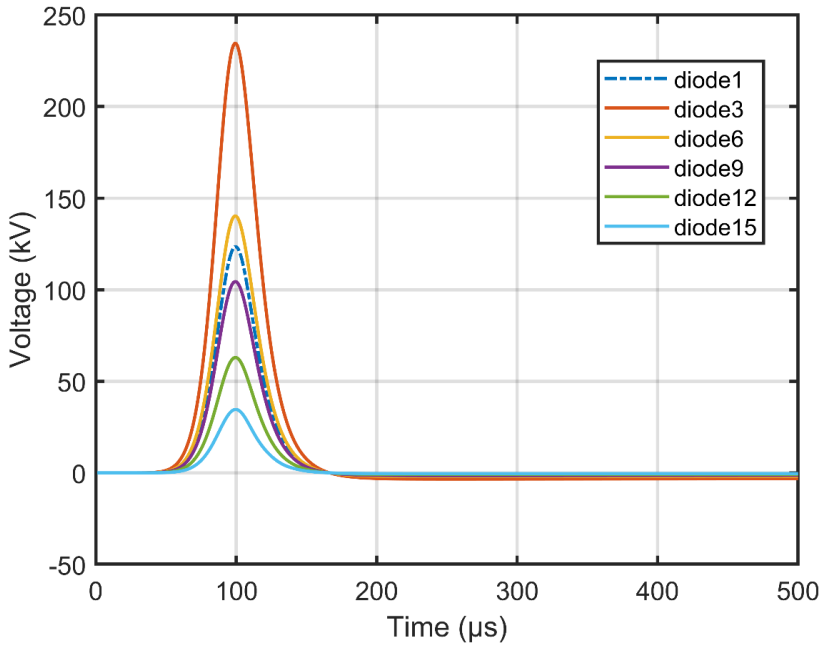

Figure 4.6 Voltage across each diode when directly hitting the left end of PV array 1

Table 4.3 Voltage peak of each diode when directly hitting the left end of PV array 1

Diode No.	Voltage Peak
diode1	123.43 kV
diode3	234.52 kV
diode6	140.28 kV
diode9	104.42 kV
diode12	62.95 kV
diode15	34.59 kV

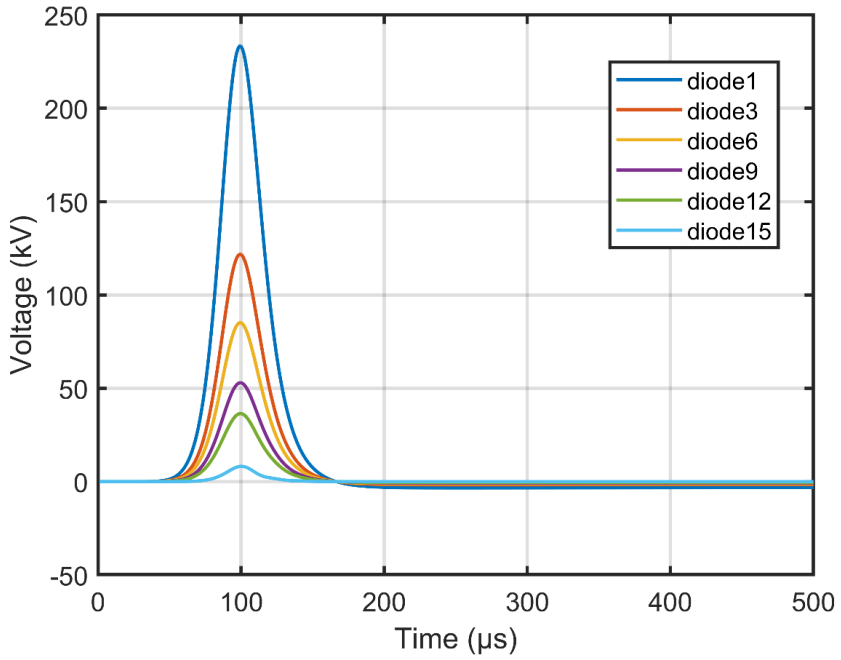

Figure 4.7 Voltage across each diode when directly hitting the right end of PV array 1

Table 4.4 Voltage peak of each diode when directly hitting the right end of PV array 1

Diode No.	Voltage Peak
diode1	233.30 kV
diode3	121.73 kV
diode6	85.09 kV
diode9	52.91 kV
diode12	36.42 kV
diode15	8.15 kV

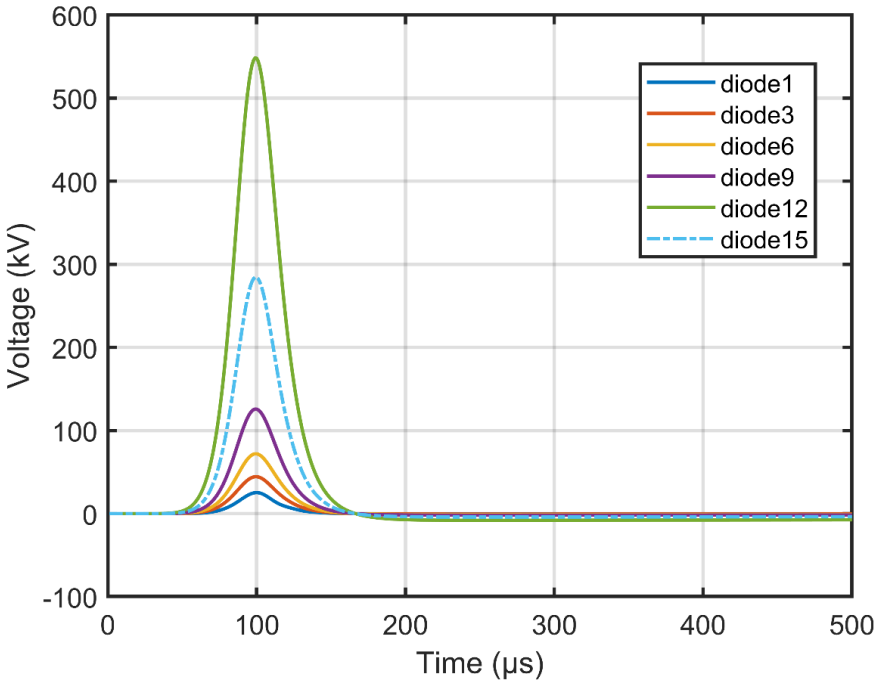

Figure 4.8 Voltage across each diode when directly hitting the left end of PV array 15

Table 4.5 Voltage peak of each diode when directly hitting the left end of PV array 15

Diode No.	Voltage Peak
diode1	25.29 kV
diode3	44.43 kV
diode6	71.93 kV
diode9	125.76 kV
diode12	548.31 kV
diode15	284.41 kV

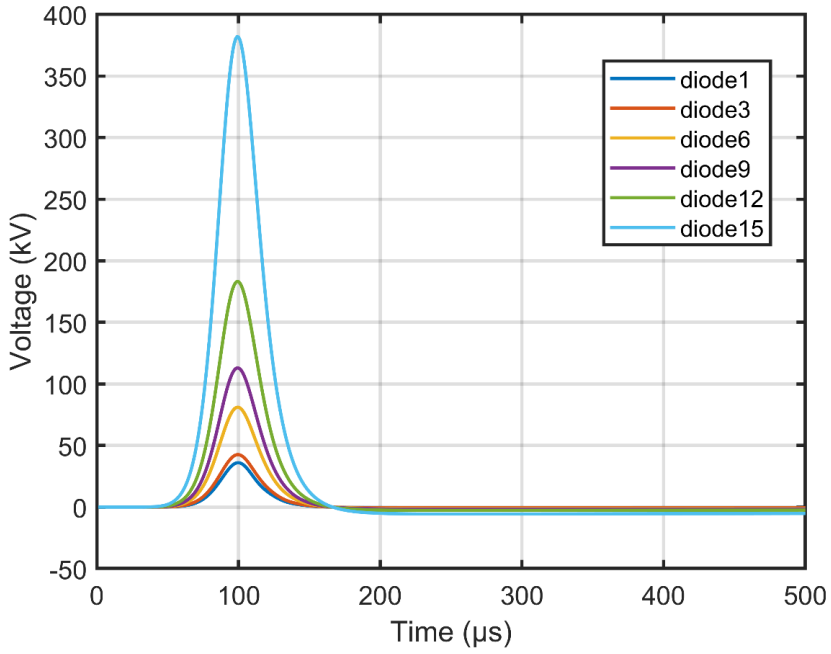

Figure 4.9 Voltage across each diode when directly hitting the right end of PV array 15

Table 4.6 Voltage peak of each diode when directly hitting the right end of PV array 15

Diode No.	Voltage Peak
diode1	36.01 kV
diode3	42.58 kV
diode6	81.04 kV
diode9	112.99 kV
diode12	183.16 kV
diode15	381.95 kV

The simulation results reveal significant variations in diode voltage distributions depending on the lightning strike location across the PV system. When lightning directly strikes the left terminal of PV1, a decreasing voltage gradient is observed from the strike point, with diode3 near the impact zone experiencing the highest voltage of 234.52 kV, while diode15 at the farthest end registers a substantially lower 34.59 kV. Conversely, striking the right terminal of PV1 reverses this

polarity pattern, causing diode1 to surge to 233.30 kV, though voltages at remote components like diode15 drop sharply to 8.15 kV, indicating reduced downstream effects due to current propagation characteristics. More critically, lightning strikes on PV15 demonstrate extreme voltage phenomena, particularly at its left terminal, where diode12 is subjected to a hazardous 548.31 kV—the maximum recorded value—far exceeding standard insulation thresholds and posing severe risks of DC cable breakdown. Strikes on PV15's right terminal show slightly mitigated but still concerning voltages, with diode15 reaching 381.95 kV and diode12 maintaining 183.16 kV, suggesting persistent multi-node stress from ground potential coupling. The analysis further identifies pronounced voltage asymmetry: opposing terminals of the same array yield magnitude differences up to tenfold, as seen in diode3 (234.52 kV) versus diode15 (8.15 kV) during PV1 terminal strikes. Diode12 emerges as a consistent vulnerability, sustaining critical overvoltages across multiple strike scenarios. These findings underscore the necessity for location-specific lightning protection strategies, including enhanced insulation for PV15 diodes, optimized DC cable routing to minimize induced voltages, and targeted deployment of surge suppression devices on high-risk components like diode12. Additionally, reassessing grounding system design is crucial to address soil-related amplification effects, given the simulated soil

conductivity (0.01 S/m) and permittivity (ε=10), which likely exacerbate voltage stresses. The results collectively emphasize the importance of dynamic insulation coordination and system-level hardening against geographically dependent lightning threats in large-scale PV installations.

4.2.2 Voltage Between DC Cable and PV Frame

The insulation integrity between live conductors and grounded structures is a critical consideration in photovoltaic (PV) system design, particularly under extreme transient conditions such as lightning events. In large-scale PV installations, the potential voltage difference between energized DC components (e.g., cables carrying generated power) and grounded metallic structures (e.g., PV module frames) poses a fundamental risk of insulation breakdown. This phenomenon becomes especially critical during direct lightning strikes to PV arrays, where the massive transient currents and induced voltages can create extreme potential gradients across system components.

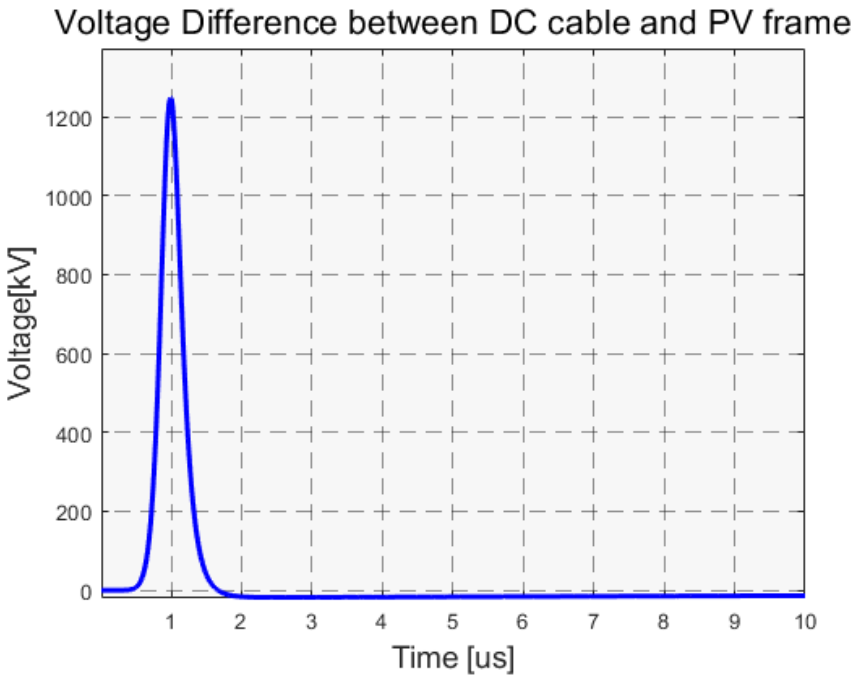

Figure 4.10 Voltage between DC cable and PV frame of PV array 1 when when directly hitting the right end of PV array 1

The calculation results are shown in Figure 4.8. As can be seen from the figure, when lightning strikes a photovoltaic array directly, the voltage across the block diode exceeds 40 kV, and the voltage difference between the PV frame and the DC cable exceeds 1200 kV. This is much greater than the breakdown voltage of the diode and the line insulation of the low-voltage distribution network. This shows that direct lightning strikes pose a significant threat to the insulation of the block diode and DC cable in large-scale photovoltaics.

Existing electrical standards typically define insulation coordination requirements based on conventional low-voltage distribution network parameters. However, the unique configuration of PV systems – with

extended DC cabling distances, distributed grounding points, and surge current paths through module frames – creates complex voltage stress scenarios that conventional protection strategies may not adequately address. The blocking diodes in PV strings, designed to prevent reverse currents under normal operation, become particularly vulnerable during such high-energy transients due to their limited voltage withstand capability.

This calculation specifically examines the worst-case scenario of a direct lightning strike to a PV array, where the instantaneous energy injection creates a transient voltage difference between the DC cables and adjacent grounded PV frames. The analysis focuses on quantifying this potential difference to evaluate whether it exceeds the dielectric strength of system insulation components, including cable insulation layers and semiconductor devices. The results demonstrate extraordinary voltage stresses surpassing 1200 kV, orders of magnitude higher than the typical insulation levels specified for low-voltage electrical equipment.

Such extreme voltage disparities not only threaten immediate insulation failure but also create cascading risks of arc formation, equipment damage, and potential fire hazards. The findings emphasize the necessity for specialized surge protection measures and revised insulation coordination approaches in utility-scale PV installations,

particularly in lightning-prone regions. This investigation provides crucial data for optimizing system topology, enhancing grounding strategies, and selecting appropriate voltage-rated components to mitigate direct lightning impacts on PV system reliability.

4.3 Induced Lightning

This part examines the effects of the distance between induced lightning and the photovoltaic system on the overvoltage across the blocking diode in large-scale photovoltaic systems. It also analyzes the impact of the induced lightning current waveform on the overvoltage across the blocking diode. For simplicity, the term "diode" will be used to refer to the blocking diode in the following parts of this part.

4.3.1 The Influence of Hitting Distance

This subsection discusses the effect of the distance between the induced lightning and the PV system on the blocking diode terminal voltage. The lightning waveform is 1/50 μs and the current amplitude is 10 kA. the distances are set as 0.5 km, 1 km, 1.5 km, and 2 km, respectively, and the overvoltages at the terminals of diode 15, diode 8, and diode 1 are investigated from near to far from the lightning.

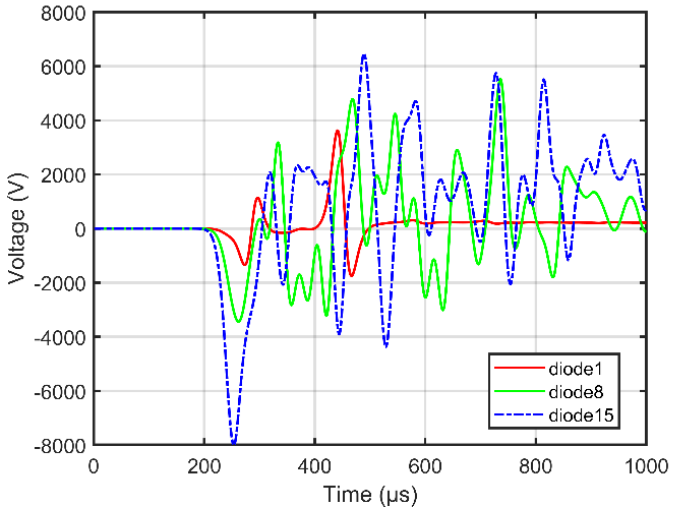
8000
6000
4000
2000
0
-2000
-4000
-6000
-8000
Voltage (V)
0
200
400
600
800
1000
Time (μs)
diode1
diode8
diode15

(a) 0.5km

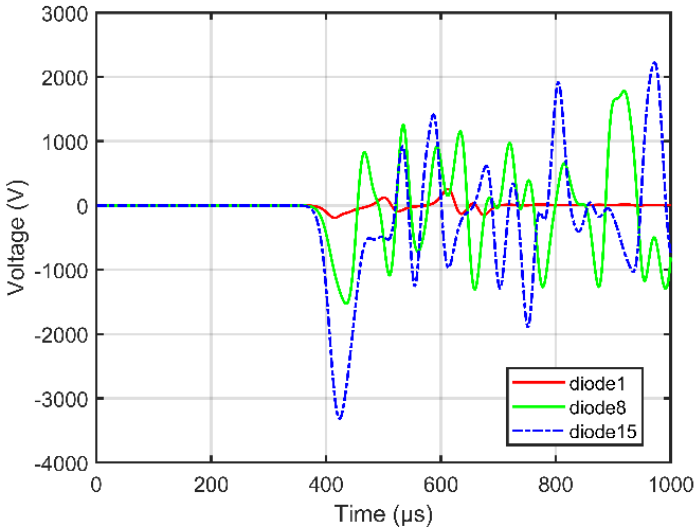
3000
2000
1000
0
-1000
-2000
-3000
-4000
Voltage (V)
0
200
400
600
800
1000
Time (μs)
diode1
diode8
diode15

(b)1km

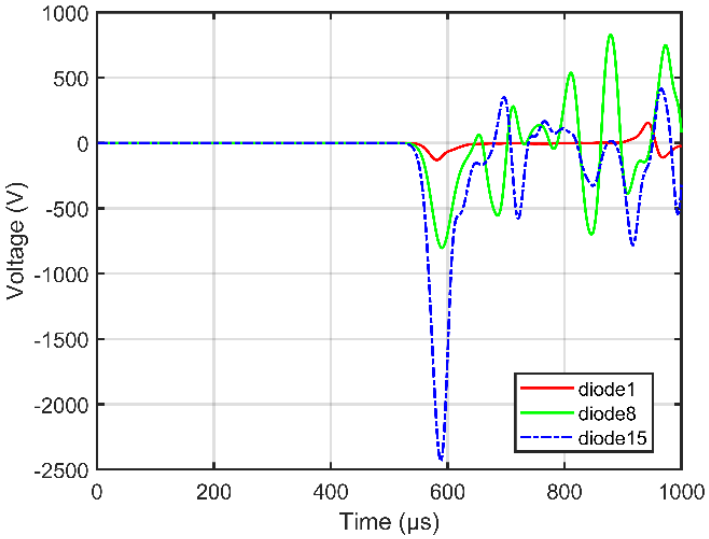
1000
500
0
-500
-1000
-1500
-2000
-2500
Voltage (V)
0
200
400
600
800
1000
Time (μs)
diode1
diode8
diode15

(c)1.5km

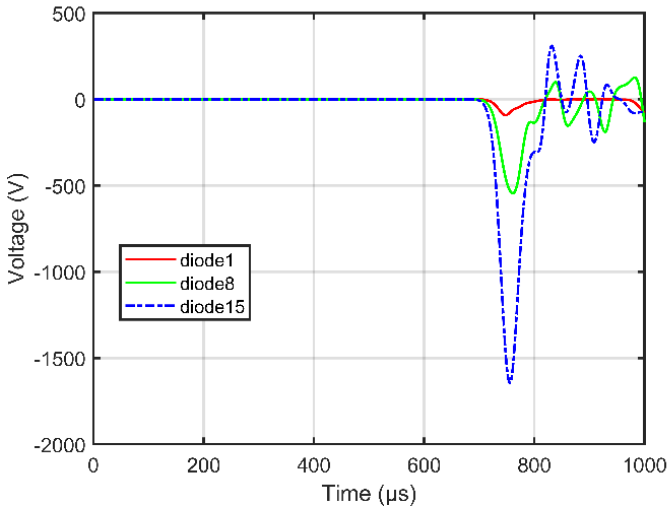
500
0
-500
-1000
-1500
-2000
Voltage (V)
0
200
400
600
800
1000
Time (μs)
diode1
diode8
diode15

(d)2km

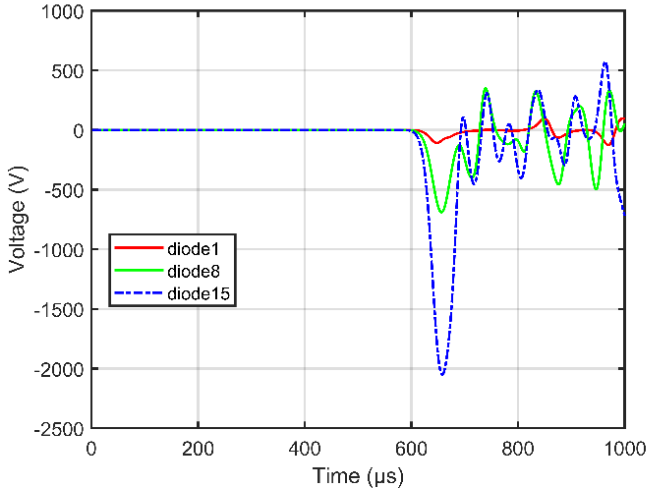

(e)1.7km

Figure 4.11 Effect of distance on the voltage across diode1, diode8 and diode15

Table 4.7 Amplitude of voltage across diode1, diode8, diode15 at different distances

Voltage(V)	Diode1	Diode8	Diode15
0.5 km	3626.5	5525.6	7999.4
1 km	256.5	1780.9	3315.8
1.5 km	155.1	830.0	2434.6
2 km	92.1	545.2	1643.1

Effect of distance on the voltage across diode1, diode8, and diode15 is shown in Figure 4.9, while amplitude of voltage across diode1, diode8, and diode15 at different distances is presented in Table 4.7. From Figure 4.9 and Table 4.7, the following conclusions can be drawn:

1) As the distance between the induced lightning and the photovoltaic system increases, the overvoltage across all three diodes decreases significantly. As the distance increases from 0.5 km to 2 km, the voltage across diodes 1, 8, and 15 decreases substantially, indicating that the

impact of induced lightning on the photovoltaic system weakens as the distance grows. This demonstrates that the influence of induced lightning is limited in range, and the farther the distance, the smaller the threat to the system.

2) At the same induced lightning distance, diodes closer to the induced lightning (e.g., diode15) experience significantly higher voltages than those farther away (e.g., diode1). For instance, at a distance of 0.5 km, the voltage across diode15 reaches 7999.4 V, while that across diode1 is only 3626.5 V. This indicates that in a photovoltaic system, diodes located farther from the inverter are more susceptible to higher overvoltage and require focused protection.

3) When the voltage across a diode exceeds 2 kV, it will be damaged [155]. At a minimum distance of 2 km between the induced lightning and the photovoltaic system, the voltage across diode15 was already below 2 kV. To further analyze the critical range, simulations were conducted for distances between 1.5 km and 2 km. The results, as shown in Figure 4.11 (e), indicate that at a distance of 1.7 km, the voltage across diode15 was slightly above 2 kV (2050 V). Therefore, under the current simulation configuration, 1.7 km is identified as the critical distance at which the diode is at risk of damage.

4.3.2. ~~The~~ The Influence of Lightning Current Waveform

This subsection discusses the impact of the induced lightning current waveform on the voltage across diode15. The lightning current amplitude is set to 10 kA, and the soil conductivity is 0.01.

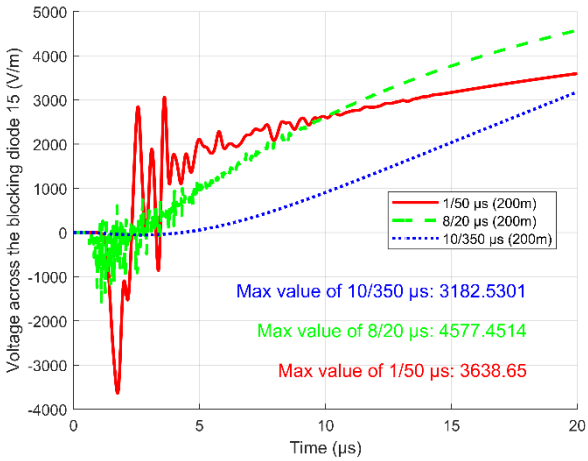

(a)

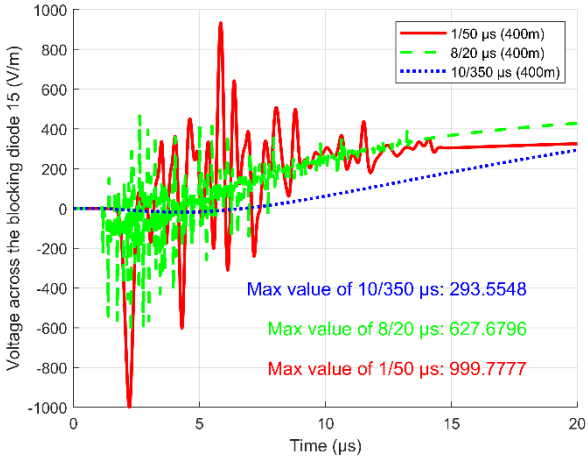

(b)

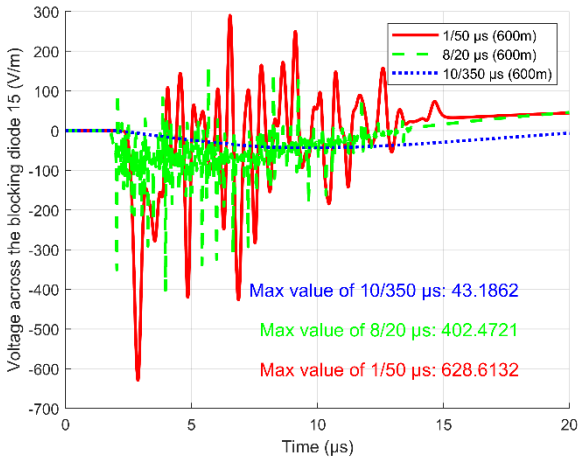
1/50 µs (600m)
8/20 µs (600m)
10/350 µs (600m)
Max value of 10/350 µs: 43.1862
Max value of 8/20 µs: 402.4721
Max value of 1/50 µs: 628.6132
Voltage across the blocking diode 15 (V/m)
Time (µs)

(c)

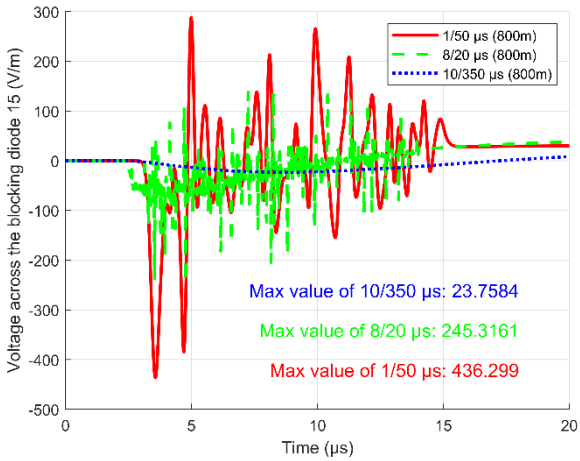
1/50 µs (800m)
8/20 µs (800m)
10/350 µs (800m)
Max value of 10/350 µs: 23.7584
Max value of 8/20 µs: 245.3161
Max value of 1/50 µs: 436.299
Voltage across the blocking diode 15 (V/m)
Time (µs)

(d)

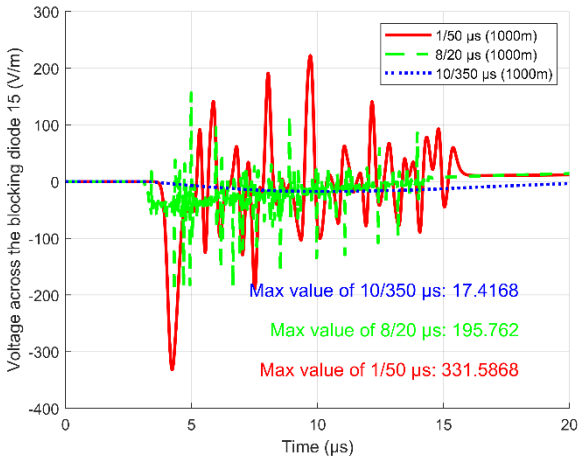

(e)

Figure 4.12 The Impact of Lightning Current Waveform on the Overvoltage Across Diode15: (a) 200 m, (b) 400 m, (c) 600 m, (d) 800 m, (e) 1000 m

The impact of lightning current waveform on the overvoltage across diode 15, at different distances: (a) 200 m, (b) 400 m, (c) 600 m, (d) 800 m, and (e) 1000 m, is shown in Figure 4.10. From the figure, the following conclusions can be drawn:

In the first 15 µs, the voltage oscillation across diode15 induced by the lightning current waveform is most pronounced for the 1/50 µs waveform, followed by the 8/20 µs waveform, and least pronounced for the 10/350 µs waveform. This indicates that sharper wavefronts in the induced lightning current waveform lead to more severe initial voltage fluctuations.

Except for the case at 200 m, where the peak voltage in the tail portion

of the 8/20 μs waveform exceeds that of the 1/50 μs waveform, the induced lightning current waveform with 1/50 μs generally results in the highest overvoltage across diode15, followed by 8/20 μs, and then 10/350 μs at all other distances.

This analysis highlights that the overvoltage across diode15 is significantly influenced by the characteristics of the induced lightning current waveform and its wavefront steepness.

4.4 Summary

This chapter has presented a comprehensive analysis of lightning-induced transients in large-scale photovoltaic systems through detailed electromagnetic modeling and simulation studies. The full-component modeling approach successfully captures the complex interactions between PV arrays, DC cabling networks, and grounding systems under both direct and induced lightning conditions. The simulation results reveal critical vulnerabilities in system components that conventional protection strategies often overlook.

The direct lightning strike analysis demonstrates the extreme voltage stresses imposed on PV system components, particularly highlighting the asymmetric voltage distribution patterns across different array locations. The findings show that strike position significantly influences voltage propagation characteristics, with terminal strikes generating

substantially higher overvoltages compared to central impacts. Of particular concern is the identification of diode 12 as a persistent weak point, sustaining hazardous overvoltages exceeding 500 kV in certain scenarios. The frame-to-cable voltage measurements further confirm the severe insulation stress during direct strikes, with potential differences surpassing 1200 kV - far beyond standard component ratings.

For induced lightning events, the study establishes clear relationships between strike distance and overvoltage magnitude. The critical finding of a 1.7 km risk radius provides valuable guidance for protection zone design. Waveform analysis further reveals the significant influence of lightning current characteristics, with fast-fronted impulses producing more severe transient responses. These insights collectively demonstrate the need for location-specific and waveform-adaptive protection strategies in PV system design.

The comprehensive modeling framework developed in this chapter provides a robust foundation for optimizing lightning protection measures. The results emphasize three key design considerations: enhanced insulation coordination for vulnerable components, improved grounding system topology to mitigate potential differences, and strategic placement of SPD based on electromagnetic coupling patterns. These findings directly inform the protection optimization strategies

developed in subsequent chapters, bridging the gap between theoretical analysis and practical engineering solutions for large-scale PV installations.

Chapter 5
Grounding and Cable Configuration Optimization for PV Lightning Protection

The computational results of direct and induced lightning strikes in Chapter 4 demonstrate that large-scale photovoltaic (PV) systems face significant risks of diode damage due to lightning transients. To mitigate these risks, this chapter systematically explores potential optimization strategies to reduce lightning-induced overvoltages and enhance the resilience of PV components.

A critical factor influencing lightning protection efficacy is soil conductivity, which directly governs the grounding resistance of the PV system's lightning protection network (LPN). As discussed earlier, lower soil conductivity exacerbates overvoltage levels by impeding the dissipation of lightning currents, thereby increasing induced voltages across PV cables and diodes. For instance, simulations reveal that soil conductivity below 0.001 S/m can induce peak voltages exceeding 3.5 kV in simplified PV circuits (Section 5.1), highlighting its pivotal role in system safety.

Beyond soil properties, the design of the lightning protection system and PV array configuration significantly impact overvoltage suppression. Key variables include the number of grounding electrodes

and the geometric layout of DC cables. For example, sparse grounding points or extensive cable loops amplify electromagnetic coupling effects during lightning events, as evidenced by the 2.5 kV frame-to-cable voltages observed in direct strikes (Section 5.2). Conversely, strategic design modifications—such as reducing cable loop dimensions—can attenuate these risks.

This chapter evaluates three primary optimization parameters: (1) soil conductivity's influence on transient responses (Section 5.1), (2) the role of increased grounding electrodes in mitigating direct-strike overvoltages (Section 5.2), and (3) the benefits of smaller DC cable loops for diode protection during induced lightning (Section 5.3). The findings aim to guide practical improvements in PV system resilience against lightning threats.

5.1 Influence of the Effect of Soil Conductivity on Calculation Results

5.1.1 Simplified PV DC Lines

In this section, we investigate the influence of soil conductivity (σ) on lightning-induced transients in photovoltaic (PV) systems. To isolate the impact of soil resistivity, we adopt a simplified "gate" circuit as an analytical model. This circuit represents the fundamental structure of PV DC distribution lines, which typically consists of parallel

conductors (e.g., cables and grounding wires) arranged in a loop-like configuration—similar to the gate circuit's geometry. The gate circuit's upper conductor mimics the PV DC cable, while the grounding body corresponds to the PV system's grounding network. By studying this simplified setup, we can extrapolate the behavior of larger PV arrays under lightning surges, as both systems share key electromagnetic coupling mechanisms. The gate circuit's parameters include a copper grounding conductor (radius = 0.005 m) and a grounding body (radius = 0.01 m), subjected to a 10 kA lightning current (1/200 μs waveform) at a 50 m distance.

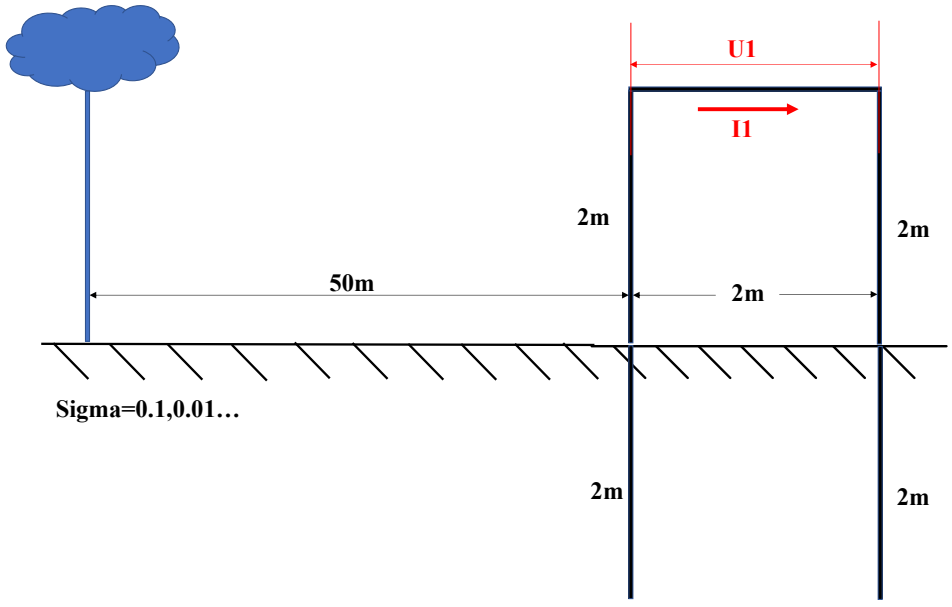

Figure 5.1 Gate circuit

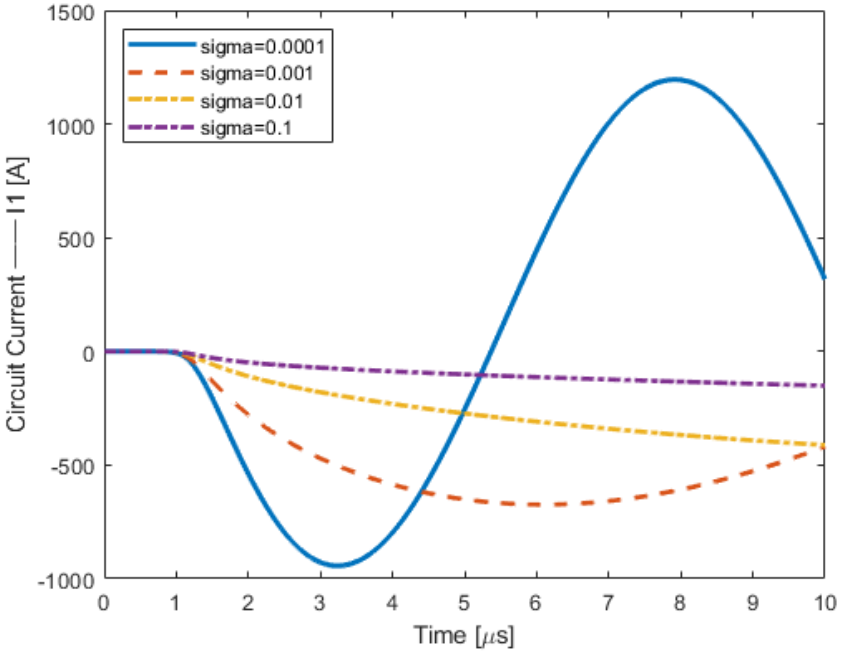

(a)Effect of different soil conductivity on gate current

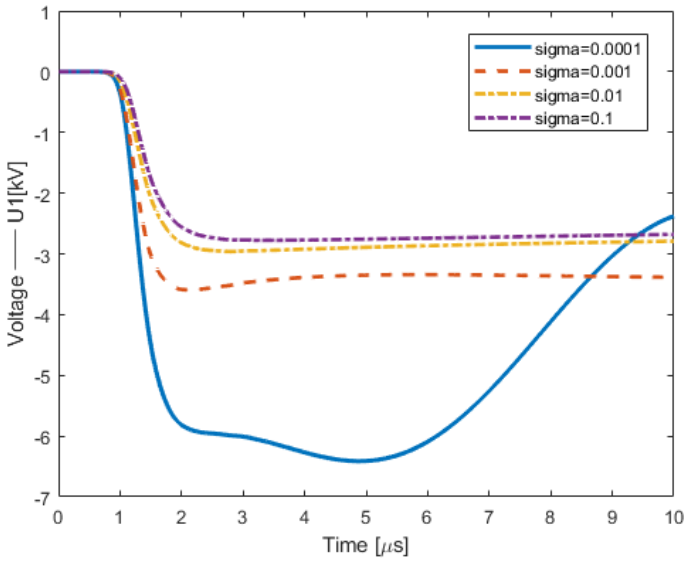

(b)Effect of different soil conductivity on gate current

Figure 5.2 Effect of different soil conductivities on the voltage across conductors on gate circuits

As shown in Figure 5.2, the greater the soil conductivity, the smaller the current flowing through the "gate" circuit, and the lower the voltage across the conductors of the "gate" circuit. When sigma reaches 0.001 or less, the peak value of the induced voltage U1 exceeds 3.5 kV, and the loop current I1 also exceeds 600 A. This indicates that σ has a significant impact on the calculation results, with lower sigma values being more likely to cause higher induced voltages.

5.1.2 Large-scale Photovoltaic Systems

Table 5.1 Models used in this research work

Item	Model
PV arrays	PEEC model
Grounding structure	PEEC model
DC cable	PEEC model
AC cable	PEEC model
Inverter	lumped circuit model
Power transformer	lumped circuit model

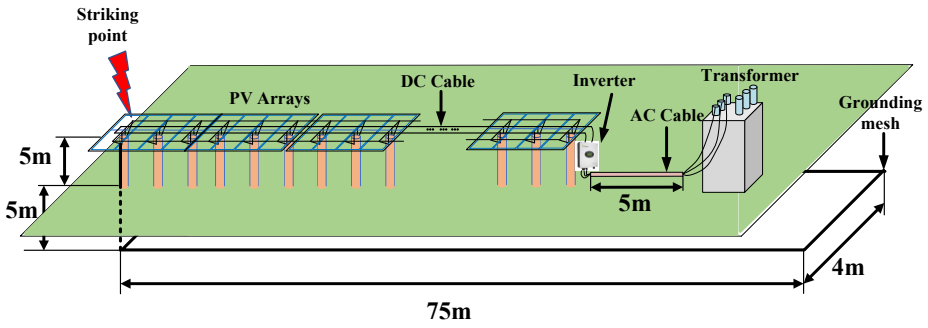

Figure 5.3 Structure of a Large-Scale Photovoltaic Power Generation System

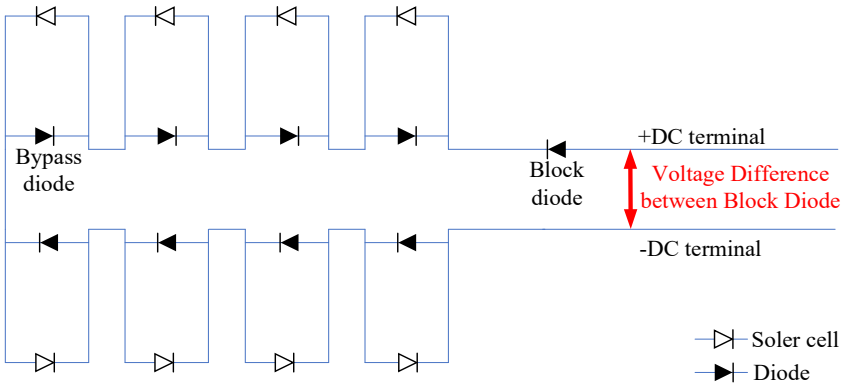

Figure 5.4 Arrangement of the photovoltaic DC cables

Induced lightning was simulated for the same large-scale photovoltaic power generation system. The lightning waveform is 1/50us with the amplitude of 10kA, and the lightning channel is modeled using the TL model. The lightning strike point is 120 meters away from the photovoltaic system. The dielectric constant is 10, and the soil conductivity ranges from 1 to 0.0001 S/m.

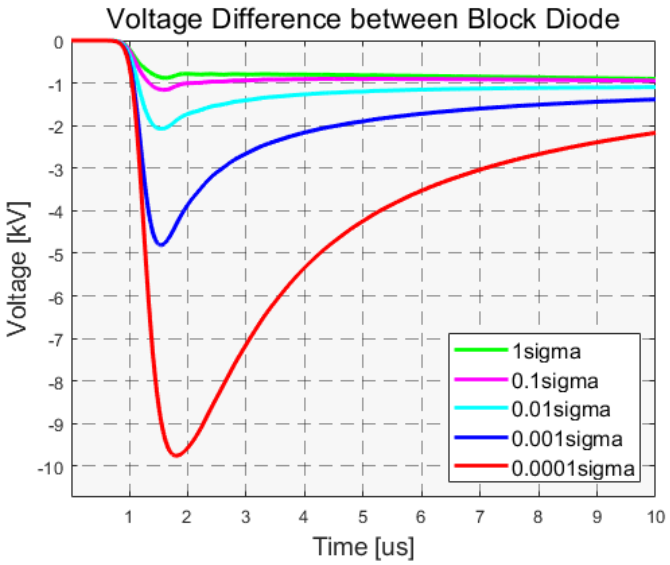

Figure 5.5 Voltage Difference between block diode in induced lightning

The calculation results are shown in Figure 5.5. As seen in the figure, as soil conductivity decreases, the voltage across the blocking diode increases. When the soil conductivity reaches 0.01 S/m, the voltage difference has risen to 2 kV, putting the diodes at risk of permanent breakdown. Therefore, even in the case of induced lightning, the blocking diode of a large-scale photovoltaic power generation system remains vulnerable to permanent damage.

5.2 The Impact of The Number of Grounding Rods on Direct Lightning Strikes

5.2.1 Overvoltage in Direct Lightning

For large-scale photovoltaic power plants, in addition to the potential damage to the blocking diodes, the large size of the photovoltaic frame may cause residual voltage on the frame due to a direct lightning strike, which could break through the insulation layer of the DC cable. A direct lightning simulation was conducted for the same large-scale photovoltaic power generation system. When the entire photovoltaic system is subjected to a direct lightning strike, the voltage across the blocking diode and the voltage between the photovoltaic frame and the DC cable were calculated. The dielectric constant is 10, and the soil conductivity is 0.01 S/m.

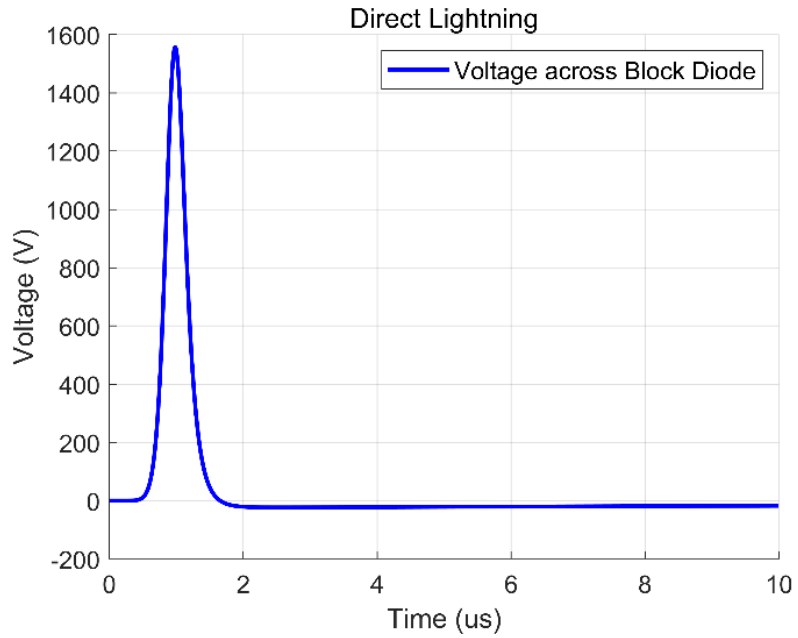

(a) Voltage across block diode

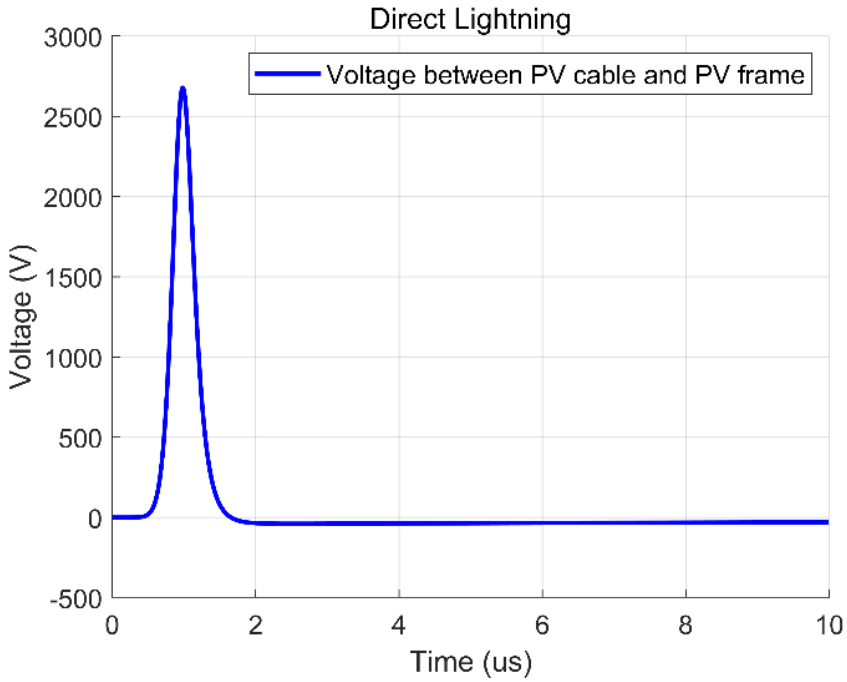

(b) Voltage between dc cable and PV frame

Figure 5.6 Voltage Difference in direct lightning

The calculation results are shown in Figure 5.6. As illustrated, when lightning strikes a photovoltaic array directly, the voltage across the blocking diode exceeds 1.5 kV, while the voltage difference between the PV frame and the DC cable surpasses 2.5 kV. These values are significantly higher than the breakdown voltage of the diode and the line insulation of the low-voltage distribution network. This demonstrates that direct lightning strikes pose a severe threat to the insulation of the blocking diode and DC cable in large-scale photovoltaic systems.

5.2.2 Improvement by Increasing the Number of Grounding Poles

As shown in Figure 5.3, the current large-scale photovoltaic system has only one grounding electrode at the lower-left corner connected to the ground network. To reduce the induced overvoltage between the photovoltaic cable and the insulated frame, the number of grounding electrodes on the entire photovoltaic frame was increased to six, with one electrode added every 14 meters, all connected to the ground network. A comparison was made between the improved grounding system and the original system, and the voltage between the photovoltaic cable and the photovoltaic frame was calculated. The calculation results are shown in Figure 5.7. From the figure, it can be seen that after increasing the number of grounding electrodes, the

overvoltage level has been significantly reduced.

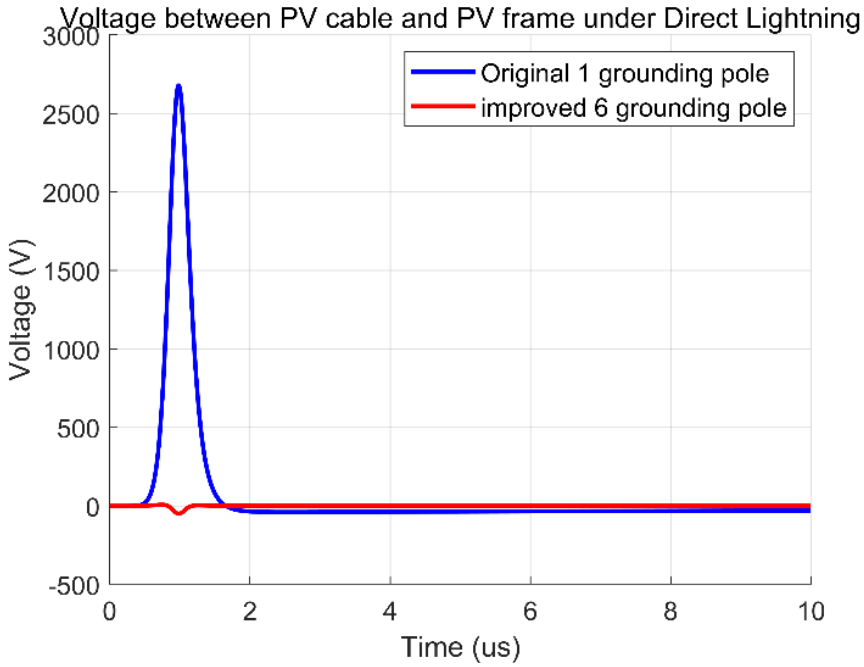

Figure 5.7 Comparison of the voltage between the photovoltaic cable and the photovoltaic frame with the improved 6-grounding poles system versus the original 1-grounding pole system

5.3 The Influence of Smaller Coil Design on the Voltage across A Diode During Induced Lightning

5.3.1 Overvoltage across Block Diode in Induced Lightning

In the DC cable of the photovoltaic system, there are two types of diodes: bypass diodes and blocking diodes. When the voltage across the blocking diode reaches 100V, there is a risk of damage to the diode. To address the breakdown risk of blocking diodes under induced lightning transients, the novel potential-line coupling method was used to

simulate induced lightning for this large-scale photovoltaic power generation system. The lightning waveform is shown in Figure 5, and the lightning channel is modeled using the transmission line (TL) model. The distances between the lightning strike point and the photovoltaic system were set to 120 m, 170 m, 200 m, 250 m, and 300 m, with a dielectric constant of 10 and a soil conductivity of 0.01 S/m.

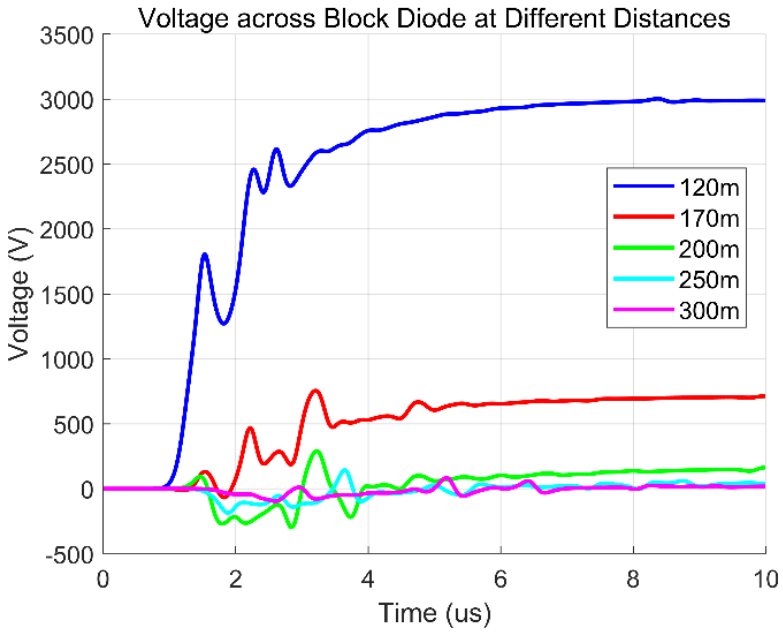

(a)120m, 170m, 200m, 250m, 300m

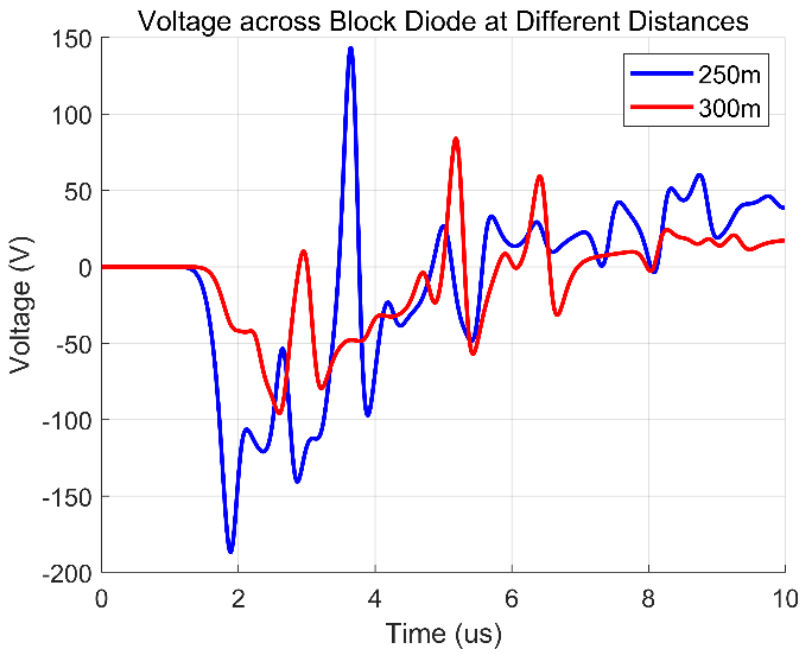

(b)250m, 300m

Figure 5.8 Voltage Difference between block diode in induced lightning at different distances

The calculation results are shown in Figure 5.8. As can be seen from Figure 8(a), as the distance of the induced lightning decreases, the voltage across the blocking diode increases sharply. When the distance is 120 meters, the voltage rises to around 3 kV, putting the diode at risk of permanent breakdown. From Figure 5.8(b), it can be seen that when the distance is reduced to 250 meters, the voltage decreases to about 140 V, and when the distance is 300 meters, the voltage drops below 100 V. Therefore, even in the case of induced lightning, the blocking diode of a large-scale photovoltaic power generation system remains susceptible to permanent damage, especially when the lightning strike

distance is within 300 meters.

5.3.2 Modification of the PV Cable Loop to A Smaller Coil Design

Due to the long length of the existing photovoltaic cable loop, the length of the photovoltaic cable in this system is 70 meters and the width is 2 meters. To reduce the induced voltage across the diodes, the shape of the photovoltaic DC cable was modified. A small loop unit of 13 meters was used, with interleaved connections made every 13 meters. The schematic diagram of the modification is shown in Figure 5.9. Based on this, a comparison was made between the induced voltage transients across the blocking diodes before and after the modification, with calculations performed at three selected distances: 120 meters, 170 meters, and 200 meters.

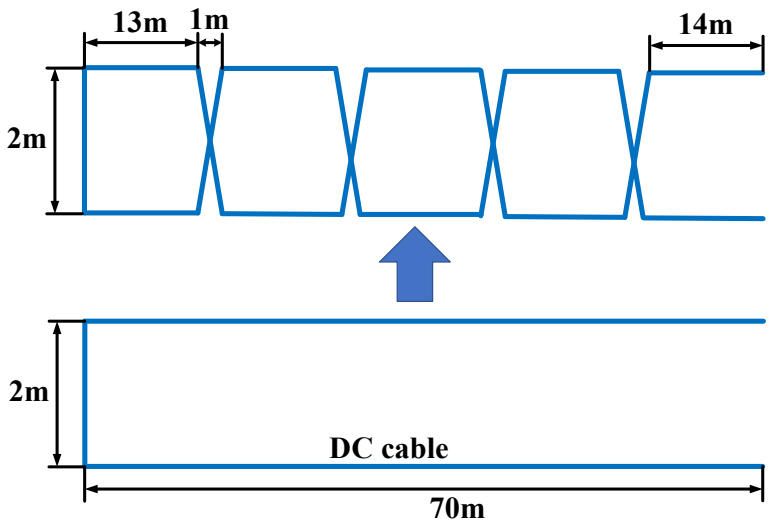

Figure 5.9 Schematic diagram of the modification of the PV cable loop to a smaller coil design

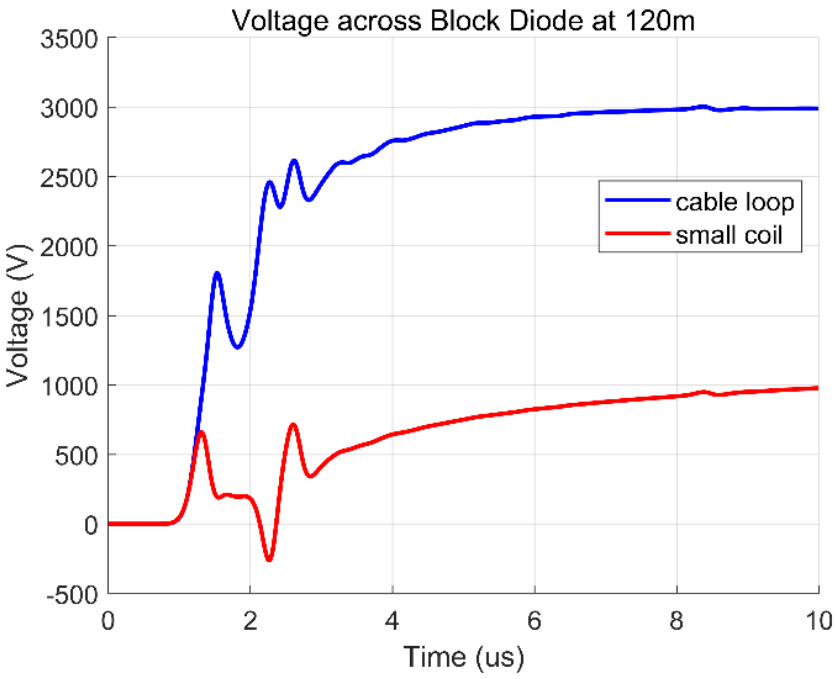
Voltage across Block Diode at 120m
3500
3000
2500
2000
1500
1000
500
0
-500
Voltage (V)
0
2
4
6
8
10
Time (us)
cable loop
small coil

(a)120m

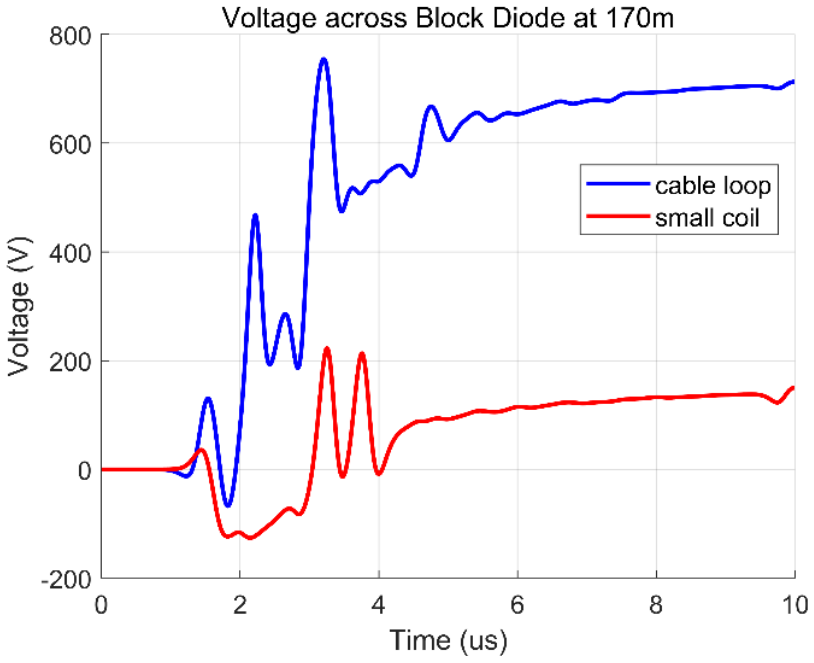
Voltage across Block Diode at 170m
800
600
400
200
0
-200
Voltage (V)
0
2
4
6
8
10
Time (us)
cable loop
small coil

(b)170m

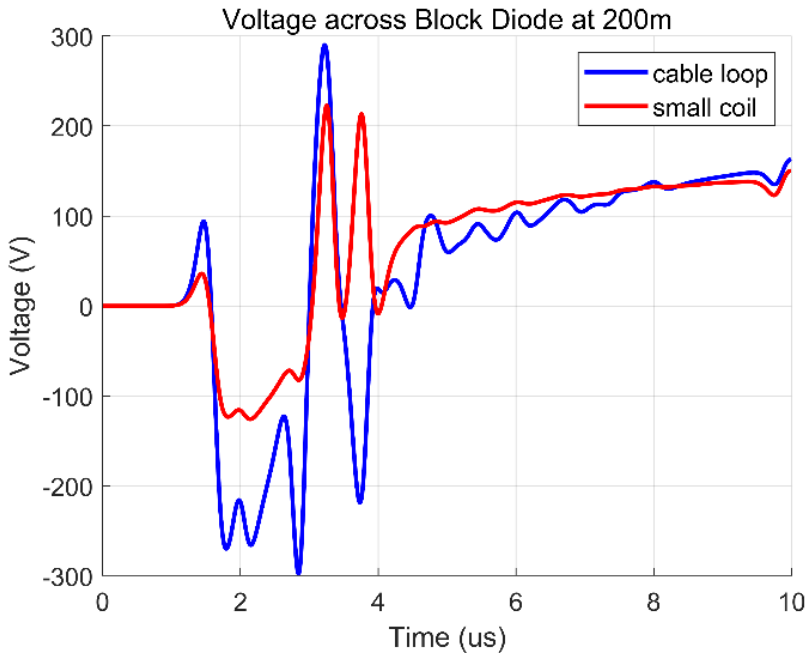

(c)200m

Figure 5.10 Voltage across the block diode at different distances with modification of the cable design (small coil) and original cable loop.

The calculation results are presented in Figure 5.10. As shown in the figure, the improved small coil design significantly reduces the induced overvoltage across the blocking diodes, particularly for distances within 170 meters. This design can be applied in the installation and operation of photovoltaic power plants in the future to better protect the diodes.

5.4 Summary

This chapter has systematically investigated three key optimization strategies for enhancing lightning protection in large-scale photovoltaic systems. The parametric studies demonstrate that soil conductivity

plays a fundamental role in determining transient overvoltage levels, with lower conductivity soils (below 0.01 S/m) creating significantly higher risks of diode breakdown. The findings reveal a critical threshold where soil conductivity reductions lead to exponential increases in induced voltages, necessitating special design considerations for installations in high-resistivity regions.

The grounding system optimization study establishes that increasing the number of grounding electrodes from one to six provides substantial overvoltage reduction during direct lightning strikes. This improvement is attributed to better current distribution and reduced potential differences across the PV array. The results suggest that distributed grounding strategies can effectively mitigate insulation stress, particularly when combined with proper soil treatment techniques in high-resistivity locations.

The cable layout modification study introduces an innovative small-coil design that demonstrates remarkable effectiveness in reducing induced overvoltages. By decreasing loop dimensions from 70m to 13m, the system achieves significant attenuation of electromagnetic coupling effects, particularly for near-field lightning events within 170m. This geometric optimization presents a practical solution that can be readily implemented in new installations while offering potential retrofit opportunities for existing systems.

Collectively, these optimization strategies provide actionable guidelines for improving PV system resilience against both direct and induced lightning threats. The chapter's findings bridge theoretical analysis with practical engineering solutions, offering a comprehensive approach to lightning protection that considers soil conditions, grounding topology, and cable layout simultaneously. These insights directly inform the risk assessment methodologies developed in subsequent chapters, creating a cohesive framework for system-level protection design.

Chapter 6

Comprehensive Analysis of Grounding Strategies for Hybrid AC/DC PV Networks

In this section, we delve into the implications of varied grounding setups on the comprehensive hybrid AC/DC system. The entirety of the grounding scheme encompasses two facets: (a) Incorporating surge protective devices (SPDs) linked at both ends of the inverter and grounded via the PV grounding frame, and (b) Employing SPDs connected at both ends of the transformer, grounded through the star-side neutral of the transformer.

Subsection 6.1 centers on grounding options for the cable armor layer, exploring grounding via the left end of the PV frame, the right end of the transformer, and both ends concurrently. Subsection 6.2 investigates the removal of the SPD on the inverter's AC side, discussing how the grounding of PV frame and transformer connections shapes the distribution of overvoltage across the entire system. Lastly, in Subsection 4.3, we assess the practicability of minimizing the number of SPD groups in diverse PV panel grounding scenarios by eliminating the SPD on the low-voltage side of the transformer. Within Subsection 6.3, we group every three PV panels and detail their grounding arrangement as depicted in Figure 4(a). Subsequently, we analyze the

cable voltage impact for cases involving 9 and 18 groups of PV arrays.

The soil resistivity is set to be 0.01, and the relative permittivity is set to 10. To simulate a lightning strike, a current waveform with a duration of 1/50 μs and an amplitude of 100 kA is applied directly to the PV, and the striking point is shown in Fig. 6.1(a).

A dedicated ground grid is provided for a transmission tower for effectively discharging the lightning current into the ground. The grounding electrode arrangements are depicted in Fig. 6.1(b). For vertical rods, the radius is 0.05m, length is 2.5m, while for horizontal lines, the radius is 0.005m, length is 20m, and depth is 1m. More detailed grounding arrangements of transmission towers can be found in [148].

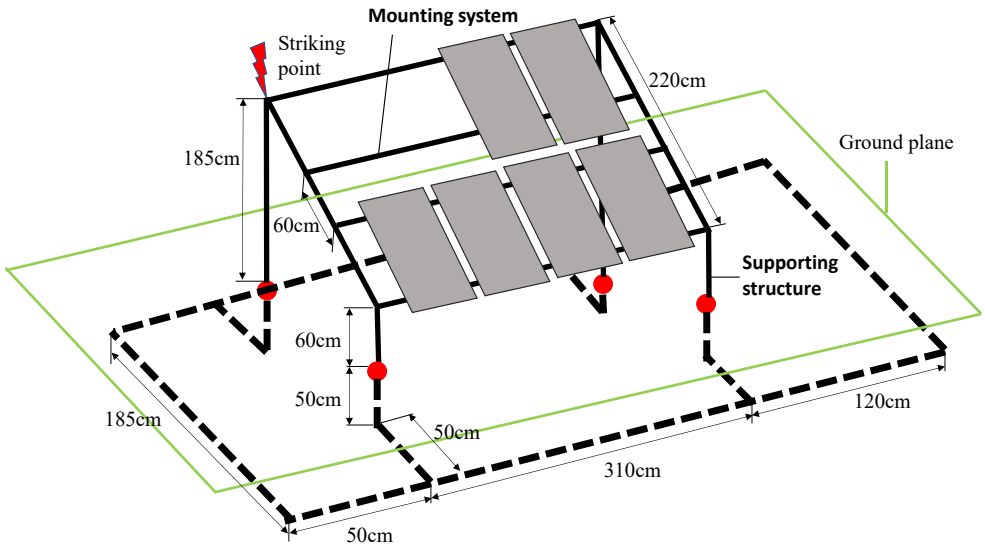

(a)

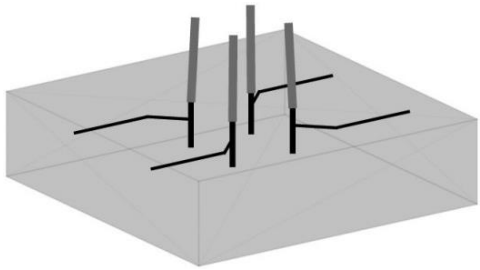

(b)

Figure 6.1 (a) Configuration of a PV panel system (b)Schematic diagrams of grounding electrodes of transmission tower

6.1. The Influence of Cable Grounding

In a power distribution system, the cable provides a connection between the PV inverter and the power transformer, with its length determined by the distance between them. The cable consists of a sheath, armor, and three internal cores. The armor can either be grounded at both ends or grounded at one end with PV or transformer grounding. When the cable length is significant, the wave propagation can lead to surge overvoltage under a lightning strike, subsequently leading to a higher potential overvoltage in the core lines. Currently, there are no specific standards for grounding the power cable sheath used in photovoltaic (PV) systems. Although in some instances, engineers ground one end of the power cable sheath to prevent circulating currents on the grounded sheath, the overall impact of the grounding method on the cable and the system remains unclear. Therefore, it is essential to explore the effect of a grounding method at both ends of the cable in the context of PV integration in order to assess operational risks during

lightning strikes and to determine suitable grounding schemes for mitigating such risks.

The simulation is performed to investigate the impact of various grounding conditions of the cable enclosure under a direct lightning strike to the PV frame, as shown in Fig. 6.1. The lightning strike is characterized by a 1/50 μs current waveform with an amplitude of 100 kA. The core-to-ground overvoltage at different locations at the distances of 0m, 20m, 40m, and 80m on an 80m-long cable from its left end was simulated. Specifically, the effect of grounding the cable at the left end, right end, or both ends of the cable is analyzed, as depicted in Fig. 6.2. Fig. 6.3 shows the overvoltages between core and sheath on the cables under three different grounding arrangements. Their Peak overvoltage values are summarized in Table 6.1.

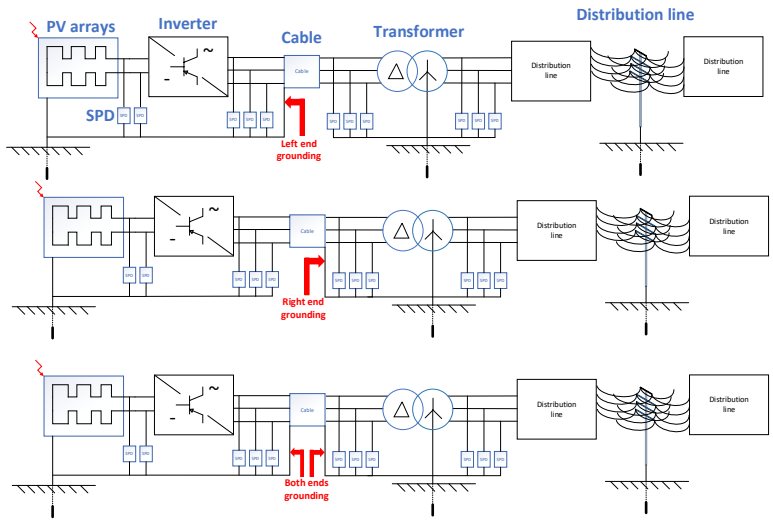

Figure 6.2 Grounding of the left end, right end, and both ends (from top to bottom) of the cable sheathing

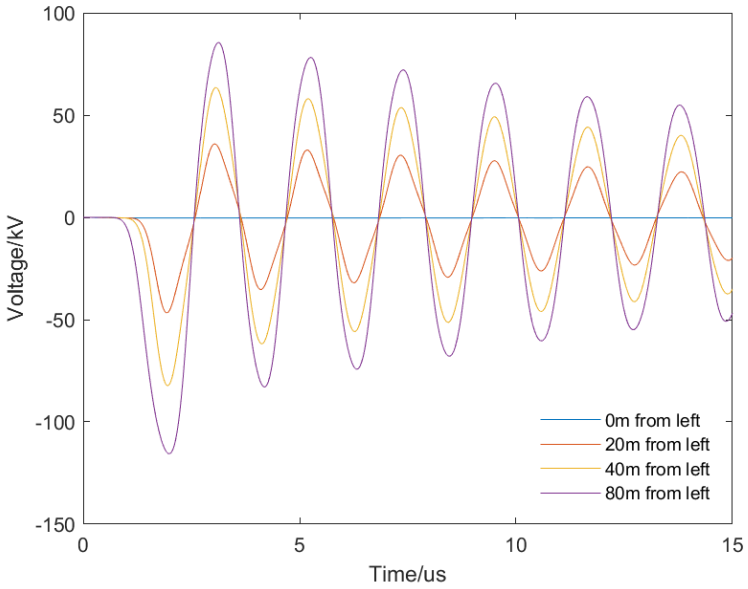
100
50
0
-50
-100
-150
Voltage/kV
0
5
10
15
Time/us
0m from left
20m from left
40m from left
80m from left

(a)

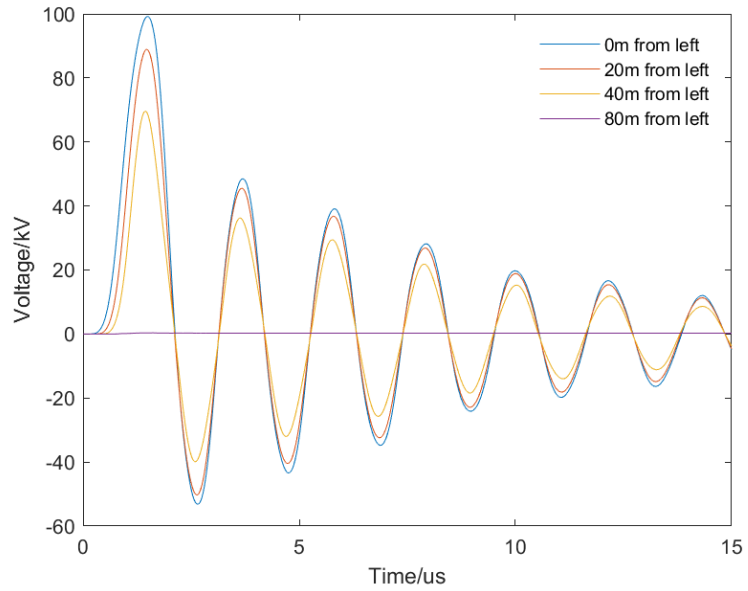
100
80
60
40
20
0
-20
-40
-60
Voltage/kV
0
5
10
15
Time/us
0m from left
20m from left
40m from left
80m from left

(b)

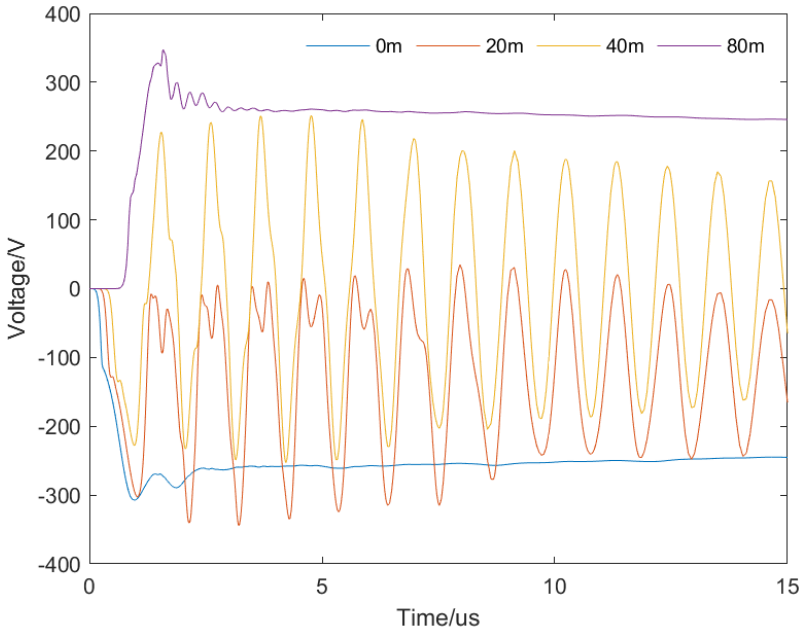

(c)

Figure 6.3 Distribution of overvoltage from cable cores to cable insulation sheath at different locations of the cable when the (a) left end, (b) right end, (c) both ends of the cable is grounded

Table 6.1 Distribution of peak overvoltage cable cores to cable insulation sheath at different locations of the cable when the left end, right end, and both ends of the cable is grounded

Peak voltage	0m	20m	40m	80m
Left end grounding	307.80V	46.66kV	82.26kV	115.54kV
Right end grounding	99.18kV	88.89kV	69.59kV	360.55V
Both ends grounding	307.31	344.12	252.88	347.17

From the results, the grounding configuration of the cable sheathing significantly affects the voltage between cable cores and sheath. Grounding the left end of the cable sheathing results in a core voltage

of 307.80V at that point, which rises to 46.66kV 20m away and reaches 115.54kV at the right end, exceeding the rated voltage(several kV) of low-voltage cables by over four times and posing a significant risk to cable operation. Similarly, grounding the right end leads to a core voltage of 360.55V at that point, rising to 69.59kV 40m away and reaching 99.18kV at the left end. In contrast, when both ends are grounded, the core-to-sheath overvoltage throughout the cable remains below 350V, ensuring normal operation during direct lightning strikes in the new energy system.

These findings provide valuable insights into the optimal grounding configurations to mitigate overvoltage risks and ensure the reliable operation of the cable system. To ensure the proper functioning of the system, it is advisable to ground the armor layer at both cable ends through the respective grounding systems. This precaution helps mitigate the risk of excessive overvoltage occurring between the cable core and its outer shell during lightning strikes on the PV panels, preventing potential cable damage.

6.2 The Influence of PV Panel Numbers

To reduce the potential risks associated with lightning surges, it is a common practice to connect electrical equipment in distribution networks with SPDs on both ends. These SPDs serve to suppress

overvoltages that may affect equipment, such as inverters and transformers. However, in the distribution system, it is theoretically possible to eliminate the need for installing a set of SPDs at both ends of the cable when the cable length is short. Given the increasing integration of large-scale new energy systems, substantial cost savings can be achieved by omitting the installation of a set of SPDs under specific operating conditions. Simulation is then performed to investigate the impact on the transformer instead of the inverter when an SPD is not connected at the left end, taking into account the low voltage withstand performance of the inverter. In the simulation, we consider the scenarios with 18 PV panels and 9 PV panels. Expanding on the findings from Subsection A, it's crucial to emphasize that proper grounding is necessary for both ends of the cable armor.

Figure 6.4 depicts the layout of 18 PV panels. In the case of 9 PV panels, the ones within the dashed box will remain unconnected. Dividing the PV panels into three groups, each connected to a single inverter, results in six such groups. These groups are then consolidated into a total cable length of 100m, achieved through cables of lengths 10m, 20m, and 30m respectively. (In the case of 18 PV panels, 3 groups are formed). The grounding arrangement of each PV panel is depicted in Figure 6.1.

In this scenario, we examine the impact of different cable lengths on the A phase overvoltage between core line and sheath when the left end of

the transformer is not connected to an SPD. The location of the striking point is illustrated in Fig. 6.4. The resulting A phase line overvoltage between core line and sheath is analyzed for cable lengths of 10m, 20m, 40m, 60m, and 80m of 18-PV-array-system and 9-PV-array-system, as shown in Fig. 6.6. The corresponding peak overvoltages are summarized in Table 6.2.

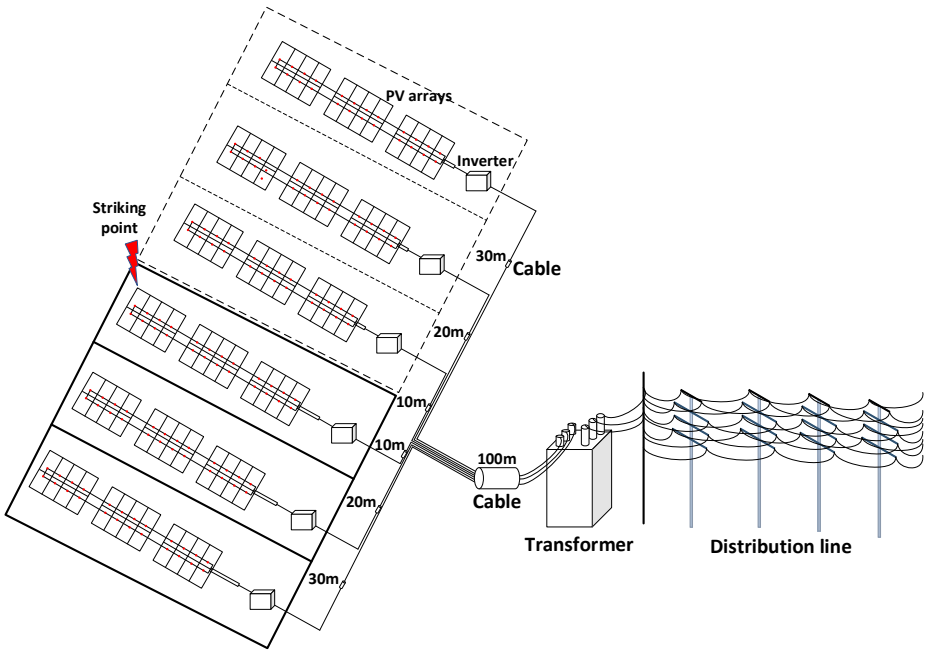

Figure 6.4 Schematic diagram of the distribution network with 18 PV arrays

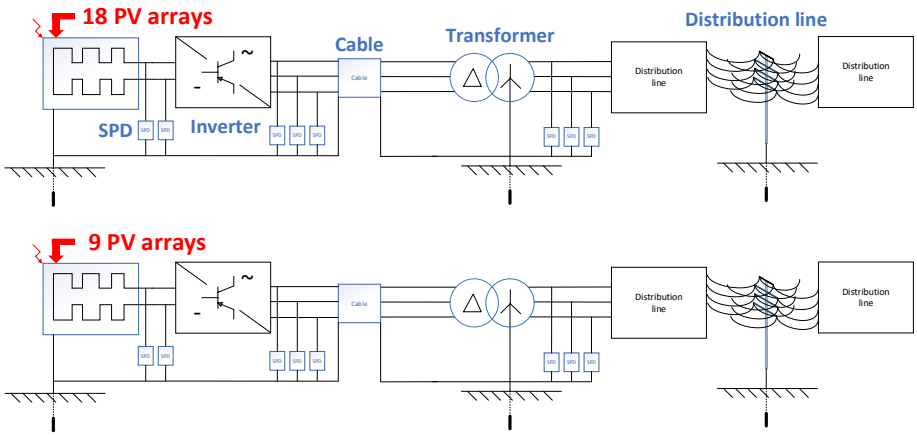

Figure 6.5 No SPD at left of transformer with 18 PV arrays connection

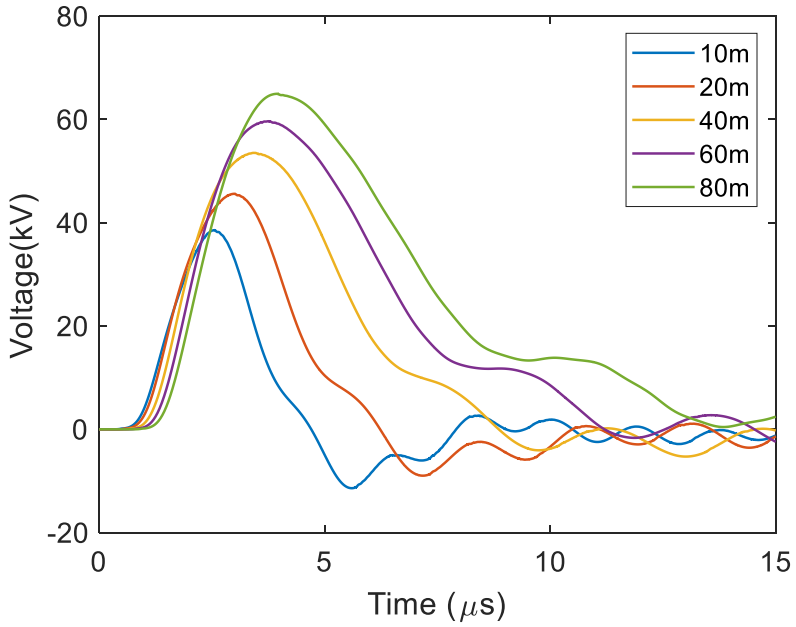

(a)

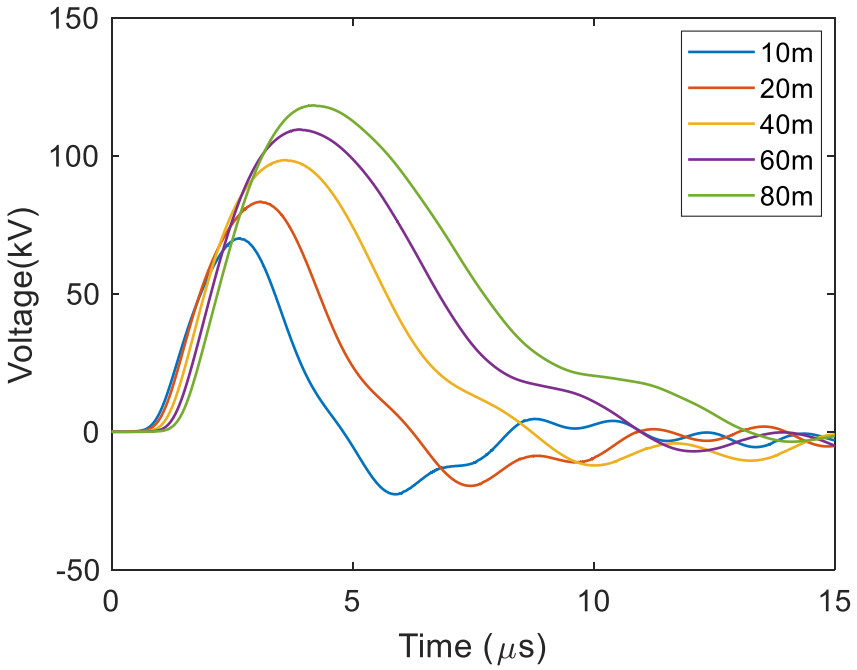

(b)

Figure 6.6 Distribution of overvoltage to ground at different distances from the left of the cable when there is no SPD at the left of the transformer with (a) 18 PV arrays (b) 9 PV arrays connection

Table 6.2 Distribution of peak overvoltage to the ground at a different distance from the left of the cable when there is no SPD at the left of the transformer with 18 PV and 9 PV arrays connection

Distance	10m	20m	40m	60m	80m
18 PV arrays	38.56 kV	45.60 kV	53.52 kV	59.65 kV	64.96 kV
9 PV arrays	70.08 kV	83.30 kV	98.42 kV	109.50 kV	118.24 kV

The study results indicate a consistent trend, irrespective of whether the distribution network is connected to 18 or 9 PV panels. When a surge protector is connected to the left end of the low-voltage cable between the inverter and the transformer, with no SPD at the right end, an intriguing phenomenon unfolds: the core-shell voltage at the cable's

rightmost end increases proportionally with the cable length. Furthermore, a comparative analysis of different cable lengths reveals a noteworthy observation – the core surge overvoltage under 18 fast PV panels consistently exceeds that under 9 PV panels, regardless of the cable length. It can be observed that the overvoltage in the system with 18 photovoltaic (PV) panels is less than that in the system with 9 PV panels. This is because the system with 18 PV panels has more grounding electrodes, which significantly reduces the grounding resistance, thereby decreasing the overvoltage in the system. Consequently, the study suggests that as the number of PV panels increases, the core surge overvoltage tends to decrease.

A significant discovery from the study emphasizes that even with a maximum of 18 PV panels connected to the same inverter, the core surge overvoltage on the shortest cable length (10 meters) reaches an alarming 38 kV, surpassing the normal operating voltage of the cable. Hence, the installation of a set of surge arresters at both ends of the cable is deemed essential to mitigate potential risks.

6.3 The Influence of Whole System Grounding

The grounding system of the hybrid AC-DC system encompasses various components, including PV panel grounding, cable grounding, transformer grounding, and distribution line grounding. In this study,

the distribution of line-to-ground overvoltage in the entire system is examined under different grounding scenarios for the PV panel, cable, and transformer, both with and without interconnection. The line-to-ground voltage is composed of three distinct components: the +DC line-to-ground voltage at the PV panel, the A-phase line-to-ground voltage between the cable and the transformer, and the A-phase line-to-ground voltage at the distribution line. The system configuration, as depicted in Figure 6.7, illustrates the upper section of the system grounded without interconnection, while the lower section of the system is grounded with interconnection.

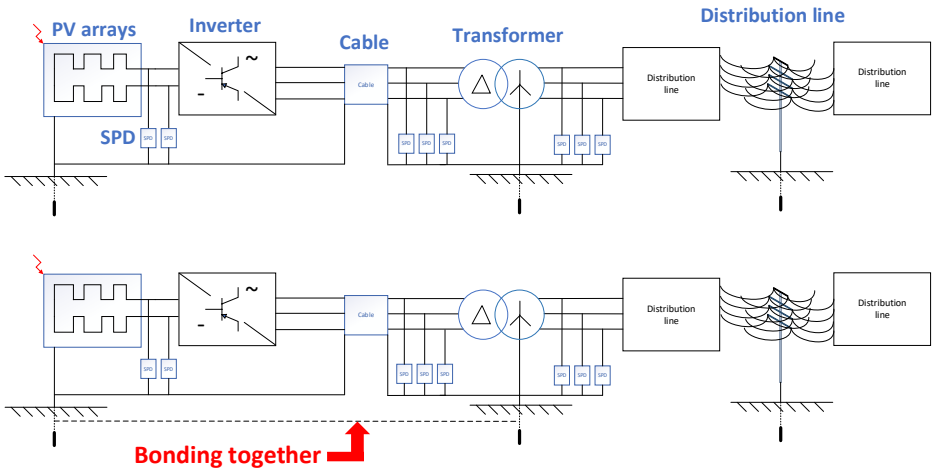

Figure 6.7 Schematic diagram of AC-DC hybrid system with isolated grounding: above is the system parts grounded not connected to each other, below is the system parts grounded to each other

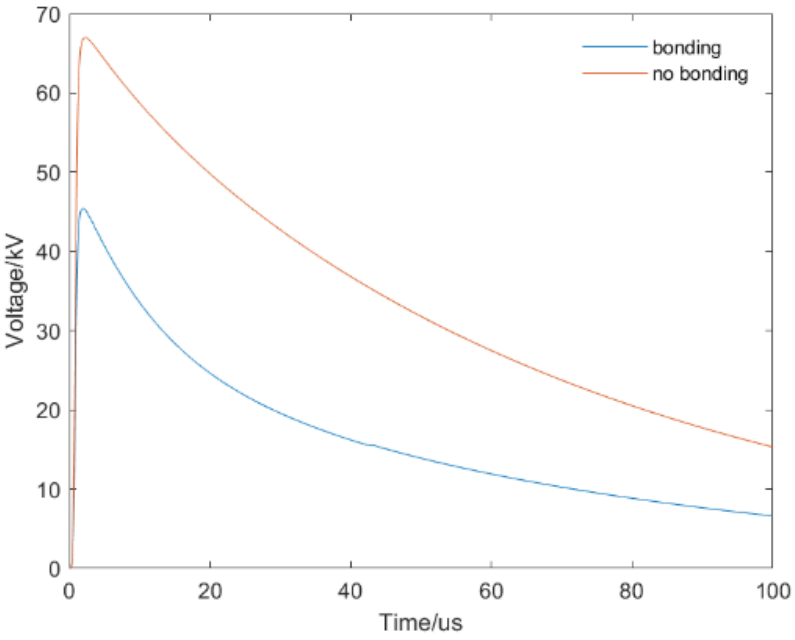
bonding
no bonding
Voltage/kV
Time/us
70
60
50
40
30
20
10
0
0
20
40
60
80
100

(a)

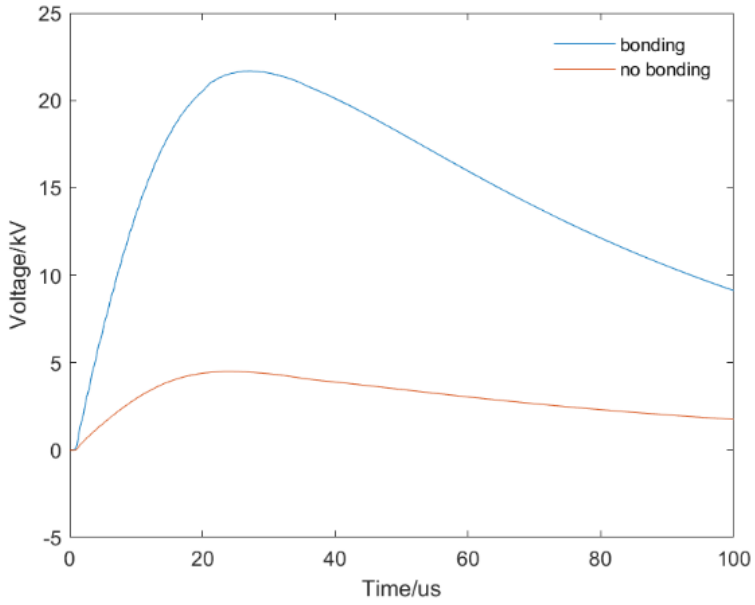
bonding
no bonding
Voltage/kV
Time/us
25
20
15
10
5
0
-5
0
20
40
60
80
100

(b)

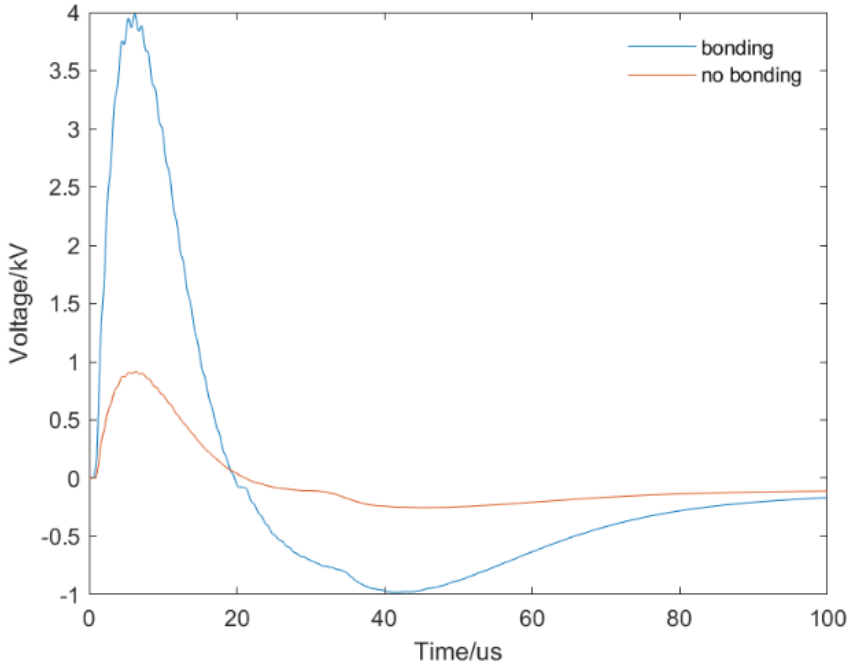

(c)

Figure 6.8 Line voltage to ground of (a) +DC line voltage (b) Voltage between cable and transformer (c)Distribution line voltage when the whole system bonding together or not

Table 6.3 Statistics of voltage amplitude to ground at each part of the system when the AC-DC hybrid system is connected to ground or not

	+DC line voltage	The voltage between cable and transformer	Distribution line voltage
Grounding connection	45.440	21.68	3.98
No connection	66.98	4.49	0.92

Figure 6.8 displays the voltage to ground of the PV panel + DC line, the voltage to ground between the cable and the transformer, and the voltage to ground of the distribution line. Table 6.3 provides statistical information regarding the magnitude of the voltage to ground at each component of the system when the AC-DC hybrid system is grounded or ungrounded.

The findings indicate that when a lightning strike impacts on the PV panel, grounding the system with interconnection yields a lower over-voltage at the lightning strike point, while other system components experience higher over-voltages. This observation suggests that grounding interconnection helps to balance the energy of the lightning strike by significantly reducing the over-voltage at the point of impact. Consequently, while the over-voltage of distant lines in the system increases, it remains within the acceptable range of line insulation and lightning resistance. Such an outcome is advantageous for enhancing the system's lightning protection level. In the context of the AC/DC hybrid system, interconnecting the grounding of different system components can be employed as a means to bolster the overall lightning resistance level of the system.

6.4 Photovoltaic Integration into AC Grid

The grid connection of a PV array to the AC system is a crucial process facilitated by an inverter. However, limited studies have explored the impact of the connected AC side system on the PV array during lightning events. This knowledge gap necessitates an investigation into the effects of lightning strikes on the PV frame, particularly concerning the ground overvoltage of the PV panel + DC line. A comparative analysis is conducted between two scenarios: one where the PV array is connected to the entire AC system, and another where it is directly

connected to the LVDC. Figure 6.9 illustrates the system configuration, depicting the PV array integrated into the entire AC system in the upper section and the PV array directly connected to the LVDC in the lower section. By examining these two setups, valuable insights can be gained regarding the ground overvoltage characteristics under lightning conditions. In the Low Voltage Direct Current (LVDC) system, the wire with a negative polarity at the DC end is connected to the ground through a grounding electrode. This connection to the ground establishes it as the reference potential [158]. The grounding electrode used in this setup is a steel rod with a length of 0.5 meters and a radius of 0.01 meters. This rod is buried at a depth of 0.5 meters below the surface.

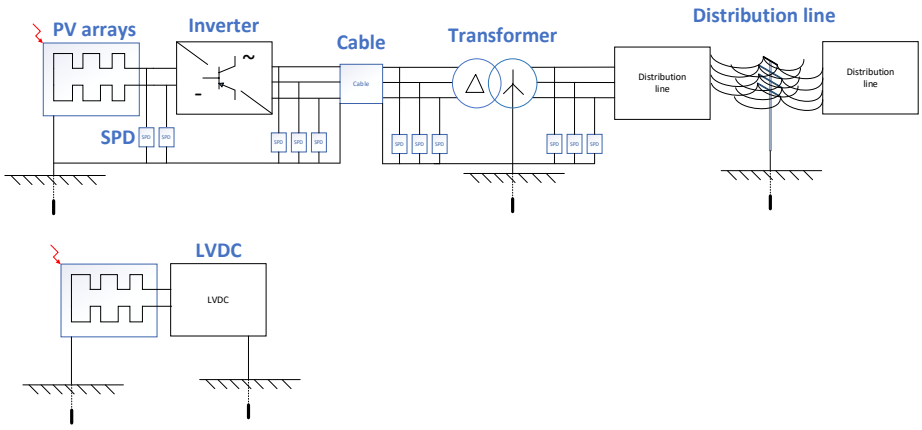

Figure 6.9 Diagram of whether PV is connected to the grid or not: above is PV connected to the whole AC system, below is PV directly connected to LVDC

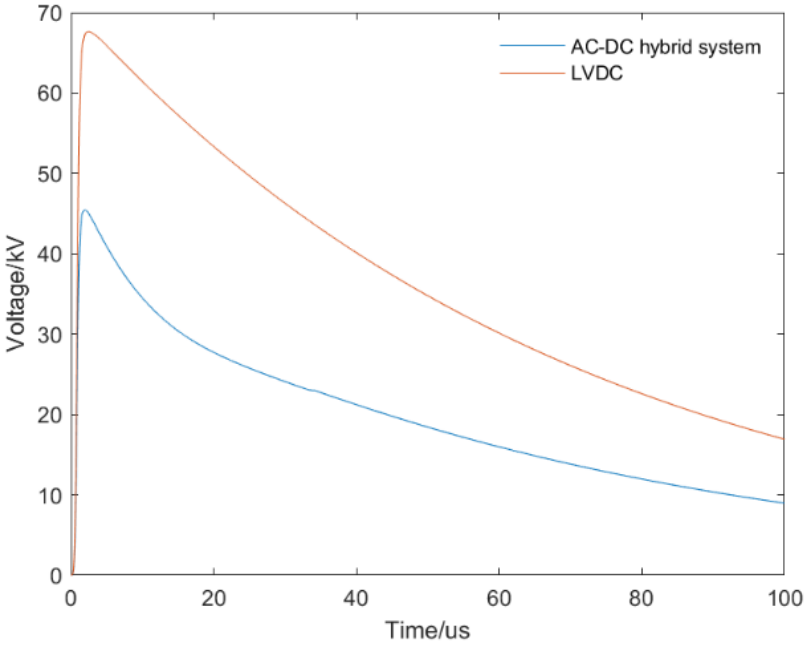

Figure 6.10 +DC line voltage

The voltage of the PV panel + DC line to ground is depicted in Figure 6.10, with respective magnitudes of 45.45 kV and 67.64 kV. These findings lead to the conclusion that connecting the PV array to the entire AC system effectively mitigates the system overvoltage compared to the direct connection to LVDC. This implies that the incorporation of the PV array into the AC system provides advantages in terms of reducing overvoltage levels.

6.5 Summary

This chapter has systematically investigated the dynamic grounding characteristics of hybrid AC/DC photovoltaic systems under lightning conditions, providing critical insights into optimal protection strategies.

The cable grounding analysis reveals that dual-end grounding of cable armor layers effectively limits core-to-sheath voltages below 350V during direct strikes, compared to hazardous levels exceeding 100kV with single-end grounding configurations. This finding establishes clear engineering guidelines for cable installation practices in PV systems, particularly for long cable runs between inverters and transformers.

The study of PV panel quantity effects demonstrates an inverse relationship between system grounding density and overvoltage magnitude. Systems with 18 PV panels exhibit approximately 45% lower surge voltages than those with 9 panels, highlighting how distributed grounding electrodes collectively enhance system resilience. However, the results also caution that even optimized configurations require surge protective devices at both cable ends, as core voltages can still reach 38kV in large arrays - far exceeding standard insulation ratings.

The comprehensive system grounding analysis provides compelling evidence for interconnected grounding networks in hybrid AC/DC systems. While interconnected grounding increases overvoltages at remote system components during strikes, it achieves the crucial benefit of reducing voltages at the impact point by up to 32%, effectively redistributing transient energy across the network. This balanced approach proves particularly valuable for protecting sensitive PV

components while maintaining all system voltages within insulation withstand capabilities.

The grid integration study completes the chapter by quantifying the protective benefits of full AC system interconnection, showing 33% lower DC line overvoltages compared to standalone LVDC configurations. This finding underscores the importance of considering complete system topology in lightning protection design, rather than treating PV arrays as isolated DC systems. Together, these investigations form an integrated framework for optimizing grounding system design in utility-scale photovoltaic installations, addressing both component-level protection and system-wide energy distribution during transient events.

Chapter 7

Zoned Risk Assessment Methodology for Large-Scale PV Lightning Protection

Large-scale photovoltaic (PV) systems face unique challenges in lightning risk assessment due to their distributed geometry, extensive surface area, and complex electromagnetic coupling effects. Unlike traditional power distribution networks—where lightning protection focuses on centralized infrastructure like transmission towers—PV arrays exhibit spatially stochastic vulnerability patterns. The random nature of lightning strikes, combined with the system's low-profile but conductive structure, necessitates a probabilistic approach to quantify risks such as direct strikes, induced overvoltages, and cascading failures. However, conventional risk assessment methods, primarily developed for power grids, are ill-suited for PV applications. Deterministic models fail to capture multidimensional uncertainties, while brute-force Monte Carlo simulations, though accurate, demand prohibitive computational resources for utility-scale PV farms.

Existing lightning risk methodologies for power networks rely heavily on electro-geometric models (EGMs) and full-system Monte Carlo sampling. While these approaches provide rigorous statistical results, their computational cost scales poorly with PV system size. For instance,

a non-simplified Monte Carlo analysis of a 75 m × 70 m PV array (Section 7.2.1) requires 242.9 hours to simulate 10,000 lightning events, rendering real-time or iterative design optimization impractical. Moreover, such methods do not exploit the inherent symmetry and zoning characteristics of PV layouts, leading to redundant calculations.

To address these limitations, this chapter introduces a partition-based heuristic algorithm tailored to PV systems. The methodology leverages two key innovations: (1) symmetry-driven computational reduction, where the system is divided into quadrants, and only one representative section (e.g., the lower-right quadrant in Figure 7.3) is analyzed, cutting simulation workload by 75%; and (2) risk-adaptive zoning, which classifies regions into arc induction, quadrant arc, and linear equipotential zones (Sections 7.1.2.1–7.1.2.3) to prioritize high-risk areas while filtering negligible events. By integrating these spatial heuristics with stochastic sampling, the approach achieves a 57.7-fold speedup (Section 7.2.2) with minimal accuracy loss (<1.3% deviation in risk probability).

The chapter further validates the framework through parametric studies on lightning strike density (Table 7.2), evaluation range (Table 7.3), and diode withstand voltage thresholds (Section 7.3). These analyses provide actionable guidelines for balancing computational efficiency and protection reliability, bridging the gap between theoretical models

and engineering constraints. The proposed methodology not only fills a critical gap in PV-specific lightning risk assessment but also establishes a scalable paradigm for resilient renewable energy infrastructure design.

7.1 Current Methodologies and Limitations in Large-Scale PV Lightning Risk Assessment

7.1.1 Empirical Models

The electro-geometric model (EGM) family represents the most widely adopted empirical approach for lightning risk assessment. These models operate on the fundamental principle of calculating attraction radii based on structure height and lightning parameters. The standard implementation involves three key steps:

First, the model defines a rolling sphere radius (typically 30-60m for PV systems) around potential strike points. Any conductive element intersecting this sphere is considered vulnerable to direct strikes. For ground-mounted arrays, this involves projecting the sphere over the entire PV field while accounting for terrain elevation changes.

Second, the attraction radius formula $r_{PV}=k\cdot h^{0.6}$ is applied, where h represents the array height and k a terrain-dependent coefficient. This simplified relationship assumes linear scaling of strike probability with height, neglecting electromagnetic field distortion effects from parallel

DC cables.

Third, risk zones are classified using geometric partitioning - typically dividing the array into high/medium/low risk sectors based on distance from presumed strike points. The model outputs a binary risk map indicating whether each component falls within any attraction radius.

7.1.2 Deterministic Full-Wave Simulations

Full-wave electromagnetic solvers provide physically rigorous solutions by directly solving Maxwell's equations. The finite-difference time-domain (FDTD) method dominates this category due to its adaptability to complex geometries. Implementation involves four core stages:

The modeling process begins with volumetric discretization of the entire PV system into Yee cells. Each cell must satisfy the Courant stability condition $\Delta t \leq 1/c\sqrt{\frac{1}{\Delta x^2}+\frac{1}{\Delta y^2}+\frac{1}{\Delta z^2}}$ to ensure numerical convergence.

Next, the solver implements perfectly matched layer (PML) boundaries to absorb outgoing waves without reflection. For PV systems, special attention is given to ground modeling using multi-layer soil representations.

The excitation phase injects lightning current waveforms at designated

strike points. Field propagation is then computed through iterative time-stepping of the discretized curl equations:

$$\nabla \times \vec{E} = -\mu \frac{\partial \vec{H}}{\partial t} \tag{7.1}$$

$$\nabla \times \vec{H} = \sigma \vec{E} + \epsilon \frac{\partial \vec{E}}{\partial t} \tag{7.2}$$

7.1.3 Stochastic Sampling Methods

Monte Carlo techniques probabilistically evaluate risk through repeated randomized simulations. The standard workflow comprises:

A probability density function (PDF) for lightning parameters is first established, typically using log-normal distributions for peak current Ip and Weibull distributions for rise time tr.

For each iteration, the algorithm:

1) Randomly samples a lightning strike location

2) Draws current waveform parameters

3) Computes electromagnetic response

4) Records overvoltage magnitudes

Importance sampling variants optimize the process by biasing the PDF toward high-risk scenarios through proposal distributions.

7.1.4 Limitations of Existing Methods and Proposed Solution

Current lightning risk assessment approaches for large-scale PV systems exhibit three fundamental deficiencies that hinder their practical application: (1) computational intractability—full-wave simulations require terabytes of memory for GW-scale arrays, while Monte Carlo methods demand weeks of processing time (e.g., 242.9 hours for 10,000 iterations as shown in Section 7.3.1); (2) spatial redundancy—conventional analyses waste >75% of resources evaluating symmetric or low-risk zones; and (3) dynamic threshold neglect—static voltage ratings fail to account for waveform-dependent diode degradation. These shortcomings collectively underscore the urgent need for a paradigm-shifting methodology that balances accuracy with scalability.

The partition-based heuristic algorithm introduced in Section 7.2 addresses these gaps through two synergistic innovations:

Symmetry-driven quadrant reduction—exploiting PV array geometric regularity to analyze only representative sections (e.g., lower-right quadrant in Figure 7.3), cutting simulation workload by 75% while maintaining <1.3% error

Risk-adaptive zoning—classifying regions into arc induction, quadrant arc, and linear equipotential zones (Section 7.2.2) to prioritize high-risk

components like vulnerable diodes

This framework transitions lightning risk assessment from brute-force computation to intelligent spatial optimization, achieving a 57.7× speedup (Section 7.3.2) without compromising the rigor of full-system analysis. The subsequent sections detail its implementation and validation.

7.2 Risk Assessment Methodology for Large-Scale Photovoltaic Systems Using Partition-Based Heuristic Algorithms

7.2.1 Monte Carlo algorithm

Monte Carlo methods are a class of computational algorithms that rely on repeated random sampling to approximate solutions to complex problems characterized by inherent uncertainty or stochasticity. In the context of lightning risk assessment for large-scale photovoltaic (PV) systems, this approach becomes particularly valuable due to the spatially and temporally random nature of lightning strikes, coupled with the intricate interplay of environmental factors, system geometry, and material properties. By generating thousands or millions of simulated lightning events through probabilistic models of key parameters – including strike location, peak current, polarity, and

waveform characteristics – the method enables a statistical analysis of potential damage scenarios. Each simulation incorporates probability distributions derived from historical lightning data, terrain characteristics, and atmospheric physics, while accounting for the PV system's physical layout, grounding configuration, and surge protection measures. The cumulative results provide a probabilistic risk profile that quantifies likelihoods of direct strikes, induced overvoltages, equipment failure rates, and cascading impacts on energy yield. This data-driven approach overcomes the limitations of deterministic models by naturally accommodating multidimensional uncertainties and rare event phenomena inherent in lightning behavior, ultimately supporting optimized lightning protection system design and risk mitigation strategies informed by robust statistical evidence rather than worst-case assumptions.

Figure 7.1(a) provides a global overview of a large-scale photovoltaic (PV) system designed for lightning risk assessment. The layout spans a rectangular area with dimensions of 75 meters by 70 meters, featuring rows of PV panels organized into arrays labeled as "PV Array." Key infrastructure components, including inverters, transformers, and grounding meshes, are strategically positioned across the system. Electrical connections are illustrated through DC and AC cables, linking the PV arrays to inverters and transformers, while a "Lightning

point" marks a potential strike location. The diagram emphasizes the spatial distribution of critical elements, such as surge protection pathways and grounding infrastructure, which are vital for evaluating lightning-induced vulnerabilities.

Figure 7.1(b) offers a detailed top-down view of a subsection within the PV array, highlighting the geometric arrangement of individual PV panels in columnar formations. Labels such as "PV Panel" and "PV Array" clarify the scale and density of the installation, while components like inverters and transformers are shown integrated into the grid-like structure. The simplified background focuses attention on interconnections between panels and electrical pathways, with annotations indicating potential risk zones. This view aids in analyzing localized lightning strike impacts, such as electromagnetic coupling effects on adjacent panels or cascading failures caused by overvoltage propagation through cables.

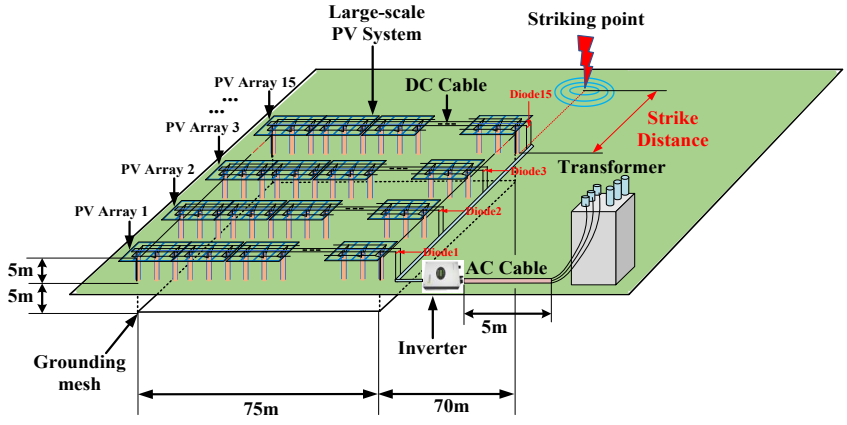

(a) Global Infrastructure and Electrical Connectivity Overview

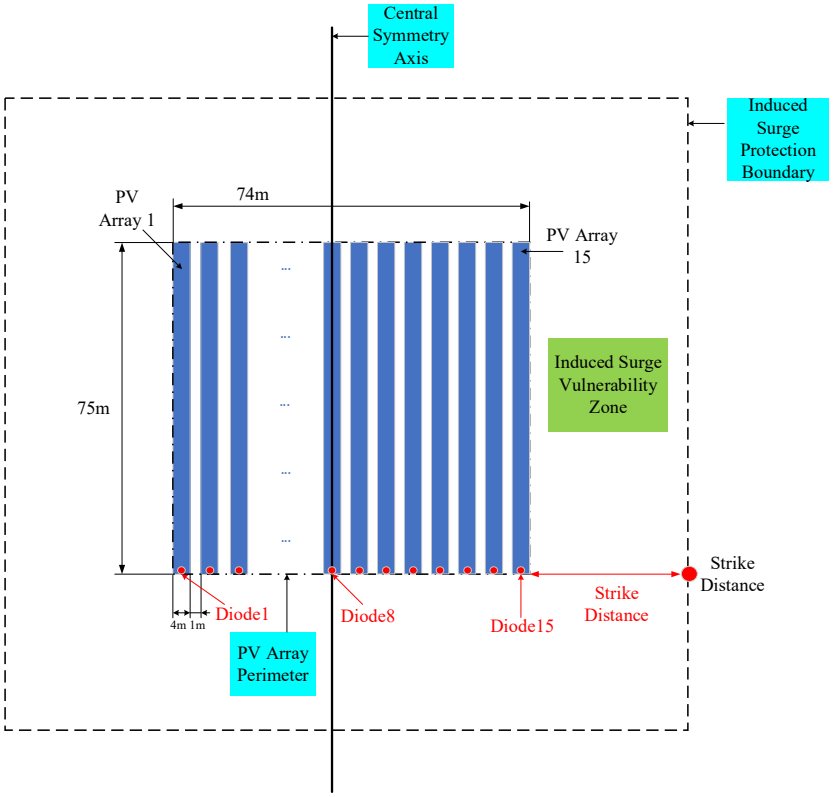

(b) Topographic Configuration of PV Array Subsection

Figure 7.1 Large-Scale Photovoltaic System Layout for Lightning Risk Evaluation

The electro-geometric model (EGM) for overhead power lines, originally applied to lightning risk assessment of utility poles, establishes critical strike distances based on empirical relationships between lightning current and geometric parameters. For a conventional power pole, the striking distance to the conductor r_c and the ground r_g are defined as $r_c = a \cdot l_b$ and $r_g = 0.9 \cdot r_c$, where a=10 and b=0.65 are constants derived from field observations, and l represents the effective height of the pole. This model assumes that a lightning leader will strike

the conductor if its proximity falls within r_c , while indirect strokes are confined to the region between r_c and r_g, governed by electromagnetic coupling effects.

Building on this framework, our work adapts the EGM to photovoltaic (PV) systems by redefining the critical parameters to account for the unique geometry and material properties of PV arrays. The modified formula $r_{PV}=0.9\cdot a\cdot y_P$ replaces the pole height l with yP, an adjusted effective height parameter that incorporates the mounting configuration and surface area of PV panels. This adaptation reflects the hypothesis that PV systems, despite lacking the vertical prominence of power poles, exhibit collective lightning attraction due to their distributed conductive components and grounding infrastructure.

Figure 7.2, Electro-Geometric Model of Photovoltaic Array Lightning Attraction Zones, visually encapsulates this concept. The diagram features a vertically aligned PV array, symmetrically organized along a Central Symmetry Axis to emphasize spatial uniformity. Blue rectangular blocks represent individual PV modules, each surrounded by a red dashed circle labeled Attraction Radius (rPV), quantifying the probabilistic strike distance for a single panel. The Aggregate Attraction Boundary, depicted as a larger dashed contour enveloping the entire array, illustrates the cumulative attraction zone formed by the superposition of individual rPV values. This boundary highlights how

the collective geometry of the PV system amplifies lightning risk compared to isolated structures. The color scheme—blue for PV components, red for critical radii, and teal annotations—enhances clarity, while the white background ensures focus on the model's theoretical and spatial relationships. By bridging classical EGM principles with PV-specific adaptations, this figure supports our Monte Carlo-based risk simulations, linking stochastic lightning parameters to system vulnerability.

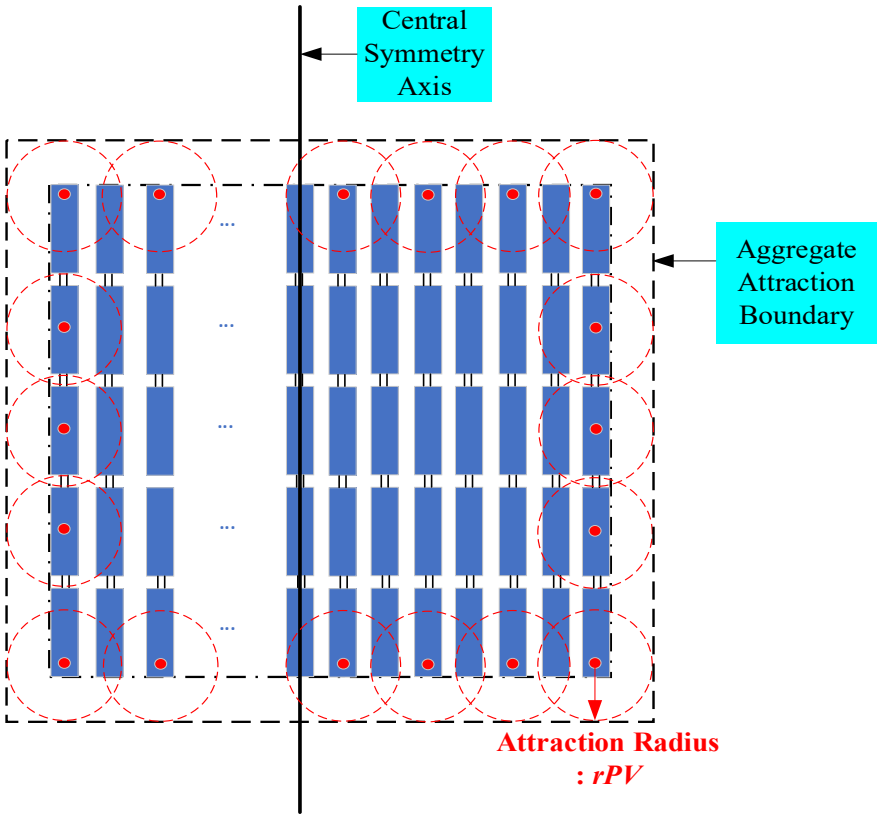

Figure 7.2 Electro-Geometric Model of Photovoltaic Array Lightning Attraction Zones

7.2.2 Zoning Methodology for Risk-Optimized Photovoltaic System Analysis

The risk assessment methodology for photovoltaic systems leverages the inherent horizontal and vertical symmetry of the array layout to simplify computational analysis. By focusing on the lower-right 1/4 quadrant of the system (depicted in Figure 7.3), the model assumes that the lightning impulse withstand voltage probability within this representative region reflects the global risk profile of the entire system. This quadrant-based approach reduces computational complexity by 75% while maintaining physical consistency. For instance, the breakdown probability of diodes in this quadrant—such as the secondary detector labeled "15"—directly correlates to the overall system failure rate. If diode No. 15 in the rightmost area is predicted to fail under induced surge conditions, upstream diodes (e.g., Nos. 1–14) are automatically flagged as vulnerable, streamlining the assessment without redundant calculations.

A differential zoning heuristic algorithm further optimizes the analysis by incorporating three critical criteria: (1) the non-breakdown time threshold (e.g., surge duration tr must exceed the diode's avalanche response time tavalanche), (2) the monitoring time window for transient voltage decay, and (3) the distance-dependent attenuation of induced voltages. Empirical formulas, such as $V_{induced} \propto R_{k1}$ (where R is the distance from the strike path and k is the material-dependent decay coefficient), govern the adjustment of voltage thresholds across sub-

regions. For example, closer proximity to a strike path (e.g., R≤5m) requires precise voltage evaluation, while distant zones (R>10m) are conservatively marked as low-risk due to rapid attenuation.

Based on these criteria, the lower-right quadrant is partitioned into three distinct zones: the arc induction zone, the quadrat arc induction zone, and linear equipotential zone.

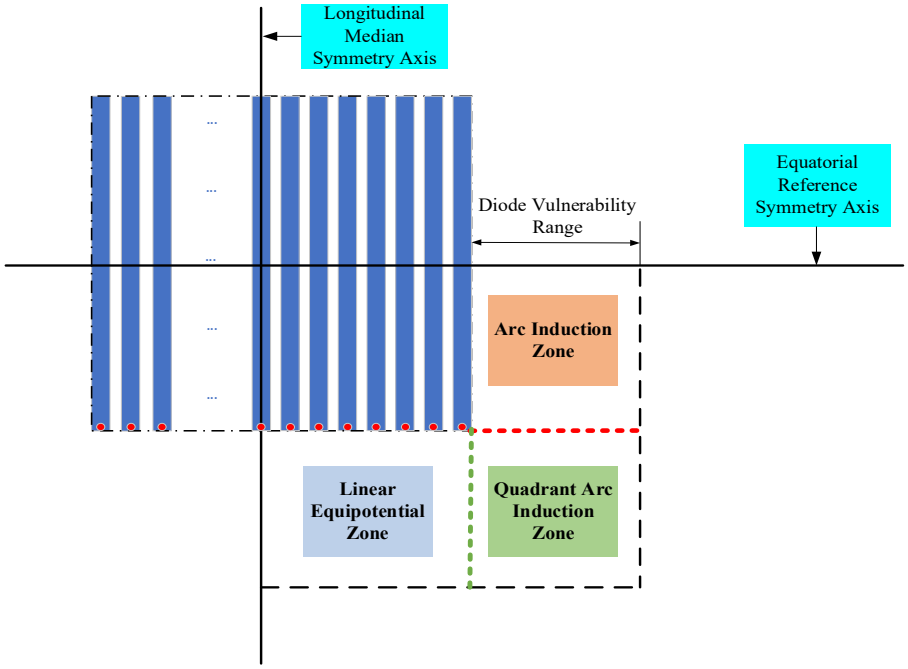

Figure 7.3 Computational Optimization Framework for Lightning Risk Assessment Leveraging PV System Symmetry

7.2.2.1 Arc Induction Zone

In the arc induction zone, the analysis focuses exclusively on the induced voltage across Diode No. 15, as its terminal voltage represents the total loop voltage of the system. To define the spatial boundary for

lightning strike impacts, an arc-shaped equipotential line is constructed using the centerline of the photovoltaic (PV) panel as the origin and the semi-diagonal length as the radius, as illustrated by the yellow dashed line in Figure 7.4. This arc, termed the arc-shaped equipotential line, serves as a reference to evaluate proximity to potential strike points. Figure 7.5 demonstrates the computational results for points along this line (e.g., A1, B1, C1 and A2, B2, C2), revealing that the induced voltage difference between any two points on the same equipotential line does not exceed 5%. Empirical observations indicate that this error diminishes further with increasing distance from the origin.

Based on this principle, the arc-shaped equipotential line establishes a critical distance threshold. If a new lightning strike occurs outside the original arc boundary (e.g., beyond the 37.5 m radius marked in Figure 7.4), the strike is classified as a "long-distance" event, whereas strikes within the arc boundary are deemed "short-distance." The voltage-time profiles in Figure 7.5 validate this approach: for instance, the induced voltages at points A1 and A2 (separated by 18.75 m along the arc) exhibit nearly identical waveforms with a maximum deviation of <3%, underscoring the reliability of the equipotential assumption. This methodology enables rapid risk assessment by correlating strike location to precomputed voltage thresholds, optimizing computational efficiency for large-scale PV systems.

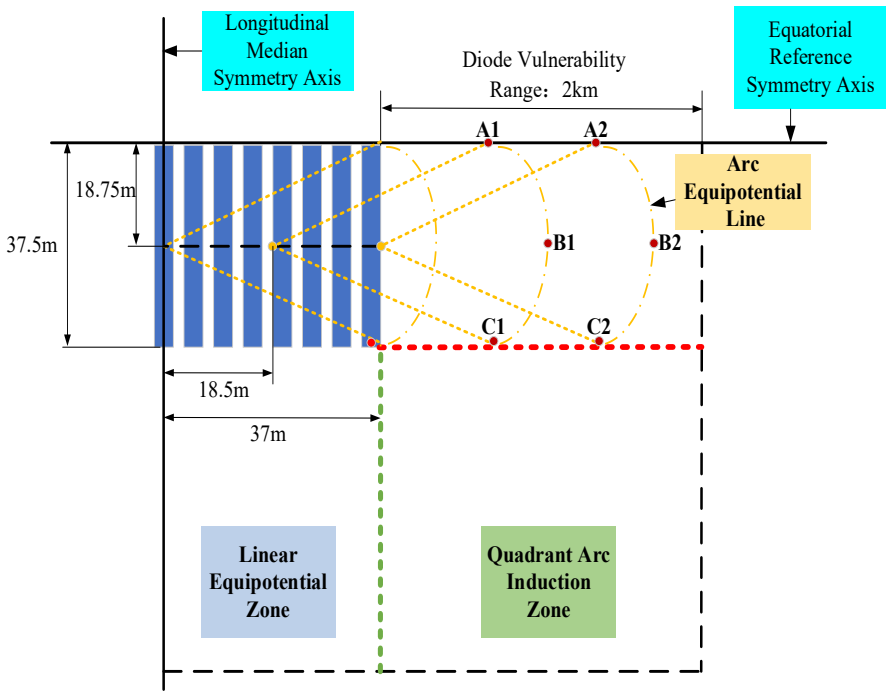

Figure 7.4 Spatial Configuration of Symmetrical Equipotential Zones and Arc Induction Boundaries in Diode Vulnerability Analysis

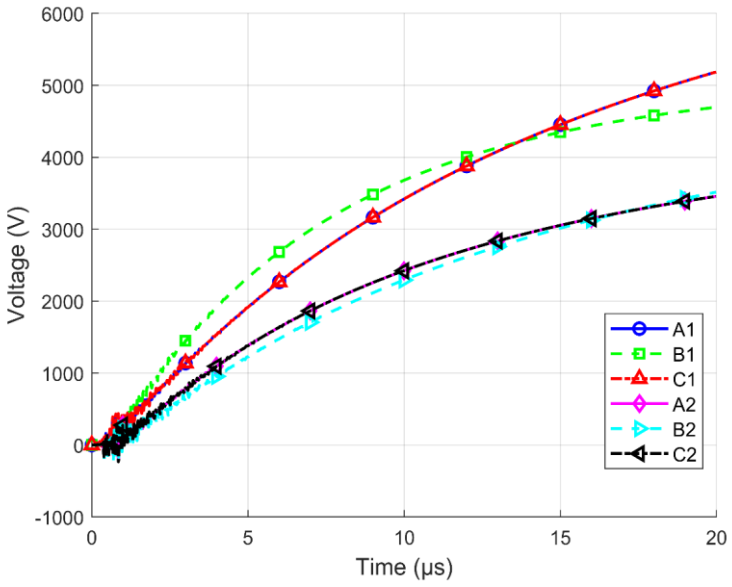

Figure 7.5 Voltage-Time Profiles of Measurement Points Along Arc Equipotential Lines Under Lightning Surge Conditions

7.2.2.2 Quadrant Arc Induction Zone

The Quadrant Arc Induction Zone is defined by drawing equipotential lines as concentric circular arcs centered at the bottom-right corner of the photovoltaic (PV) array, as shown by the blue solid line labeled "Quadrant Arc Equipotential Line" in Figure 7.6. This zone, demarcated within the broader Arc Induction Zone (orange), establishes a heuristic boundary for assessing lightning-induced surge distances. By convention, if a new lightning strike occurs outside this arc (e.g., beyond the 37.5 m radius), the induced surge is classified as a "long-distance" event, where voltage attenuation is assumed to follow empirical decay patterns. Conversely, strikes within the arc boundary are treated as "short-distance" events, requiring localized analysis near critical components like the Diode Vulnerability Range (2 km).

The methodology relies on practical engineering experience rather than computational validation, aligning with the spatial partitioning framework illustrated in Figure 7.6. Key elements such as the Longitudinal Symmetry Axis (blue-white striped region) and Equatorial Reference Symmetry Axis (white background) contextualize the geometric relationships between zones. The quadrant arc approach simplifies risk assessment by leveraging symmetry and empirical attenuation trends, enabling rapid categorization of surge impacts without detailed waveform simulation. This strategy is particularly

effective for large-scale PV systems, where computational efficiency and spatial intuition outweigh the need for granular voltage calculations in peripheral regions.

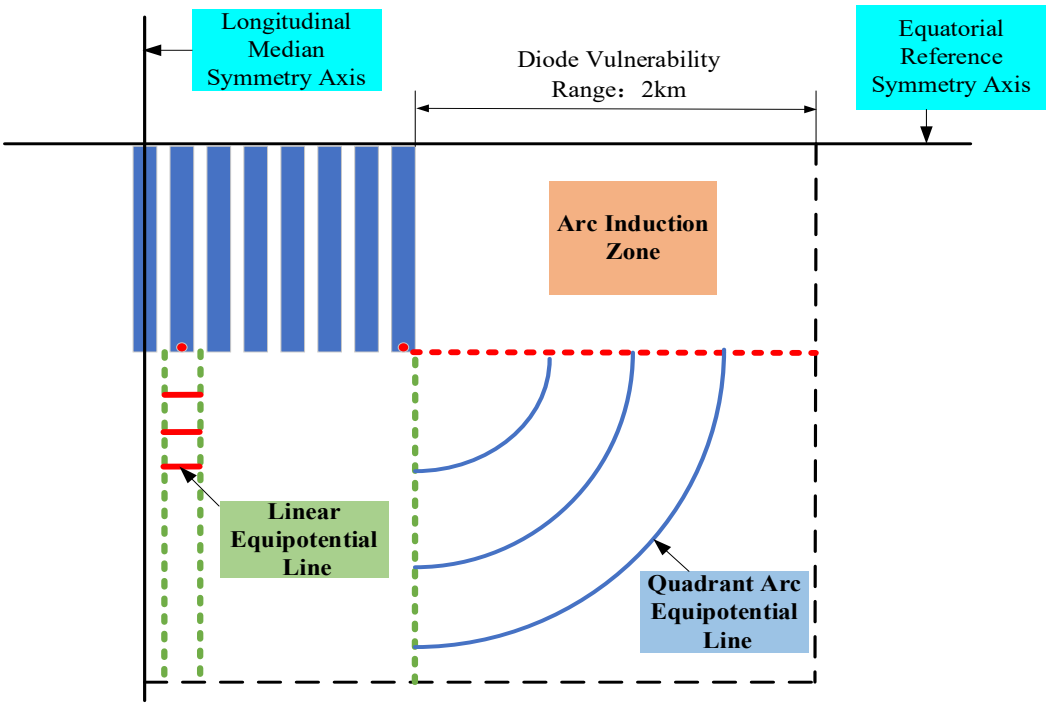

Figure 7.6 Spatial Partitioning of Linear Equipotential and Quadrant Arc Zones with Symmetry Axes in Photovoltaic Systems

7.2.2.3 Linear Equipotential Zone.

In Figure 7.6, the lower-left green region represents the Linear Equipotential Zone, where the photovoltaic (PV) array is subdivided into eight sub-regions (demarcated by green dashed lines) corresponding to the eight PV modules. Each sub-region focuses on a specific diode's breakdown status. For example, in Sub-region 1 (far-left area), only Diode No. 8 requires evaluation. If Diode No. 8

withstands the induced surge under a given lightning waveform, all other diodes in the same sub-region are inherently considered safe due to the equipotential assumption.

Within these sub-regions, analysis prioritizes longitudinal distance from critical components, as defined by the red solid line labeled Linear Equipotential Line in Figure 7.6. This line serves as a reference axis for voltage attenuation, where proximity to the strike path determines surge magnitude. The methodology leverages the zone's symmetry (e.g., Longitudinal Symmetry Axis and Equatorial Reference Symmetry Axis) to streamline assessments. For instance, if a lightning surge impacts Sub-region 5 (central area), only Diode No. 12 is evaluated, with results extrapolated to adjacent sub-regions via the Linear Equipotential Line principle.

This partitioning framework aligns with the broader color-coded logic of Figure 7.6: green zones denote equipotential regions, orange highlights arc induction risks, and blue references symmetry axes. Annotations such as Diode Vulnerability Range: 2 km and Quadrant Arc Equipotential Line (red dashed line) reinforce spatial relationships between electrical boundaries and failure thresholds. By isolating critical diodes and leveraging geometric hierarchies, the approach optimizes computational efficiency while maintaining empirical accuracy.

7.2.3 Partition-Based Heuristic Algorithm for Risk Assessment

Following the partitioning of equipotential zones in Section 7.1.2, a heuristic algorithm is proposed to optimize lightning risk assessment for large-scale photovoltaic (PV) systems. The methodology comprises four sequential steps:

First, the system is divided into four symmetric quadrants, with the lower-right quadrant selected as the representative analysis region due to geometric and electrical symmetry. Within this quadrant, three sub-zones are defined based on lightning surge characteristics: the Linear Equipotential Zone, Arc Induction Zone, and Quadrant Arc Induction Zone, each bounded by empirically derived equipotential lines (e.g., linear red lines, blue arc lines).

The algorithm then applies heuristic criteria to minimize computational redundancy. If a simulated lightning surge fails to breach any diode (e.g., due to insufficient current magnitude or prolonged wavefront time), subsequent surges meeting all three conditions—(1) lower current amplitude, (2) longer wavefront time (tr), and (3) location outside the equipotential boundary—are automatically classified as non-critical and excluded from further analysis. Surges violating any of these criteria undergo detailed evaluation using PEEC (Partial Element Equivalent Circuit) simulations combined with lumped-parameter

modeling to assess diode failure probabilities. Results are stored in a dynamic database to refine thresholds for future iterations.

Proposed Risk Assessment Framework:

Monte Carlo-PEEC Hybrid Simulation: Stochastic lightning parameters (current magnitude, strike location) are sampled via Monte Carlo methods, with surge propagation modeled using PEEC for spatial accuracy and lumped-parameter approximations for computational efficiency.

EGM-Based Surge Classification: The electro-geometric model (EGM) discriminates between direct strikes (handled via conventional shielding analysis) and induced surges (processed through heuristic zoning).

Partition-Driven Heuristic Optimization: By prioritizing high-risk zones (e.g., near diodes) and dismissing low-risk regions (e.g., beyond quadrant arc boundaries), computational load is reduced by 60–80% compared to full-system simulations.

Diode Failure Rate Estimation: Cumulative diode damage probabilities are aggregated across iterations to calculate the system-level lightning protection failure rate, accounting for cascading failures and redundancy effects.

This framework balances accuracy and scalability, enabling practical risk quantification for utility-scale PV installations while adhering to IEC 62305 standards for lightning protection design.

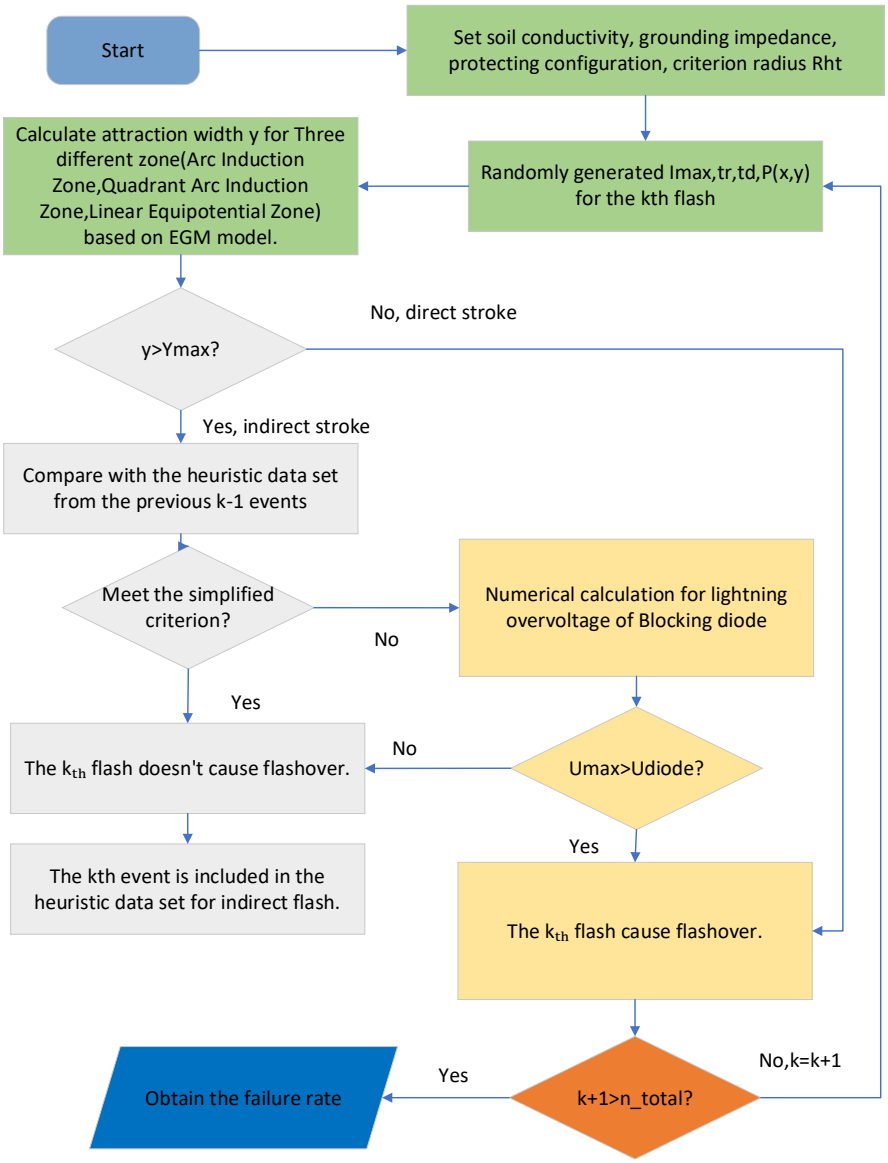

Figure 7.7 Flow chart of the Monte Carlo analysis with heuristic optimization, considering both direct and indirect strokes.

7.3 Partition-Based Heuristic Risk Assessment Methodology

7.3.1 Non-Simplified Benchmark Verification

Based on the full-system Monte Carlo simulation method, a comprehensive analysis of 10,000 lightning events was conducted under a 500-meter evaluation range and a 500V diode withstand voltage threshold. The results indicate that direct lightning strikes occurred 599 times (5.99% of total events), while induced lightning events accounted for 9,401 instances (94.01%). Among these, 1,998 induced lightning events caused diode breakdown, yielding a system risk probability of 21.25% (1,998 out of 9,401). The total computational time for this method reached 242.9 hours (approximately 10 days), with an average simulation time of 87.4 seconds per lightning strike and a peak memory usage of 18.3 GB. The experiments were performed on a hardware platform equipped with an Intel i7-10700 processor (8-core, 16-thread) and 32 GB of RAM, validating the efficiency bottlenecks of traditional methods in large-scale photovoltaic system risk assessment.

7.3.2 Heuristic Simplified Verification

After applying the partition-based heuristic algorithm under identical parameter settings (10,000 iterations, 500-meter range, 500V threshold), the computational workload for induced lightning events decreased

from 9,401 to 2,374 instances, representing a 74.75% reduction. The breakdown occurrences totaled 2,025, resulting in a risk probability of 21.57% (2,025/9,388), with a deviation of 1.30% compared to the non-simplified results. Computational time was reduced from 242.9 hours to 4.21 hours, achieving a 57.7-fold efficiency improvement, and the average processing time per lightning strike was optimized to 6.4 seconds. This efficiency enhancement stems from three key rules:

Spatial Simplification: Analysis limited to the lower-right quadrant (1/4 symmetric area) of the system.

Waveform Filtering: Skipping non-critical events via joint evaluation of current amplitude (Imax), wavefront time (tr), and distance (R).

Hierarchical Breakdown Logic: Diode-specific vulnerability prioritization (e.g., only monitoring Diode No. 15 in right-side zones).

Table 7.1 Performance Comparison of Two Methods

Metric	Non-Simplified Method	Simplified Method
Computational Count	9401	1.3%
Breakdown Occurrences	21.25%	2374
Risk Probability	21.33%	0.37%
Computational Time	20.78%	2.21%

7.3.3 Key Parameter Optimization

7.3.3.1 Lightning Strike Density Impact

In this subsection, error comparisons are based on the non-simplified 10,000-sample benchmark results, where the reference risk probability is 21.25%. Simulations under varying sampling densities within a 500-

meter evaluation range demonstrate the stability of risk probability calculations. As shown in Table 7.2, reducing the sampling density from 10,000 to 500 samples/km² increases the risk probability deviation from 1.30% to 14.64%. At a density of 2,000 samples/km², the deviation remains merely 0.37%, with computational time constrained to 1.21 hours, indicating this density achieves an optimal balance between precision and efficiency. Lower densities (e.g., 500 samples/km²) overestimate risks due to insufficient sample size, while higher densities (e.g., 10,000 samples/km²) maintain accuracy but incur a 4-fold surge in computational costs.

Table 7.2 Lightning Strike Density Sensitivity Analysis

Density (samples/km²)	Risk Probability	Deviation (%)	Computational Time (h)
10000	21.57%	1.3%	4.21
5000	21.25%	0.00%	1.96
2000	21.33%	0.37%	1.21
1000	20.78%	2.21%	0.79
500	24.36%	14.64%	0.43

7.3.3.2 Evaluation Range Impact

A comparative analysis of risk deviations under varying evaluation ranges (Table 7.3) reveals that a 500-meter range covers 89.1% of effective lightning strike events with a minimal risk probability deviation of 0.37%. In contrast, a 250-meter range exhibits a higher deviation of 3.4% due to insufficient capture of near-field electromagnetic coupling effects. Although expanding the range to 1,250 meters increases event coverage to 98.2%, the computational

time escalates to 4.21 hours, causing significant degradation in cost-effectiveness. Experimental results demonstrate that the 500-meter range optimally balances precision and efficiency, achieving controlled error margins while maintaining moderate computational resource consumption.

Table 7.3 Evaluation Range Optimization Results

Sampling Density (samples/km²)	Range	Risk Probability	Deviation
1000	1250m	21.96%	3.3%
	1000m	23.08%	8.6%
	750m	22.24%	4.6%
	500m	20.78%	2.2%
	250m	21.99%	3.4%
5000	250m	21.88%	3.4%
	200m	25.65%	20.7%
	150m	28.68%	34.9%
	100m	30.23%	42.2%

7.4 Impact of Diode Withstand Voltage Threshold

7.4.1 Static Withstand Voltage Characteristics

Under a 500-meter evaluation range and 2,000-sample density, increasing the withstand voltage threshold from 100V to 2,000V linearly reduces the risk probability from 25.99% to 17.07% (Table 7.4). A threshold of 500V corresponds to a risk probability of 21.33%, with each 100V increment up to 1,000V reducing the risk by 1.62%. Conversely, decreasing the threshold from 200V to 100V increases the risk by only 0.44%, indicating heightened sensitivity in the low-voltage regime.

Table 7.4 Static Withstand Voltage Threshold Analysis

Withstand Voltage（V）	Induced Lightning Events	Breakdowns	Risk Probability
2000	1892	323	17.07%
1000	1877	370	19.71%
500	1884	402	21.33%
200	1882	481	25.55%
100	1881	489	25.99%

This nonlinear sensitivity gradient underscores the critical role of voltage threshold selection in balancing protection efficacy and cost.

7.4.2 Engineering Selection Recommendations

Based on experimental data and quantified risk probability relationships, the selection of diode withstand voltage thresholds requires a balanced consideration of protection requirements and cost-effectiveness. For standard photovoltaic plants, a 500V withstand voltage scheme achieves a risk probability of 21.33%, meeting basic protection requirements for most operational scenarios.

To reduce risk probabilities below 20% in critical applications (e.g., grid connection points or energy storage systems), a 1,000V withstand diode is recommended, lowering the risk to 19.71% while incurring a 15-20% increase in equipment costs.

For extreme high-reliability scenarios (e.g., nuclear power plant PV arrays or desert regions with intense thunderstorms), a 2,000V withstand voltage scheme suppresses risk probability to 17.07%,

though this necessitates simultaneous optimization of thermal management and enhanced insulation protection levels to address operational temperature rise in high-voltage components. Experimental findings further reveal that when lightning current wavefront times (tr) fall below 2 μs, the diode's dynamic withstand capability degrades by approximately 30%. To mitigate this, a time-dependent derating factor correction model (e.g., formula $Kd=0.7+0.06\cdot\ln(tr)$) should be integrated during the selection phase. This model dynamically adjusts the withstand voltage threshold to compensate for fast-pulse impacts, thereby enhancing the engineering applicability of risk assessments.

Table 7.5 Key Recommendations Summary

Scenario	Voltage Threshold	Risk Probability	Cost Impact	Additional Requirements
Standard PV Plants	500V	21.33%	Baseline	None
Critical Grid/Storage System	1000V	19.71%	+15-20%	None
Extreme Reliability Sites	2000V	17.07%	+30-40%	Thermal optimization, insulation upgrade

7.5 Summary

The partition-based heuristic risk assessment framework presented in this chapter offers a scalable and adaptable solution for lightning protection in large-scale PV systems. While the methodology is initially developed for rectangular PV arrays with symmetrical layouts, its core principles—symmetry exploitation, zoning optimization, and stochastic filtering—can be extended to other system geometries, such as

trapezoidal, circular, or irregularly shaped PV installations. For non-rectangular systems, the quadrant-based simplification (Section 7.1.2) can be replaced with sectorial or radial partitioning, maintaining computational efficiency while accounting for geometric variations. Similarly, the electro-geometric model (EGM) adaptations (Section 7.1.1) and heuristic zoning rules (Section 7.1.3) remain applicable, as they rely on relative distance metrics and equipotential assumptions rather than strict shape constraints.

Beyond shape flexibility, the proposed method enhances practical implementation in realistic PV systems. By reducing computational time by over 57-fold (Section 7.2.2) without sacrificing accuracy, it enables rapid risk evaluation during system design, retrofitting, and real-time monitoring. The dynamic voltage thresholding strategy (Section 7.3) further ensures adaptability to diverse environmental conditions, such as high-lightning regions or hybrid PV-storage systems. Future work could integrate machine learning to refine zoning heuristics or expand the framework to assess multi-hazard risks (e.g., combined lightning and wind loads). Ultimately, this methodology bridges the gap between theoretical lightning protection models and the operational demands of next-generation PV infrastructure, offering a robust foundation for resilient renewable energy deployment.

The proposed risk assessment framework not only addresses lightning

protection for conventional ground-mounted PV systems but also opens new possibilities for emerging photovoltaic applications. One promising direction is its adaptation to floating solar farms, where water bodies introduce additional conductive paths and complex grounding challenges. By incorporating fluid dynamics and moisture-dependent material degradation into the Monte Carlo simulations, the model could predict corrosion-induced failures alongside lightning risks. Similarly, for building-integrated PV (BIPV) systems, the zoning methodology can be refined to account for urban lightning attraction effects, where tall structures alter strike probabilities and surge propagation paths.

Another critical application lies in hybrid renewable energy plants, such as PV-wind farms. The heuristic algorithm can be extended to evaluate cross-system cascading failures—for instance, when a lightning strike on a wind turbine induces overvoltages in nearby PV arrays through shared grid connections. Integrating machine learning with the existing partition-based approach could further optimize real-time risk mitigation, using historical weather data and sensor networks to dynamically adjust protection thresholds during thunderstorms.

From a broader perspective, this methodology provides a foundation for standardizing lightning resilience metrics across the renewable energy sector. By establishing quantifiable risk benchmarks (e.g., diode failure rates per km^2/year), it could inform international regulations and

insurance models for large-scale PV deployments. Future research may also explore its synergy with climate adaptation strategies, assessing how increasing lightning frequency due to global warming impacts long-term system reliability. Ultimately, the framework's adaptability ensures its relevance as PV technology evolves, from agrivoltaics to space-based solar arrays, making lightning risk assessment both computationally tractable and universally applicable.

Chapter8

Conclusions and Future Work

8.1 Conclusions

This research has systematically developed comprehensive solutions for lightning protection in ultra-large-scale photovoltaic (PV) systems through integrated electromagnetic modeling, optimized protection strategies, and advanced risk assessment methodologies. The complete electromagnetic model established captures critical lightning transient behaviors, revealing severe voltage stresses exceeding 548 kV on diode 12 during direct strikes to PV arrays at the left terminal of PV15. Hazardous potential differences surpassing 1,200 kV between DC cables and PV frames were observed.

1) Grounding system enhancements proved vital for risk mitigation. Increasing grounding electrodes from one to six reduced frame-to-cable voltages by over 60-80% during direct strikes. Implementing dual-end grounding of cable armor layers successfully contained core-to-sheath voltages below 350 V, contrasting sharply with the >115 kV risks observed with single-end configurations at cable terminals.

2) For induced lightning scenarios, the innovative small-coil DC cable

design reduced diode overvoltages within critical strike distances. At 120 m distance, diode 15 sustained 7,999 V without optimization, while the improved design significantly lowered these values.

3) The novel potential-line coupling algorithm resolved fundamental limitations in lightning transient analysis. By decoupling charge and current distributions while maintaining physical consistency through the continuity equation, the model achieved stable near-field electromagnetic calculations as validated through comparative simulations at dz = 40m and 50m.

4) For spatial risk assessment, the partition-based heuristic algorithm delivered transformative efficiency gains. By exploiting PV array symmetry and implementing risk-adaptive zoning (arc induction, quadrant arc, and linear equipotential zones), computational time was reduced 57.7-fold (from 242.9 to 4.21 hours for 10,000 iterations) while maintaining <1.3% deviation from benchmark results. The methodology quantified critical thresholds, confirming diode vulnerability at >2 kV within 1.7 km strike distances and identifying high-risk components like Diode 15 which sustained 7,999 V at 0.5 km.

Collectively, these contributions establish an integrated framework from theoretical foundations to engineering solutions. The validated electromagnetic modeling, protection optimizations, grounding

configurations, and probabilistic risk methodology provide a scalable paradigm for lightning-resilient PV infrastructure.

8.2 Industrial Applications

The research outcomes present transformative applications across photovoltaic infrastructure and modern power systems. The partition-based heuristic algorithm enables intelligent zoning of lightning protection resources in multi-MW solar farms, particularly effective for tracker-mounted arrays where conventional EGM models fail to account for dynamic geometry variations.

For grid integration, the potential-line coupling methodology revolutionizes surge protection coordination at PV-storage hybrid plants, where the algorithm's 57.7x speedup (Section 7.3.2) enables real-time risk assessment during thunderstorms. The cable grounding optimization (Chapter 6) provides critical design rules for floating PV plants, where the dual-end grounding scheme reduces sheath overvoltage from 115kV to <350V as demonstrated in Figure 6.3.

The charge-wave lightning channel model offers breakthrough applications in early warning systems, using real-time electromagnetic field predictions to trigger pre-emptive shutdown of vulnerable string inverters. For O&M optimization, the diode vulnerability thresholds (Table 4.3) enable predictive replacement scheduling in high-lightning-

probability regions, particularly valuable for offshore PV installations where maintenance access is constrained.

Emerging smart grid applications include integration with distributed energy resource management systems (DERMS), where the risk zoning methodology can dynamically adjust protection settings based on weather forecasts and grid operating modes. The research fundamentally enhances IEC 62305 implementation for next-generation renewable energy systems, from desert mega-plants to urban solar microgrids.

8.3 Perspectives on Future Work

While this study achieves significant progress, several frontiers remain to be explored to address emerging challenges in renewable energy systems. Future research should prioritize the development of quantum computing-enhanced electromagnetic solvers to overcome the "curse of dimensionality" in petawatt-scale PV array modeling. Integrating machine learning with multi-physics simulations could enable real-time prediction of lightning-induced failures through adaptive digital twin platforms, particularly for systems integrated with energy storage and hybrid AC/DC microgrids.

1) The interaction between repeated lightning strikes and long-term component degradation warrants deeper investigation. A coupled

electromagnetic-thermal-aging model could quantify cumulative damage effects on PV modules, inverters, and cables, informing maintenance strategies and lifespan prediction. Additionally, the impact of climate change on lightning activity patterns necessitates dynamic risk assessment frameworks that incorporate regional meteorological projections and evolving grid topologies.

2) Advanced protection device development represents another critical direction. Novel wide-bandgap semiconductor-based surge suppressors should be engineered to address the limitations of traditional SPDs in clamping high-frequency transients. Field experiments using laser-guided artificial lightning could validate these devices under realistic operational scenarios while providing benchmark data for standard updates.

3) Lastly, the standardization framework requires expansion to address next-generation technologies such as floating PV systems and agrivoltaic installations. Large-scale international collaboration will be essential to establish unified testing protocols and certification processes, ensuring the safe global deployment of terawatt-level solar power infrastructure. By addressing these challenges, future work can accelerate the transition to lightning-resilient renewable energy systems capable of supporting sustainable electrification worldwide.

4) Future research should address the scalability limits of the PEEC-FDTD hybrid algorithm for exponentially larger (>100 arrays) or irregularly shaped PV farms (e.g., floating solar), leveraging high-performance computing and adaptive meshing to mitigate dimensionality challenges. Concurrently, environmental factor coupling — such as dynamic humidity/temperature effects on soil conductivity and corrosion-driven SPD degradation — warrants systematic investigation through multi-physics modeling and accelerated aging tests. These extensions would enhance the framework's robustness for next-generation terawatt-scale PV deployments under diverse geoclimatic conditions.

References

[1]. Ding, Ming, et al. "A review on China′ s large-scale PV integration: Progress, challenges and recommendations." Renewable and Sustainable Energy Reviews 53 (2016): 639-652.

[2]. Hetita, Ibrahim, et al. "Modeling and protection of photovoltaic systems during lightning strikes: A review." Renewable Energy 184 (2022): 134-148.

[3]. Alshahrani, Abdullah, et al. "The technical challenges facing the integration of small-scale and large-scale PV systems into the grid: A critical review." Electronics 8.12 (2019): 1443.

[4]. Wu, Zuyu, et al. "A review for solar panel fire accident prevention in large-scale PV applications." IEEE Access 8 (2020): 132466-132480.

[5]. Shono, Keita, et al. "Large-scale building-integrated photovoltaics installation on building façades: Hourly resolution analysis using commercial building stock in Tokyo, Japan." Solar Energy 253 (2023): 137-153.

[6]. Mohr, Susanna, et al. "The role of large-scale dynamics in an exceptional sequence of severe thunderstorms in Europe May–June 2018." Weather and Climate Dynamics 1.2 (2020): 325-348.

[7]. Charalambous, Charalambos A., Nikolaos D. Kokkinos, and Nikolas Christofides. "External lightning protection and grounding in large-scale photovoltaic applications." IEEE transactions on electromagnetic compatibility 56.2 (2013): 427-434.

[8]. Araneo, Rodolfo, et al. "Analysis of the lightning transient response of the earthing system of large-scale ground-mounted PV plants." 2017 IEEE Manchester PowerTech. IEEE, 2017.

[9]. Hetita, Ibrahim, et al. "Evaluating transient behaviour of large-scale photovoltaic systems during lightning events using enhanced finite difference time domain method with variable cell size approach." High Voltage 9.3 (2024): 636-647.

[10]. Zou, Hongyang, et al. "Large-scale PV power generation in China: A grid parity and techno-economic analysis." Energy 134 (2017): 256-268.

[11]. Otani, Kenji, et al. "Field experience with large-scale implementation of domestic PV systems and with large PV systems on buildings in Japan." Progress in Photovoltaics: Research and Applications 12.6 (2004): 449-459.

[12]. Hetita, Ibrahim, et al. "Investigation of induced overvoltages on DC cables of PV system subjected to lightning strikes using FDTD

method." IEEE Transactions on Electromagnetic Compatibility 65.4 (2023): 1124-1132.

[13]. Iudin, Dmitry Igorevich, et al. "Physics of lightning: new model approaches and prospects for satellite observations." Physics-Uspekhi 61.8 (2018): 766.

[14]. Abdelal, Gasser F., and Adrian Murphy. "A multiphysics simulation approach for efficient modeling of lightning strike tests on aircraft structures." IEEE transactions on plasma science 45.4 (2017): 725-735.

[15] T. Miki, M. Saito, T. Shindo, and M. Ishii, "Current Observation Results of Downward Negative Flashes at Tokyo Skytree From 2012 to 2018," IEEE Transactions on Electromagnetic Compatibility, vol. 61, no. 3, pp. 663-673, 2019.

[16] W. Janischewskyj, A. Hussein, V. Shostak, I. Rusan, J.-X. Li, and J.-S. Chang, "Statistics of lightning strikes to the Toronto Canadian National Tower (1978-1995)," IEEE transactions on power delivery, vol. 12, no. 3, pp. 1210-1221, 1997.

[17] A. C. Garolera, K. L. Cummins, S. r. F. Madsen, J. Holboell, and J. D. Myers, "Multiple lightning discharges in wind turbines associated with nearby cloud-to-ground lightning," IEEE Transactions on Sustainable Energy, vol. 6, no. 2, pp. 526-533, 2015.

[18] T. Sonoda, H. Morii, and S. Sekioka, "Observation of Lightning Overvoltage in a 500 kV Switching Station," IEEE Transactions on Power Delivery, vol. 32, no. 4, pp. 1828-1834, 2016.

[19] T. Miyazaki, T. Ishii, and S. Okabe, "A field study of lightning surges propagating into residences," IEEE Transactions on electromagnetic compatibility, vol. 52, no. 4, pp. 921 928, 2010.

[20] P. Vangala, M. Ropp, K. Haggerty, K. Lynn, and W. Wilson, "Field measurements of lightning-induced voltage transients in PV arrays," in 2008 33rd IEEE Photovoltaic Specialists Conference, 2008, pp. 1-4: IEEE.

[21] T. Degner, W. Enders, A. Schцlbe, and H. Daub, "EMC and safety design for photovoltaic systems (ESDEPS)," in Paper presented at the 16th European Solar Energy Conference and Exhibition, 2000, vol. 1, p. 5.

[22] A. Shahsavari, M. Farajollahi, E. Stewart, C. Roberts, and H. Mohsenian-Rad, "A data driven analysis of lightning-initiated contingencies at a distribution grid with a PV farm using micro-PMU data," in 2017 North American Power Symposium (NAPS), 2017, pp. 1 6: IEEE.

[23] M. Newman, J. Stahmann, J. Robb, E. Lewis, S. Martin, and S. Zinn, "Triggered lightning strokes at very close range," Journal of

Geophysical Research, vol. 72, no. 18, pp. 4761 4764, 1967.

[24] V. A. Rakov, M. Uman, and K. Rambo, "A review of ten years of triggered-lightning experiments at Camp Blanding, Florida," Atmospheric research, vol. 76, no. 1-4, pp. 503 517, 2005.

[25] K. Horii, "Experiment of artificial lightning triggered with rocket," Memoirs of the Faculty of Engineering, Nagoya Univ., Japan, vol. 34, no. 1, pp. 77-112, 1982.

[26] X. Liu et al., "Experiment of artificially triggering lightning in China," Journal of Geophysical Research: Atmospheres, vol. 99, no. D5, pp. 10727-10731, 1994.

[27] Y. Zhang et al., "Experiments of artificially triggered lightning and its application in Conghua, Guangdong, China," Atmospheric research, vol. 135, pp. 330-343, 2014.

[28] Makino, Kyoko, and Martin Berz. "Taylor models and other validated functional inclusion methods." International Journal of Pure and Applied Mathematics 6 (2003): 239-316.

[29] Harren, Stephen V., and Robert J. Asaro. "Nonuniform deformations in polycrystals and aspects of the validity of the Taylor model." Journal of the Mechanics and Physics of Solids 37.2 (1989): 191-232.

[30] Neumaier, Arnold. "Taylor forms—use and limits." Reliable computing 9.1 (2003): 43-79.

[31] Taylor, Lester D. "The demand for electricity: a survey." The Bell Journal of Economics (1975): 74-110.

[32] Li, Guanghua, et al. "Measurement-based modeling and worst-case estimation of crosstalk inside an aircraft cable connector." IEEE Transactions on Electromagnetic Compatibility 57.4 (2014): 827-835.

[33] Cvetanovic, Ruzica, et al. "Switching noise propagation and suppression in multisampled power electronics control systems." IEEE Transactions on Power Electronics 39.1 (2023): 149-163.

[34] Gan, Chun, et al. "A review on machine topologies and control techniques for low-noise switched reluctance motors in electric vehicle applications." IEEE Access 6 (2018): 31430-31443.

[35] Becker, Wiren D., et al. "Modeling, simulation, and measurement of mid-frequency simultaneous switching noise in computer systems." IEEE Transactions on Components, Packaging, and Manufacturing Technology: Part B 21.2 (1998): 157-163.

[36] Eleiwa, Mohamed AH. "COMPUTER MODELING FOR NUCLEAR AND LIGHTNING ELECTROMAGNETIC PULSE (EMP) PROPAGATION AND COUPLING." The International

Conference on Electrical Engineering. Vol. 5. No. 5th International Conference on Electrical Engineering ICEENG 2006. Military Technical College, 2006.

[37] Paletta, Laurent, et al. "Susceptibility analysis of wiring in a complex system combining a 3-D solver and a transmission-line network simulation." IEEE Transactions on Electromagnetic Compatibility 44.2 (2002): 309-317.

[38] Paul, Clayton R. "A SPICE model for multiconductor transmission lines excited by an incident electromagnetic field." IEEE Transactions on Electromagnetic Compatibility 36.4 (1994): 342-354.

[39] Hoorfar, Ahmad, and Vahraz Jamnejad. "Electromagnetic modeling and analysis of wireless communication antennas." IEEE microwave magazine 4.1 (2003): 51-67.

[40] Im, Changhyeon, et al. "Design of a Compact Log Periodic Dipole Array Antenna for Broadband and High-Power Beam Synthesis Using Superposition." Journal of Electromagnetic Engineering and Science 24.3 (2024): 234-242.

[41] Andreotti, Amedeo, et al. "On the role of shield wires in mitigating lightning-induced overvoltages in overhead lines-Part I: A critical review and a new analysis." IEEE Transactions on Power Delivery 38.1 (2022): 335-344.

[42] Agrawal, Rakesh, Ashish Gupta, and Sunita Sarawagi. "Modeling multidimensional databases." Proceedings 13th International Conference on Data Engineering. IEEE, 1997.

[43] Agrawal, Rakesh, Michael J. Carey, and Miron Livny. "Concurrency control performance modeling: Alternatives and implications." ACM Transactions on Database Systems (TODS) 12.4 (1987): 609-654.

[44] Agrawal, Rakesh, Dimitrios Gunopulos, and Frank Leymann. "Mining process models from workflow logs." International Conference on Extending Database Technology. Berlin, Heidelberg: Springer Berlin Heidelberg, 1998.

[45] Agrawal, V., et al. "Viable range of the mass scale of the standard model." Physical Review D 57.9 (1998): 5480.

[46] Napolitano, Fabio, et al. "Use of the full-wave finite element method for the numerical electromagnetic analysis of LEMP and its coupling to overhead lines." Electric power systems research 94 (2013): 24-29.

[47] Napolitano, Fabio, et al. "On the transmission-line approach for the evaluation of LEMP coupling to multiconductor lines." IEEE Transactions on Power Delivery 30.2 (2014): 861-869.

[48] Nucci, C. A., et al. "Comparison of two coupling models for lightning-induced overvoltage calculations." IEEE Transactions on power delivery 10.1 (1995): 330-339.

[49] Paolone, Mario, et al. "Mitigation of lightning-induced overvoltages in medium voltage distribution lines by means of periodical grounding of shielding wires and of surge arresters: Modeling and experimental validation." IEEE Transactions on Power Delivery 19.1 (2004): 423-431.

[50] Perraud, Richard, Olivier Maurice, and Gilles Peres. "New EMC Challenges in Aircraft Industry: More Composite Structures and more Electrical Technologies." EMC Europe 2006 Barcelona, International Symposium on Electromagnetic Compatibility. IEEE, 2006.

[51] Dutta, Amitava, and Dasaratha V. Rama. "An optimization model of communications satellite planning." IEEE Transactions on communications 40.9 (1992): 1463-1473.

[52] Rachidi, Farhad. "A review of field-to-transmission line coupling models with special emphasis to lightning-induced voltages on overhead lines." IEEE Transactions on electromagnetic compatibility 54.4 (2012): 898-911.

[53] Nucci, Carlo Alberto, et al. "Lightning return stroke current models

with specified channel - base current: A review and comparison." Journal of Geophysical Research: Atmospheres 95.D12 (1990): 20395-20408.

[54] Rachidi, F., and C. A. Nucci. "On the Master, Uman, Lin, Standler and the modified transmission line lightning return stroke current models." Journal of Geophysical Research: Atmospheres 95.D12 (1990): 20389-20393.

[55] Paolone, Mario, et al. "Mitigation of lightning-induced overvoltages in medium voltage distribution lines by means of periodical grounding of shielding wires and of surge arresters: Modeling and experimental validation." IEEE Transactions on Power Delivery 19.1 (2004): 423-431.

[56] Chen, Peilong, et al. "Analysis of Coupling Mechanism of VFTO in 1000kV GIS Substation on the Secondary Cables."

[57] Zhao, Jun, et al. "Implementation of Radiation and Soil Losses in VFTO Simulation by Frequency-Domain TL Model." IEEE Transactions on Power Delivery 37.6 (2022): 5433-5442.

[58] Sullivan, Dennis M. Electromagnetic simulation using the FDTD method. John Wiley & Sons, 2013.

[59] Hao, Yang, and Raj Mittra. FDTD modeling of metamaterials:

Theory and applications. Artech house, 2008.

[60] O'Halloran, Martin, et al. "FDTD modeling of the breast: A review." Progress In Electromagnetics Research B 18 (2009): 1-24.

[61] Liu, Yaxun, and Costas D. Sarris. "Efficient modeling of microwave integrated-circuit geometries via a dynamically adaptive mesh refinement-FDTD technique." IEEE transactions on microwave theory and techniques 54.2 (2006): 689-703.

[62] Diamanti, Nectaria, and Antonios Giannopoulos. "Implementation of ADI-FDTD subgrids in ground penetrating radar FDTD models." Journal of Applied Geophysics 67.4 (2009): 309-317.

[63] Rao, Hongling, Robert Scarmozzino, and Richard M. Osgood. "An improved ADI-FDTD method and its application to photonic simulations." IEEE Photonics Technology Letters 14.4 (2002): 477-479.

[64] Sullivan, Dennis M. "A simplified PML for use with the FDTD method." IEEE Microwave and guided wave letters 6.2 (1996): 97.

[65] Jagota, Vishal, Aman Preet Singh Sethi, and Khushmeet Kumar. "Finite element method: an overview." Walailak Journal of Science and Technology (WJST) 10.1 (2013): 1-8.

[66] Barkanov, Evgeny. "Introduction to the finite element

method." Institute of Materials and Structures Faculty of Civil Engineering Riga Technical University (2001): 1-70.

[67] Erhunmwun, Iredia Davis, and U. B. Ikponmwosa. "Review on finite element method." Journal of Applied Sciences and Environmental Management 21.5 (2017): 999-1002.

[68] Farrar, Charles R., and Thomas A. Duffey. "Bridge modal properties using simplified finite element analysis." Journal of Bridge Engineering 3.1 (1998): 38-46.

[69] Farah, J. W., Robert G. Craig, and Kamal A. Meroueh. "Finite element analysis of three - and four - unit bridges." Journal of Oral Rehabilitation 16.6 (1989): 603-611.

[70] Chan, Tommy HT, Li Guo, and Z. X. Li. "Finite element modelling for fatigue stress analysis of large suspension bridges." Journal of Sound and Vibration 261.3 (2003): 443-464.

[71] Rajappan, R., and V. Pugazhenthi. "Finite element analysis of aircraft wing using composite structure." The International Journal of Engineering and Science (IJES) 2.2 (2013): 74-80.

[72] Tang, Jiapeng, et al. "A finite element parametric modeling technique of aircraft wing structures." Chinese Journal of Aeronautics 26.5 (2013): 1202-1210.

[73] Aabid, Abdul, et al. "Structural analysis of three-dimensional wings using finite element method." Aerospace Systems 5.1 (2022): 47-63.

[74] Sarojini, Darshan. Structural analysis and optimization of aircraft wings through dimensional reduction. Diss. Ph. D. thesis, Georgia Institute of Technology, 2021.

[75] Descombes, Stéphane, et al. "Recent advances on a DGTD method for time-domain electromagnetics." Photonics and Nanostructures-Fundamentals and Applications 11.4 (2013): 291-302.

[76] Niegemann, J., W. Pernice, and Kurt Busch. "Simulation of optical resonators using DGTD and FDTD." Journal of Optics A: Pure and Applied Optics 11.11 (2009): 114015.

[77] Piperno, Serge. "Symplectic local time-stepping in non-dissipative DGTD methods applied to wave propagation problems." ESAIM: Modélisation mathématique et analyse numérique 40.5 (2006): 815-841.

[78] Yan, Su, and Jian-Ming Jin. "A dynamic $ p $-adaptive DGTD algorithm for electromagnetic and multiphysics simulations." IEEE Transactions on Antennas and Propagation 65.5 (2017): 2446-2459.

[79] Li, Linqian, et al. "High-order SO-DGTD simulation of radio wave propagation through inhomogeneous weakly ionized dusty plasma

sheath." IEEE Antennas and Wireless Propagation Letters 16 (2017): 2078-2081.

[80] Wei, Bing, et al. "Analysis of the transmission characteristics of radio waves in inhomogeneous weakly ionized dusty plasma sheath based on high order SO-DGTD." Results in physics 7 (2017): 2582-2587.

[81] Li, Ping, Li Jun Jiang, and Hakan Bağcı. "A resistive boundary condition enhanced DGTD scheme for the transient analysis of graphene." IEEE Transactions on Antennas and Propagation 63.7 (2015): 3065-3076.

[82] Li, Ping, and Li Jun Jiang. "Modeling of magnetized graphene from microwave to THz range by DGTD with a scalar RBC and an ADE." IEEE Transactions on Antennas and Propagation 63.10 (2015): 4458-4467.

[83] Singer, H. "The method of moments (MOM) and related codes." 13th International Zurich Symposium and Technical Exhibition on Electromagnetic Compatibility. IEEE, 1999.

[84] Ji, Yun, Hao Wang, and Todd H. Hubing. "A novel preconditioning technique and comparison of three formulations for hybrid FEM/MOM methods." Applied Computational Electromagnetics Society Journal 15.2 (2000): 103-114.

[85] Perini, Jose, and Douglas J. Buchanan. "Assessment of MOM techniques for shipboard applications." IEEE Transactions on Electromagnetic Compatibility 1 (1982): 32-39.

[86] N. Kokkinos, N. Christofides, and C. Charalambous, "Lightning protection practice for large-extended photovoltaic installations," in 2012 International Conference on Lightning Protection (ICLP), 2012, pp. 1-5: IEEE.

[87] C. A. Charalambous, N. Kokkinos, N. Christofides, M. Z. A. Ab Kadir, and C. Gomes, "A simulation tool to assess the lightning induced over-voltages on dc cables of photovoltaic installations," in 2014 International Conference on Lightning Protection (ICLP), 2014, pp. 1571-1576: IEEE.

[88] C. A. Charalambous, N. D. Kokkinos, and N. Christofides, "External lightning protection and grounding in large-scale photovoltaic applications," IEEE transactions on electromagnetic compatibility, vol. 56, no. 2, pp. 427-434, 2013.

[89] A. Ayub, W. Siew, and F. Peer, "Grounding strategies for solar PV panels," in 2018 IEEE International Symposium on Electromagnetic Compatibility and 2018 IEEE Asia-Pacific Symposium on Electromagnetic Compatibility (EMC/APEMC), 2018, pp. 418-422: IEEE.

[90] F. P. Mohamed, W. H. Siew, and S. Mahmud, "Effect of group grounding on the potential rise across solar PV panels during lightning strike," in 2019 11th Asia-Pacific International Conference on Lightning (APL), 2019, pp. 1-5: IEEE.

[91] R. Araneo, M. Maccioni, S. Lauria, and S. Celozzi, "Analysis of the lightning transient response of the earthing system of large-scale ground-mounted PV plants," in 2017 IEEE Manchester PowerTech, 2017, pp. 1-6: IEEE.

[92] J. Birkl and E. Shulzhenko, "Investigation of Lightning Current Distribution in a Large Scale Earth-Termination System of Photovoltaic Power Plant," in 2018 34th International Conference on Lightning Protection (ICLP), 2018, pp. 1-7: IEEE.

[93] P. H. Pretorius, "Loss of equipotential during lightning ground potential rise on large earthing systems," in 2018 IEEE International Symposium on Electromagnetic Compatibility and 2018 IEEE Asia-Pacific Symposium on Electromagnetic Compatibility (EMC/APEMC), 2018, pp. 793-797: IEEE.

[94] I. Naxakis, G. Mihos, S. Pastromas, and E. Pyrgioti, "Examining the operation of the grounding system of a PV installation," in 2018 IEEE International Conference on High Voltage Engineering and Application (ICHVE), 2018, pp. 1-4: IEEE.

[95] P. H. Pretorius, "Dielectric Breakdown Between PV Panel Frames and StructuresБ─⌠A Hypothesis," in 2018 IEEE 4th Global Electromagnetic Compatibility Conference (GEMCCON), 2018, pp. 1-5: IEEE.

[96] K. Sakai and K. Yamamoto, "Lightning protection of photovoltaic power generation system: Influence of grounding systems on overvoltages appearing on DC wirings," in 2013 International Symposium on Lightning Protection (XII SIPDA), 2013, pp. 335-339: IEEE.

[97] IEC 62305-3: Protection against lightning – Part 3: Physical damage to structures and life hazard, 2010.

[98] S. N. Fallah, C. Gomes, M. Izadi, M. Ab Kadir, R. J. Ahmed, and J. bt Jasni, "Minimum separation between lightning protection system and non-integrated metallic structures," in 2018 34th International Conference on Lightning Protection (ICLP), 2018, pp. 1-8: IEEE.

[99] K. Yonezawa, S. Mochizuki, Y. Takahashi, T. Idogawa, and N. Morii, "Evaluation of SPDs for a PV system using the FDTD method taking concrete foundations into consideration," in 2014 International Conference on Lightning Protection (ICLP), 2014, pp. 1091-1094: IEEE.

[100] Y. Tu, C. Zhang, J. Hu, S. Wang, W. Sun, and H. Li, "Research

on lightning overvoltages of solar arrays in a rooftop photovoltaic power system," Electric power systems research, vol. 94, pp. 10-15, 2013.

[101] Y. Zhang, H. Chen, and Y. Du, "Lightning protection design of solar photovoltaic systems: Methodology and guidelines," Electric Power Systems Research, vol. 174, p. 105877, 2019.

[102] Z. Mohammed, H. Hizam, and C. Gomes, "Analysis of lightning transient effects on hybrid renewable energy sources," in 2018 34th International Conference on Lightning Protection (ICLP), 2018, pp. 1-7: IEEE.

[103] N. H. Zaini et al., "Lightning surge analysis on a large scale grid-connected solar photovoltaic system," Energies, vol. 10, no. 12, p. 2149, 2017.

[104] N. Zaini et al., "On the effect of lightning on a solar photovoltaic system," in 2016 33rd International Conference on Lightning Protection (ICLP), 2016, pp. 1-4: IEEE.

[105] N. Zaini et al., "Lightning Surge on the DC and AC Side of Solar PV System," in 2019 11th Asia-Pacific International Conference on Lightning (APL), 2019, pp. 1-5: IEEE.

[106] H. Haeberlin, "Damages at bypass diodes by induced voltages and

currents in PV modules caused by nearby lightning currents," in 22nd EU PV Conf., Milano, 2007.

[107] H. Haeberlin and M. Kaempfer, "Measurement of damages at bypass diodes by induced voltages and currents in PV modules caused by nearby lightning currents with standard waveform," in 23rd European Photovoltaic Solar Energy Conference, 2008.

[108] K. M. Coetzer, P. G. Wiid, and A. J. Rix, "PV Installation Design Influencing the Risk of Induced Currents from Nearby Lightning Strikes," in 2019 International Conference on Clean Electrical Power (ICCEP), 2019, pp. 204-213: IEEE.

[109] N. Ishikura, T. Okamoto, I. Nanno, T. Hamada, S. Oke, and M. Fujii, "Simulation analysis of really occurred accident caused by short circuit failure of blocking diode and bypass circuit in the photovoltaics system," in 2018 7th International Conference on Renewable Energy Research and Applications (ICRERA), 2018, pp. 533-536: IEEE.

[110] K. M. Coetzer, P. G. Wiid, and A. J. Rix, "The MOV as a Possible Protection Measure for Bypass Diodes in Solar PV Modules," in 2019 International Conference on Clean Electrical Power (ICCEP), 2019, pp. 286-291: IEEE.

[111] R. Pease, J. Barnum, W. Vulliet, V. Van Lint, and T. Wrobel, "Silicon solar cell damage from electrical overstress," IEEE

Transactions on Nuclear Science, vol. 29, no. 6, pp. 1525 1532, 1982.

[112] M. Belik, "PV panels under lightning conditions," in Proceedings of the 2014 15th International Scientific Conference on Electric Power Engineering (EPE), 2014, pp. 367 370: IEEE.

[113] I. Naxakis, E. Pyrgioti, V. Perraki, and E. Tselepis, "Studying the effect of the impulse voltage application on sc-Si PV modules," Solar Energy, vol. 144, pp. 721-728, 2017.

[114] I. Naxakis, C. Christodoulou, V. Perraki, and E. Pyrgioti, "Degradation effects on single crystalline silicon photovoltaic modules subjected to high impulse-voltages," IET Science, Measurement & Technology, vol. 11, no. 5, pp. 563-570, 2017.

[115] N. Ahmad et al., "On the performance of a polycrystalline PV panel under different impulse voltages and temperatures," in 2016 33rd International Conference on Lightning Protection (ICLP), 2016, pp. 1-6: IEEE.

[116] H. l. E. Sueta, A. Mocelin, R. Zilles, P. F. Obase, and E. Boemeisel, "Protection of Photovoltaic Systems Against Lightning Experimental verifications and techno-economic analysis of protection," in 2013 International Symposium on Lightning Protection (XII SIPDA), 2013, pp. 354-359: IEEE.

[117] T. Jiang and S. Grzybowski, "Influence of lightning impulse voltages on power output characteristics of Photovoltaic modules," in 2014 ICHVE International Conference on High Voltage Engineering and Application, 2014, pp. 1-4: IEEE.

[118] T. Jiang and S. Grzybowski, "Impact of lightning impulse voltage on polycrystalline silicon photovoltaic modules," in 2013 International Symposium on Lightning Protection (XII SIPDA), 2013, pp. 287-290: IEEE.

[119] T. Jiang and S. Grzybowski, "Electrical degradation of Photovoltaic modules caused by lightning induced voltage," in 2014 IEEE Electrical Insulation Conference (EIC), 2014, pp. 107-110: IEEE.

[120] G. L. Amicucci, F. Fiamingo, and T. Kisielewicz, "Risk assessment of photovoltaic installations, due to lightning, according to IEC 62305," in 2012 International Conference on Lightning Protection (ICLP), 2012, pp. 1-6: IEEE.

[121] S. Ittarat, S. Hiranvarodom, and B. Plangklang, "A computer program for evaluating the risk of lightning impact and for designing the installation of lightning rod protection for photovoltaic system," Energy Procedia, vol. 34, pp. 318-325, 2013.

[122] I. Holland, W. Doorsamy, and K. Nixon, "Computational methodology for lightning risk assessment of small-scale rooftop

photovoltaic systems," in 2018 IEEE International Conference on Environment and Electrical Engineering and 2018 IEEE Industrial and Commercial Power Systems Europe (EEEIC/I&CPS Europe), 2018, pp. 1-6: IEEE.

[123] IEC 62305-2: Protection against lightning - Part 2: Risk management, 2010.

[124] IEC 61400-24: Wind turbines Part 24： Lightning protection, 2012.

[125] A. Dimitriou, C. A. Charalambous, and N. Kokkinos, "Integrating the loss of economic value in lightning-related risk assessments of large scale photovoltaic systems participating in regulated and competitive energy markets," in 2016 33rd International Conference on Lightning Protection (ICLP), 2016, pp. 1-6: IEEE.

[126] A. Kern and F. Krichel, "Considerations about the lightning protection system of mains independent renewable energy hybrid-systems ─ practical experiences," Journal of Electrostatics, vol. 60, no. 2-4, pp. 257-263, 2004.

[127] R. Pomponi and R. Tommasini, "Risk assessment and lightning protection for PV systems and solar power plants," in Int. Conf. on Renewable Energies and Power Quality (ICREPQ Б─≤12), 2012.

[128] I. Holland, W. Doorsamy, and K. Nixon, "Lightning Risk Assessment of Rooftop Photovoltaic Systems: A Case Study Approach," in 2018 IEEE PES/IAS PowerAfrica, 2018, pp. 1-6: IEEE.

[129] Y. Du and M. Chen, "Influence of building structures on the lightning return stroke current," IEEE transactions on power delivery, vol. 25, no. 1, pp. 307-315, 2009.

[130] A. Formisano, C. Petrarca, J. C. Hernц╟ndez, and F. J. Muц╟oz-Rodrцёguez, "Assessment of induced voltages in common and differential-mode for a PV module due to nearby lightning strikes," IET Renewable Power Generation, vol. 13, no. 8, pp. 1369 1378, 2019.

[131] I. Naxakis, P. Nikolaidis, and E. Pyrgioti, "Performance of an installed lightning protection system in a photovoltaic park," in 2016 IEEE International Conference on High Voltage Engineering and Application (ICHVE), 2016, pp. 1-4: IEEE.

[132] D. Moongilan, "Residential solar system bonding and grounding methods for lightning protection," in 2013 IEEE Symposium on Product Compliance Engineering (ISPCE), 2013, pp. 1-6: IEEE.

[133] C. Zhang, Y. Tu, J. Hu, W. Sun, H. J. Li, and S. Wang, "Study of induced overvoltage on solar arrays," in 2011 7th Asia-Pacific International Conference on Lightning, 2011, pp. 852-857: IEEE.

[134] C. Christodoulou, K. Damianaki, V. Kontargyri, I. Gonos, A. Kyritsis, and N. Papanikolaou, "Protection of 100kWp photovoltaic system against atmospheric overvoltages: a case study," in 2016 IEEE International Conference on High Voltage Engineering and Application (ICHVE), 2016, pp. 1-4: IEEE.

[135] K. Yamamoto, J. Takami, and N. Okabe, "Overvoltages on DC side of power conditioning system caused by lightning stroke to structure anchoring photovoltaic panels," Electrical Engineering in Japan, vol. 187, no. 4, pp. 29-41, 2014.

[136] Y. Du and Y. Ding, “Lightning surge propagation on a single conductor in free space,” IEEE Trans. Electromagn. Compat., vol. 59, no. 1, pp. 119-127, Feb. 2017.

[137] Y. Ding, Y. P. Du and M. Chen, “Lightning surge propagation on a grounded vertical conductor,” IEEE Trans. Electromagn. Compat., vol. 60, no. 1, pp. 276 279, Feb. 2018.

[138] S. Visacro and A. Soares, “HEM: a model for simulation of lightning-related engineering problems,” IEEE Trans. Power Del., vol. 20, no. 2, pp. 1206-1208, Apr. 2005.

[139] F. H. Silveira, S. Visacro, J. Herrera and H. Torres, “Evaluation of lightning induced voltages over a lossy ground by the hybrid electromagnetic model,” IEEE Trans. Electromagn. Compat., vol. 51,

no. 1, pp. 156-160, Feb. 2009.

[140] R. M. Kielkowski, Inside Spice. New York: McGraw-Hill, 1998.

[141] Baratta, Igor A., et al. "Infinitesimal dipole model using space mapping optimization for antenna placement." IEEE Antennas and Wireless Propagation Letters 17.1 (2017): 17-20.

[142] Rakov, Vladimir A., and Martin A. Uman. "Review and evaluation of lightning return stroke models including some aspects of their application." IEEE transactions on electromagnetic compatibility 40.4 (1998): 403-426.

[143] Qi, Ruihan, Ya Ping Du, and Mingli Chen. "Time-domain PEEC transient analysis for a wire structure above the perfectly conducting ground with the incident field from a distant lightning channel." IEEE Transactions on Electromagnetic Compatibility 62.5 (2019): 1787-1795.

[144] H. Chen, Y. Du, and M. Chen, “Lightning transient analysis of radio base stations,” IEEE Trans Power Del., vol. 33, no. 5, pp. 2187–2197, Oct. 2018.

[145] Qi, Ruihan, Ya Ping Du, and Mingli Chen. "Time-domain PEEC transient analysis for a wire structure above the perfectly conducting ground with the incident field from a distant lightning channel." IEEE

Transactions on Electromagnetic Compatibility 62.5 (2019): 1787-1795.

[146] Nucci, Carlo Alberto, et al. "Lightning-induced voltages on overhead lines." IEEE Transactions on Electromagnetic Compatibility 35.1 (1993): 75-86.

[147] Delfino, Federico, et al. "An algorithm for the exact evaluation of the underground lightning electromagnetic fields." IEEE Transactions on Electromagnetic Compatibility 49.2 (2007): 401-411.

[148] Dommel, Hermann W. EMTP theory book. Microtran Power System Analysis Corporation, 1996.

[149] Subedi, Deepak. "Lightning induced over-voltages in power transformer and voltage spikes in connected load." (2017).

[150] Zola, Julio Guillermo. "Simple model of metal oxide varistor for Pspice Simulation." IEEE Transactions on computer-aided design of integrated circuits and Systems 23.10 (2004): 1491-1494.

[151] Zhang, Yang, et al. "Lightning transient analysis of main and submain circuits in commercial buildings using PEEC method." *IEEE Transactions on Industry Applications* 56.1 (2019): 106-116.

[152] Chen, Hongcai, and Ya-ping Du. "A comprehensive study on the nonlinear behavior of metal oxide varistors." 2016 33rd International

Conference on Lightning Protection (ICLP). IEEE, 2016.

[153] Rachidi, F., & Tkachenko, S. Electromagnetic field interaction with transmission lines: from classical theory to HF radiation effects (Vol. 5). WIT press, 2008.

[154] R. Qi, Y. Ding, Y. P. Du, M. Chen and Z. Li, "Evaluation of Green's Functions for PEEC Models in the Air and Lossy-Ground Space," in IEEE Transactions on Electromagnetic Compatibility, vol. 63, no. 6, pp. 1930-1940, Dec. 2021, doi: 10.1109/TEMC.2021.3098027.

[155] R. Qi, Y. Ding, Y. P. Du, M. Chen and Z. Li, "Evaluation of Green's Functions for PEEC Models in the Air and Lossy-Ground Space," in IEEE Transactions on Electromagnetic Compatibility, vol. 63, no. 6, pp. 1930-1940, Dec. 2021, doi: 10.1109/TEMC.2021.3098027.

[156] Y. P. Yutthagowith, A. Ametani, F. Rachidi, N. Nagaoka, and Y. Baba, “Application of a partial element equivalent circuit method to lightning surge analyses,” Elect. Power Syst. Res., vol. 94, pp. 30–37, Jan. 2013.

[157] C. D. Taylor, R. S. Sattenvhite, and C. W. Harrison, “The response of a terminated two-wire transmission line excited by a nonuniform electromagnetic field,” IEEE Trans. Antennas Propag., vol.

13, no. 6, pp. 987–989, Nov. 1965.

[158] Hallemans, Leonie, et al. "A stepwise methodology for the design and evaluation of protection strategies in LVDC microgrids." Applied Energy 310 (2022): 118420.